

# **Modeling and Control of Diesel-Hydrokinetic Microgrids**

Mohammadhossein Ashourianjozdani

A Thesis  
in  
The Department  
of  
Electrical and Computer Engineering

Presented in Partial Fulfilment of the Requirements  
For the Degree of  
Doctor of Philosophy (Electrical and Computer Engineering) at  
Concordia University  
Montréal, Québec, Canada

April 2018

© Mohammadhossein Ashourianjozdani, 2018

**CONCORDIA UNIVERSITY**  
**SCHOOL OF GRADUATE STUDIES**

This is to certify that the thesis prepared

By: Mohammadhossein Ashourianjozdani

Entitled: Modeling and Control of Diesel-Hydrokinetic Microgrids

and submitted in partial fulfillment of the requirements for the degree of

Doctor of Philosophy (Electrical & Computer Engineering)

complies with the regulation of the University and meets the accepted standards with respect to originality and quality.

Signed by the final Examining Committee:

_____	Chair
Dr. Ketra Schmitt	
_____	External Examiner
Dr. Sousso Kelouwani	
_____	Examiner
Dr. Youmin Zhang	
_____	Examiner
Dr. Shahin Hashtrudi Zad	
_____	Examiner
Dr. Akshay Kumar Rathore	
_____	Thesis Co-Supervisor
Dr. Pragasen Pillay	
_____	Thesis Co-Supervisor
Dr. Luiz A. C. Lopes	

Approved by \_\_\_\_\_  
Dr. Wei-Ping Zhu, Graduate Program Director

Thursday, June 7, 2018

\_\_\_\_\_  
Dr. Amir Asif, Dean  
Faculty of Engineering and Computer Science

## **ABSTRACT**

### **Modeling and Control of Diesel-Hydrokinetic Microgrids**

**Mohammadhossein Ashourianjozdani, Ph.D.**

**Concordia University, 2018**

A large number of decentralized communities in Canada and particularly in Québec rely on diesel power generation. The cost of electricity and environmental concerns suggest that hydrokinetic energy is a potential for power generation. Hydrokinetic energy conversion systems (HKECSs) are clean, reliable alternatives, and more beneficial than other renewable energy sources and conventional hydropower generation. However, due to the stochastic nature of river speed and variable load patterns of decentralized communities, the use of a hybrid diesel-hydrokinetic (D-HK) microgrid system has advantages. A large or medium penetration level has a negative effect on the short-term (transient) and long-term (steady-state) performance of such a hybrid system if the HKECS is controlled based on conventional control schemes. The conventional control scheme of the HKECS is the maximum power point tracking (MPPT). In the long-term conditions, the diesel generator set (genset) can operate at a reduced load where the role of the HKECS is to reduce the electrical load on the diesel genset (light loading). In the short-term, the frequency of the microgrid can vary due to the variable nature of water speed and load patterns. This can lead to power quality problems like a high rate of change of frequency or power, frequency fluctuations, etc. Moreover, these problems are magnified in storage-less D-HK microgrids where a conventional energy storage system is not available to mitigate power as well as frequency deviations by controlling active power. Therefore, developing sophisticated control strategies for the HKECS to mitigate problems as mentioned above are necessary. Another challenging issue is a hardware-in-the-loop (HIL) platform for testing and developing a D-HK microgrid.

A dispatchable power controller for a fixed-pitch cross-flow turbine-based HKECS operating in the low rotational speed (stall) region is presented in this thesis. It delivers a given power requested by an operator provided that the water speed is high enough. If not, it delivers as much as possible, operating with an MPPT algorithm while meeting the basic operating limits (i.e., generator voltage and rotor speed, rated power, and maximum water speed), shutting down automatically if necessary. A supervisory control scheme provides a smooth transition between modes of operation as the water speed and reference power from the operator vary. The performance of the proposed dispatchable power controller and supervisory control algorithm is verified experimentally with an electromechanical-based hydrokinetic turbine (HKT) emulator.

The permanent magnet synchronous generator (PMSG) is preferred in small HKECSs. So, a converter-based PMSG emulator as a testbed for designing, analyzing, and testing of the generator's power electronic interface and its control system is developed. A 6-switch voltage source converter (VSC) is used as a power amplifier to mimic the behaviour of the PMSG supplying linear and non-linear loads. Technical challenges of the PMSG emulator are considered, and proper solutions are suggested.

Finally, an active power sharing control strategy for a storage-less D-HK microgrid with medium and high penetration of hydrokinetic power to mitigate: 1) the effect of the grid frequency fluctuation due to instantaneous variation in the water speed/load, and 2) light loading operation of the diesel engine is proposed. A supplementary control loop that includes virtual inertia and frequency droop control is added to the conventional control system of HKECS in order to provide load power sharing and frequency support control. The proposed strategy is experimentally verified with diesel engine and HKT emulators controlled via a dSPACE® rapid control prototyping system. The transient and steady-state performance of the system including grid frequency and power balancing control are presented.

*To my wife and son, Firoozeh & Daniel*

## ACKNOWLEDGEMENTS

I would like to express my deep and sincere gratitude to my supervisor, Prof. P. Pillay for giving me the opportunity to go through the PhD program. He has inspired me in many ways, from the beginning to the end of my research program. It has been an honor for me to be his PhD student. I also would like to thank him for the financial support.

I am deeply grateful to my co-supervisor, Prof. L. Lopes for his detailed guidance and constructive advices, from which I have learned and developed important technical skills to become a better researcher in the field of electrical engineering.

I would also like to thank my committee members, Prof. Youmin Zhang, Prof. Shahin Hashtrudi Zad and Prof. Akshay Kumar Rathore for serving as my committee members even at hardship. I also want to thank all of them on their brilliant comments and suggestions and their valuable time.

I would like to express my deepest gratitude to my parents, Abbas and Mahin, and my sisters, Somayeh and Samaneh, for their unconditional support throughout my entire life, to my beloved wife Firoozeh, for her emotional support and continuous encouragement, and to my son Daniel.

My sincere gratitude goes to all my colleagues from the PEER group at Concordia University for being supportive in my PhD journey.

I would like to thank and acknowledge the support of the Natural Sciences & Engineering Research Council of Canada and Hydro-Québec for this work. This work was supported in part by the R&D program of the NSERC Chair entitled “Design and Performance of Special Electrical Machines” established in Concordia University.

# TABLE OF CONTENTS

LIST OF FIGURES .....	x
LIST OF TABLES .....	xiv
LIST OF ABBREVIATIONS .....	xv
Chapter 1. Introduction .....	1
1.1 Background .....	1
1.2 The Potential of Diesel-Hydrokinetic Microgrid .....	5
1.2.1 Characteristics of the D-HK Microgrid .....	6
1.2.2 Power Control Considerations for HKECS .....	8
1.3 Technical Issues in Small-Scale Storage-Less D-HK Microgrid.....	9
1.4 Contributions.....	10
1.5 Thesis outline .....	12
1.6 Summary .....	13
Chapter 2. Theory, Modeling and Design Considerations of Diesel-Hydrokinetic Microgrid .....	14
2.1 Structure and Operation of HKECS .....	14
2.1.1 Hydrokinetic Turbine (HKT).....	15
2.1.2 Drivetrain System .....	17
2.1.3 Electrical Generator, PMSG .....	18
2.1.4 Control Strategies for Fixed-Pitch HKT .....	19
2.1.5 HKECS Power Electronic Interfaces.....	23
2.2 Diesel Generator Set .....	38
2.2.1 Diesel Engine and Coupling Shaft.....	39
2.2.2 Electrical Generator.....	39
2.2.3 Speed Governor .....	40
2.2.4 Automatic Voltage Regulator (AVR).....	41
2.3 Summary .....	43
Chapter 3. Supervisory Power Control for a Dispatchable Fixed-Pitch PMSG-Based Hydrokinetic Energy Conversion System.....	45
3.1 Introduction.....	45
3.2 Description of HKT Operating Conditions .....	47
3.2.1 MPPT Operation.....	49
3.3 Design of the Controllers for Power and Speed/Voltage Regulation in the Stall Region.....	50
3.3.1 The Inner Speed/Voltage Loop.....	52

3.3.2	The Outer Power Loop .....	55
3.4	Proposed Supervisory Power Control System .....	58
3.5	Electromechanical-based HKT Emulator .....	61
3.6	Experimental Results and Discussion .....	63
3.6.1	Power Control Strategy Procedure .....	63
3.6.2	Shutdown Procedure.....	64
3.6.3	Power vs Water Speed Characteristic.....	66
3.7	Summary .....	67
Chapter 4.	Power Electronic Converter-Based PMSG Emulator: A Testbed for Renewable Energy Experiments	68
4.1	Introduction.....	68
4.2	PMSG Emulator Configuration .....	71
4.3	PMSG Modeling in the Real-Time Simulator .....	73
4.4	VSC Modeling and Control .....	75
4.5	Virtual Impedance Selection and Performance Considerations.....	81
4.6	Experimental Observations and Discussions .....	86
4.6.1	Changing the Input Power with a Constant Load Impedance.....	87
4.6.2	Effect of the Virtual Impedance on the Emulator's Performance.....	93
4.7	Summary .....	94
Chapter 5.	Power and Frequency Support Control for a Storage-less Diesel Hydrokinetic Microgrid	96
5.1	Introduction.....	96
5.2	Power and Frequency Control for a Storage-Less D-HK Microgrid .....	99
5.3	HKECS Configuration and Operation .....	102
5.3.1	HKECS Control Scheme .....	102
5.3.2	DL Operation Mode.....	104
5.4	Proposed Frequency Support Control Scheme of the HKECS .....	106
5.4.1	Frequency Support Control Scheme of the HKECS Using the Boost DC-DC Converter..	107
5.4.2	Selection of the Frequency Loop Gains.....	109
5.5	Experimental Results and Discussions.....	113
5.5.1	D-HK Microgrid Emulator as Experimental Test-bed.....	113
5.5.2	Response to a Step Load Variation.....	116
5.5.3	Response to a Water Speed Variation.....	121
5.6	Summary .....	124
Chapter 6.	Conclusions and Future Works .....	125
6.1	Conclusions.....	125
6.2	Proposed Future Work .....	127

References .....	129
Appendix A .....	145
Appendix B .....	148
Appendix C .....	153

## LIST OF FIGURES

Figure 1.1 Remote communities in Quebec [3] .....	2
Figure 1.2 Two most common small-scale HKTs .....	4
Figure 1.3 D-HK microgrid .....	6
Figure 1.4 Water speed measured along the Winnipeg river, Manitoba at a constant depth, approximately 1.5 m [19] .....	7
Figure 2.1 Block diagram of the HKECS structure .....	14
Figure 2.2 (a) $C_p$ and $C_q$ versus $\lambda$ curves; (b) HKT power versus turbine shaft speed ( $\omega m$ ) at different water speeds ( $vT$ ) .....	16
Figure 2.3 Equivalent circuit of the PMSG in d-axis and q-axis frames. ....	18
Figure 2.4 the power coefficient ( $C_p$ ) versus rotor speed ( $\omega m$ ) for a constant water speed ( $vT$ ). ..	19
Figure 2.5 HKECS power flow during deceleration when HKT works in section II .....	22
Figure 2.6 Different generator-side converter topologies .....	23
Figure 2.7 PMSG controller in dq-frame [37] .....	24
Figure 2.8 Schematic of CC-VSI and its electronic interface .....	25
Figure 2.9 control block diagram of internal current controlled VSI in dq-frame .....	26
Figure 2.10 Bode plot for closed-loop and open-loop current controller. VSI parameters: $R_F =$ $0.1 \Omega$ , $L_F = 2 \text{ mH}$ $\tau_i = 0.0008 \text{ s}$ , $MPWM=1$ , $T_s = 80 \text{ ns}$ , $T_D = 20 \text{ ns}$ . ....	28
Figure 2.11 Space vector diagram CC-VSI control scheme .....	29
Figure 2.12 Block diagram of three phase SRF-PLL .....	30
Figure 2.13 Simulation results of SRF-PLL performance under both a phase jump of $90^\circ$ and a step change of frequency from 60 Hz to 59 Hz. (a) the grid voltage in abc-frame, (b) the phase angle of the grid voltage, (c) input ideal and locked grid voltage, and (d) the grid and estimated frequency. ....	31
Figure 2.14 $V_{dc}$ vs. PMSG rotor speed $\omega g$ across various water speeds .....	34
Figure 2.15 a) Simplified circuit of the boost converter, b) nonlinear averaged model of the boost converter. ....	35
Figure 2.16 Simulation results of the power electronics interface performance of the HKECS performance for an increase step change from 0.5 to 0.6 in duty cycle of the boost converter. a) output voltage of diode rectifier and DC-link voltage b) output active and reactive power of the HKECS, c) output current and voltage of the HKECS .....	36
Figure 2.17 VSI vector diagram for unit power factor (UPF) and leading power factor (LPF) operation .....	38

Figure 2.18 Diesel genset model.....	38
Figure 2.19 The model of (a) speed governor, (b) AVR.....	41
Figure 2.20 Isochronous mode operation of diesel genset; (a) frequency, (b) output active power, (c) output phase voltage, and (d) output current. ....	43
Figure 2.21 Droop mode operation of diesel genset; (a) frequency, (b) output active power, (c) output phase voltage, and (d) output current. ....	43
Figure 3.1 HKT output power ( $PHKT$ ) vs. water speed curve ( $vT$ ).....	48
Figure 3.2 Schematic diagram of the HKECS. ....	49
Figure 3.3. The real part of plant poles vs. tip speed ratio at water speed 1.2 m/s and 3 m/s.....	54
Figure 3.4 Root locus of the system with the designed voltage controller at $vT = 3$ m/s and $\lambda = 0.8$ . ....	55
Figure 3.5 Step response of the voltage loop for $vT = 1.2$ m/s and 3 m/s at $\lambda = 0.15, 0.8, 2.1, 3$ . ...	55
Figure 3.6 A cascaded inner voltage and outer power loop control block diagram of the system for operation in the stall region. ....	57
Figure 3.7 $P_{dc}$ open-loop response to a variation in $V_{dc}$ * from 80 V to 85 V with $vT = 3$ m/s....	57
Figure 3.8 Step responses of the power loop for $v_T = 1.2$ m/s and 3 m/s at $\lambda = 0.8$ . ....	58
Figure 3.9 Power vs. output voltage of the diode rectifier for various water speeds and operating conditions of the HKECS. ....	60
Figure 3.10 Overall control diagram of the proposed supervisory power control system. ....	60
Figure 3.11 (a) Electromechanical-based emulator block diagram, (b) Experimental setup of the HKECS system. ....	62
Figure 3.12 HKECS system parameters: (a) water speed variations, (b) output DC power, (c) output DC voltage, (d) PMSG rotor speed, and (e) turbine power coefficient. ....	65
Figure 3.13 HKECS system measurements during shut-down procedure at water speed 3 m/s: (a) water speed variations, (b) output DC power, (c) output DC voltage, (d) PMSG rotor speed. ....	66
Figure 3.14 DC-link power characteristic with respect to the water speed. ....	67
Figure 4.1 Basic block diagram of the emulator of the PMSG-based energy conversion system.....	69
Figure 4.2 (a) The original system. (b) PHIL simulation for the PMSG emulator.....	73
Figure 4.3 Block diagram of the PMSG in real-time simulation platform, where 't' is the sampling time. ....	75
Figure 4.4 (a) Schematic diagram of the VC-VSC for the converter-based power amplifier, (b) Control block diagram of the VC-VSC. ....	77

Figure 4.5 Bode plot of $G_{vs}$ , $G_A$ s & $H_Z(s)$ when $\omega_0 = 2\pi 60 \times 6 \text{ rad/s}$ .....	81
Figure 4.6 Block diagrams: (a) original system, (b) PMSG emulator with the modified voltage type ITM.....	82
Figure 4.7 Bode diagram of (4.21) with changing loads up to 400% overload for the purely resistive and resistive-inductive load impedances .....	85
Figure 4.8 Comparison of the frequency responses of the virtual impedance calculated by (4.21) and proposed series RLC impedance/filter.....	85
Figure 4.9 Experimental setup.....	87
Figure 4.10 Variation of the PMSG emulator input power.....	88
Figure 4.11 Test results of the PMSG emulator connected to a linear load; (a) phase voltage, (b) phase current, (c) frequency, (d) zoomed-in voltage around $t = 2\text{s}$ , (e) zoomed-in current around $t = 2\text{s}$ .....	89
Figure 4.12 Harmonic spectra of the PMSG emulator connected to a linear load; (a) voltage, (b) current.....	90
Figure 4.13 Results of the PMSG emulator connected to a non-linear load; (a) phase voltage, (b) phase current, (c) frequency, (d) zoomed-in voltage around $t = 2\text{s}$ , (e) zoomed-in current around $t = 2\text{s}$ .....	91
Figure 4.14 Harmonic spectra of the PMSG emulator connected to a nonlinear load; (a) voltage, (b) current.....	92
Figure 4.15 Results of the PMSG emulator connected to a non-linear load; (a) voltage in dq-frame, (b) phase current in dq-frame for 2 cycles waveform.....	93
Figure 4.16 Test results of the PMSG emulator using two different virtual impedances. (a) Phase voltage, (b) phase current.....	94
Figure 5.1 Schematic diagram of a generic storage-less D-HK microgrid.....	100
Figure 5.2 Block diagram of the HKECS.....	103
Figure 5.3 Power vs. output voltage of the diode rectifier for various water speeds and MPPT and DL Curves.....	106
Figure 5.4 DC-DC boost converter with frequency support control.....	108
Figure 5.5 Variations of the HKECS and genset output power with grid frequency for three different water speeds , $vT = [1.6 \text{ m/s}, 2.4 \text{ m/s}, 2.8 \text{ m/s}]$ , while $K_i=0$ ( $\Delta v_{dc}$ , $i = 0$ ), $K_d=24$ and $DL_{max}= 25\%$ .....	111
Figure 5.6 System response to a 30% step load change while $K_{d0} = 25$ and $DL_{max} = 25\%$ ; (a) grid frequency (i), output voltage of diode rectifier (ii), output power of HKECS(iii) for $vT = 2.8\text{m/s}$ , (b) grid frequency (i), output voltage of diode rectifier (ii), output power of HKECS (iii) for $vT = 2.4\text{m/s}$ .....	113

Figure 5.7 The block diagram of the storage-less D-HK microgrid emulator .....	115
Figure 5.8 Hardware of experimental setup for a D-HK microgrid emulator; 1. dSPACE and ABB drive control desk, 2. DC motor and PMSG, 3. industrial ABB drive, wound rotor synchronous generator and DC motor, 4. AC and DC loads, 5. Synchronization device, 6. dSPACE interface hardware, 7. diode rectifier, DC-DC boost converter, and inverter, 8. current and voltage sensors, 9. DC-DC buck converter, 10. coupling filters and transformers. ....	116
Figure 5.9 The system response for case I. The HKECS operates in MPPT mode. (a) grid frequency $f$ , (b) HKECS output active power $PHKECS$ and genset output active power $Pgenset$ , and (c) inverter DC-link voltage $V_o$ , diode rectifier output voltage $V_{dc}$ , turbine power coefficient $CP$ , and generator rotor speed $\omega g$ . ....	117
Figure 5.10 The system response for case II. The HKECS operates with proposed frequency support control while $K_i = 0$ during the test. (a) grid frequency $f$ , (b) HKECS output active power $PHKECS$ and diesel genset output active power $Pgenset$ , and (c) inverter DC-link voltage $V_o$ , diode rectifier output voltage $V_{dc}$ , turbine power coefficient $CP$ , and generator rotor speed $\omega g$ . ....	119
Figure 5.11 The system response for case III. The HKECS operates with proposed frequency support control loops. (a) grid frequency $f$ , (b) HKECS output active power $PHKECS$ and diesel genset output active power $Pgenset$ , and (c) inverter DC-link voltage $V_o$ , diode rectifier output voltage $V_{dc}$ , turbine power coefficient $CP$ , and generator rotor speed $\omega g$ . ....	120
Figure 5.12 Water speed variations.....	122
Figure 5.13 The system response to water speed variations while the HKECS operates with the MPPT mode. (a) grid frequency $f$ , (b) HKECS output active power $PHKECS$ and diesel genset output active power $Pgenset$ , and (c) inverter DC-link voltage $V_o$ , diode rectifier output voltage $V_{dc}$ , turbine power coefficient $CP$ , and generator rotor speed $\omega g$ . ....	122
Figure 5.14 The system response to water speed variations while the HKECS operates with the proposed frequency support control loops. (a) grid frequency $f$ , (b) HKECS output active power $PHKECS$ and diesel genset output active power $Pgenset$ , and (c) inverter DC-link voltage $V_o$ , diode rectifier output voltage $V_{dc}$ , turbine power coefficient $CP$ , and generator rotor speed $\omega g$ . ....	123

## LIST OF TABLES

Table 1.1 Relative power density of river current compared with the wind and solar sources .....	3
Table 1.2 Turbine configurations for hydrokinetic application; advantages and disadvantages [8], [10], [11].....	4
Table 2.1 A summary of some MPPT algorithms used in the HKECS .....	21
Table 5.1 Variation of the HKECS output power and output voltage of the diode rectifier with grid frequency for three different water speeds, $vT = [1.6 \text{ m/s}, 2.4 \text{ m/s}, 2.8 \text{ m/s}]$ , while $Ki = 0$ ( $\Delta vdc, i = 0$ ), $Kd = 24$ , and $DLmax = 25\%$ . .....	110
Table 5.2 Summary of the system response for Case I, Case II, and Case III results for a 30% step-up load change. $fs$ is the steady-state value of the grid frequency. ....	120
Table 5.3 Summary of the system response to water speed variations while the HKECS operates with the MPPT mode, and with the proposed frequency support control loops.....	123

## LIST OF ABBREVIATIONS

2L-VSI	→	Two-level Voltage Source Inverter
ADC	→	Analog-to-digital Converter
APC	→	Active Power Curtailment
APF	→	Active Power Flow
AVR	→	Automatic Voltage Regulator
CC-VSI	→	Current Controlled Voltage Source Inverter
CDCL	→	Controllable DC load
CPM	→	Cosntant Power Mode
DAC	→	Digital-to-analog Converter
DC	→	Direct Current
DER	→	Distributed Electrical Resource
D-HK	→	Diesel-Hydrokinetic
DIM	→	Damped ImpedanceMethod
DL	→	Deloading
D-W	→	Diesel-Wind
ESS	→	Energy Storage System
FEA	→	Finite-element Analysis
genset	→	Diesel Engine Driving an Electrical Generator
GR	→	Gear Ratio
HCC	→	Hysteresis Current Control
HIL	→	Hardware-In-The-Loop
HKECS	→	Hydrokinetic Energy Conversion System
HKT	→	Hydrokinetic Turbine
ITM	→	Ideal Transformer Method
LPF	→	Low Pass Filter
LV	→	Low Voltage

MPPT	→	Maximum Power Point Tracking
ODE	→	Ordinary Differential Equations
PCC	→	Point of Common Coupling
PCD	→	Partial Circuit Duplication
PEI	→	Power Electronic Interface
PHIL	→	Power Hardware-In-The-Loop
PI	→	Proportional Integral
PI+res	→	Proportional Integral Plus Resonant
PLL	→	Phase-locked Loop
PMSG	→	Permanent Magnet Synchronous Generator
PRM	→	Power Regulation Mode
RCP	→	Rapid Control Prototyping
ROCOF	→	Rate of Change of Frequency
RTI	→	Real-time Platform
WRSG	→	Wound Rotor Synchronous Generator
SG	→	Synchronous Generator
SLM	→	Speed Limiting Mode
SVPWM	→	Space Vector Pulse Width Modulation
TFA	→	Transient First-order Approximation
TFP	→	transfer function perturbation
TLA	→	Transmission Line Approximation
VC-VSI	→	Voltage Controlled Voltage Source Inverter
V-F	→	Voltage-Frequency
VSC	→	Voltage Source Converter

# Chapter 1. Introduction

*This chapter presents the background information on diesel-hydrokinetic microgrid systems. Advantages and disadvantages of such systems have been discussed, leading to the definition of the research goal and research objectives. The chapter finishes with presenting the new contributions and the structure of the Ph.D. thesis.*

## 1.1 Background

Historically, before the development of electrical grids, electricity was produced near the locations where it was required [1]. Presently, there are still many remote communities in the world which do not have access to a main power grid due to geographic barriers or economic issues. Many of these small decentralized communities rely on electricity from an electrical generator driven by a diesel engine. This autonomous power generation system is reliable, well established, relatively efficient and highly dependable [2]. In Quebec, there are communities with a permanent settlement that do not have access to the main power grid, and rely on local diesel generation for the production electricity. Figure 1.1 shows the distribution of these communities throughout five regions [3]. Of these communities, 20 rely on the local diesel generator set (diesel genset) for electrical power.

The cost of diesel fuel, fuel transportation and maintenance and operation are the main weaknesses of gensets. At this time, some remote communities in the north of Quebec pay around 0.80 \$/kWh for electricity whereas the price in Montreal is around 0.06 \$/kWh [4]. Furthermore, this source of power has significant adverse impacts on the environment due to CO<sub>2</sub> emissions [4], [5].

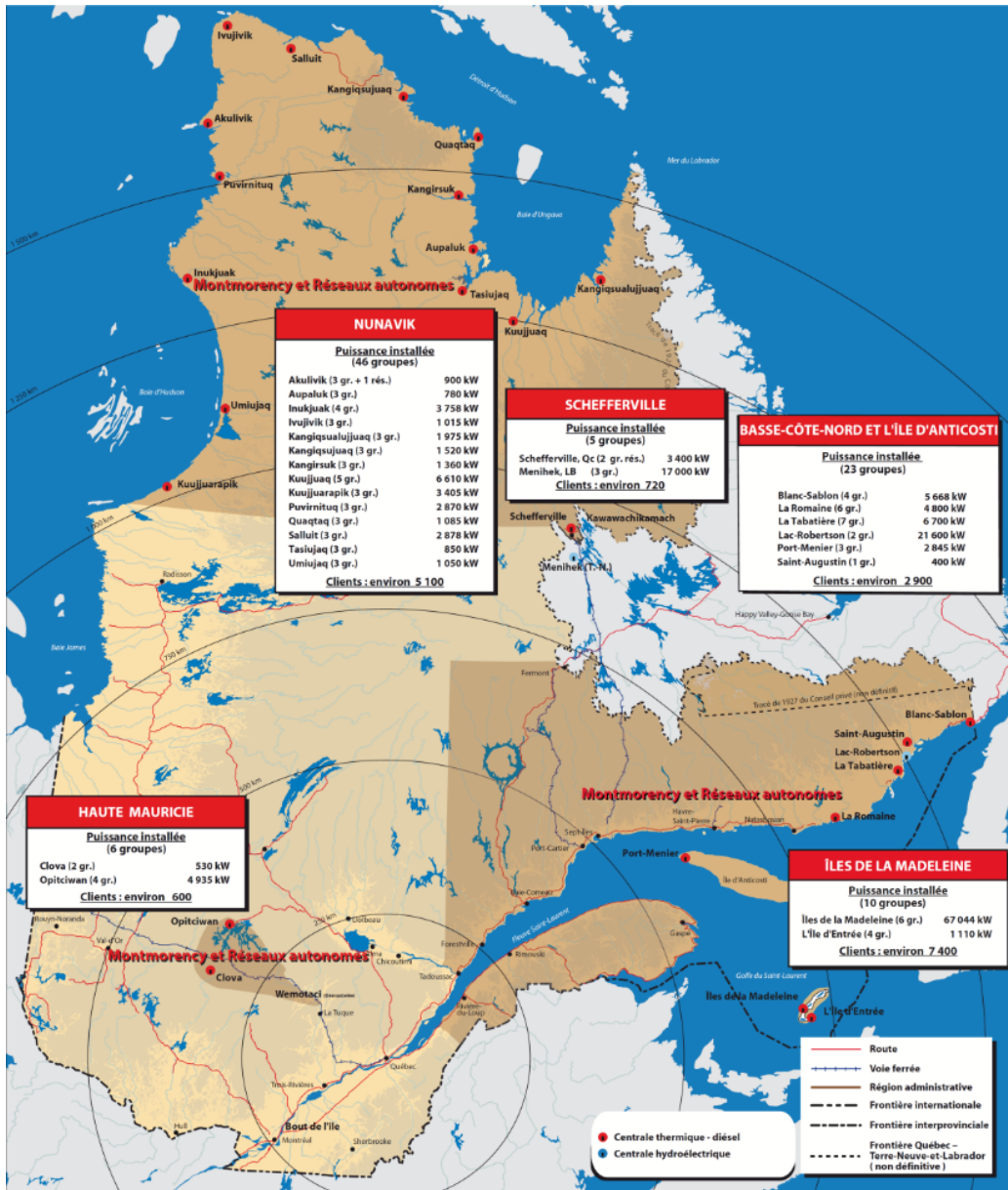


Figure 1.1 Remote communities in Quebec [3].

Because of the issues mentioned above, renewable energy sources (such as wind, solar, and hydro) offer clean and reliable options for remote communities. Low negative environment effects, sustainability, and cost-effectiveness are some benefits provided by these energy sources. On the other hand, due to the stochastic nature of these renewable resources and the variable load characteristics of remote communities, the use of a hybrid diesel generator-renewable energy system is usually indispensable. Several renewable energy technologies are candidates for

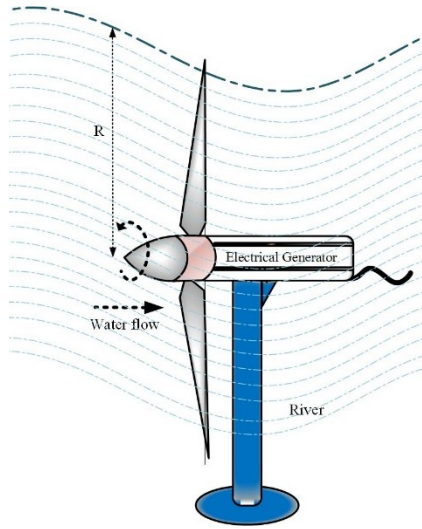
remote community applications. River hydrokinetic power is one of the most interesting alternatives. Kinetic power which can be captured from flowing water in rivers has a higher power density than the better-known renewable alternatives such as solar and wind power [6]. Table 1.1 shows that the power density of river current per square meter is higher than solar and wind sources [7]. Furthermore, it produces electricity without the requirement of constructing dams and the associated infrastructure when compared to conventional hydropower generation. Unlike other renewable sources, power generation during winter is a real challenge [8].

Table 1.1 Relative power density of river current compared with the wind and solar sources.

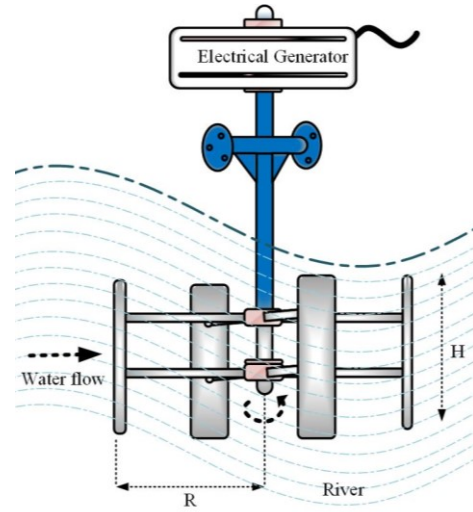
<b>Energy source</b>	<b>River current</b>			<b>Wind</b>	<b>Solar</b>
<b>Velocity(m/s)</b>	1	2	3	13	Peak at noon
<b>Power density (kW/m<sup>2</sup>)</b>	0.52	1.74	4.12	1.37	~1.0

In Canada, hydrokinetic power is still in the pre-commercialization and experimental stage. Québec’s potential hydrokinetic power is estimated to be around 5,250 MW [9]. The expected cost of electricity generated by a hydrokinetic turbine is projected to be around 0.15 \$/kWh [9], including the initial cost, the mounting hardware cost, the operating and maintenance cost. This is cheaper than the power supplied by genset that costs about 0.80 \$/kWh, including fuel and initial expenses [3], [4].

Figure 1.2 shows the two most common small-scale (1-100 kW) hydrokinetic turbines (HKTs); axial flow and cross-flow HKTs. Table 1.2 lists some advantages and disadvantages of both cross-flow and axial-flow turbines [8], [10], [11]. This research work focuses on the fixed-pitch cross-flow HKTs in which rotor blades of the HKT are fixed at a pitch angle.



(a) Axial-flow HKT



(b) Cross-flow HKT

Figure 1.2 Two most common small-scale HKTs.

Table 1.2 Turbine configurations for hydrokinetic application; advantages and disadvantages [8], [10], [11].

Turbine configurations	Advantages	Disadvantages
<p><b>Axial-flow</b> <b>(Horizontal axis)</b></p>	<ul style="list-style-type: none"> <li>• Self-starting capability.</li> <li>• Optimum performance at higher rotor speed.</li> <li>• Active control by blade pitching.</li> </ul>	<ul style="list-style-type: none"> <li>• High generator coupling cost.</li> <li>• Ducts cannot be easily used for a floating purpose.</li> </ul>
<p><b>Cross-flow</b></p>	<ul style="list-style-type: none"> <li>• Less generator coupling costs compared to horizontal axis turbine.</li> <li>• Allows to have flexible farm architectures</li> <li>• Operating under bi-directional water flow and shallow channel.</li> </ul>	<ul style="list-style-type: none"> <li>• less efficient than axial flow turbines</li> </ul>

## 1.2 The Potential of Diesel-Hydrokinetic Microgrid

A diesel-hydrokinetic (D-HK) microgrid consists of at least one hydrokinetic energy conversion system (HKECS) and one diesel generator set (diesel genset). The D-HK microgrid can [12]

- Reduce CO<sub>2</sub> emissions and fossil fuel consumption,
- Improve power quality of the electrical grid with respect to “hydrokinetic only” operation,
- Provide power to meet the customer load,
- Obtain the benefits of using multiple distributed electrical resources (DERs).

A D-HK microgrid can contain several subsystems as shown in Figure 1.3. In this microgrid, both the HKECS and the diesel genset supply the load demand. The diesel genset usually regulates the system’s voltage and frequency [13] and the HKECS works like a negative electrical load. A dump load is used to dissipate the excess power generated by generators and to maintain the power balance of the grid. An energy storage system may be necessary to enhance energy usage, to avoid wasting power in dump loads, and to allow generators to operate at maximum efficiency. The classification and sizing of components of such a hybrid system depend on several factors such as the availability of hydrokinetic power, e.g., minimum, maximum and average available power in kW, the pattern of the diesel genset loading, the pattern of load demand, etc. It should be mentioned that the selection of the components for such a small-scale microgrid depends on its own particular requirements and design constraints such as power quality, availability, system reliability, simplicity of maintenance, etc. [14].

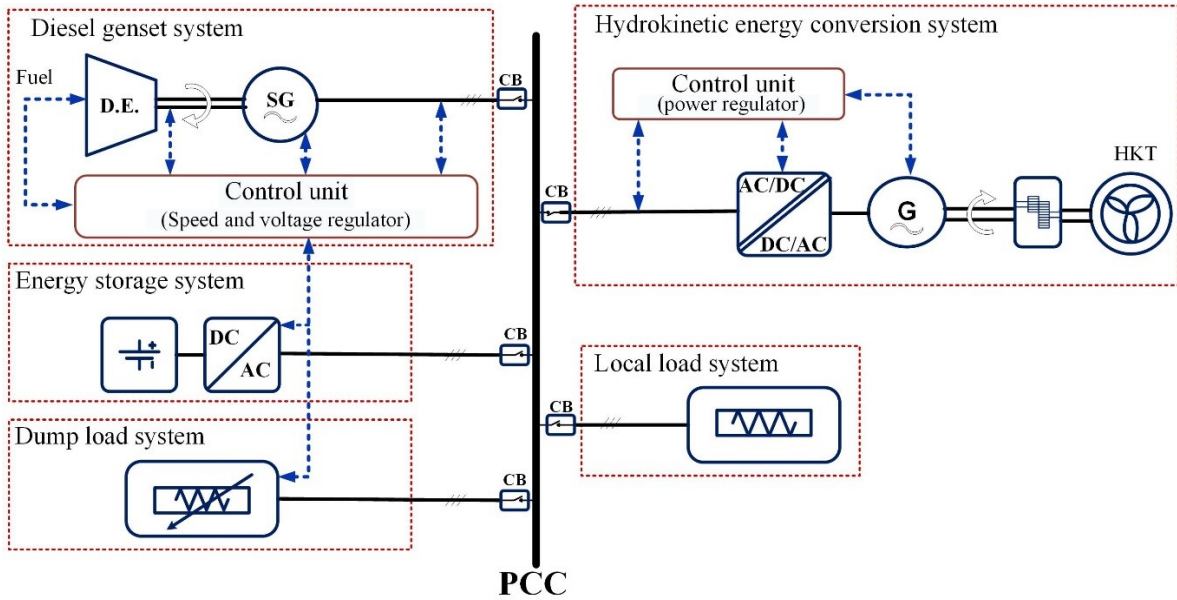


Figure 1.3 D-HK microgrid.

### 1.2.1 Characteristics of the D-HK Microgrid

In this Section, a brief overview of the technical features of D-HK microgrids are explained. The power vs. water speed curve of an HKECS is similar to that of a wind energy conversion system (WECS). In fact, many of the power topologies and control techniques used for WECSs can be extended for HKECSs [15], [16].

The output power of an HKT is a function of the cube of the water speed of a river [6]. Water speed depends on several factors such as the channel cross-section, river channel profile, climate conditions (i.e., snow melting, rainfall, etc.), the HKT placement (i.e., mounting arrangement, augmentation channel, etc.), etc. [10]. Speed of the water in a river has seasonal/long-term and turbulence/short-term variations [17], [18]. Figure 1.4 shows a short-time water speed profile for a sample river [19]. The Water speed measured along the Winnipeg river, Manitoba at a constant depth, approximately 1.5 m. The average water speed was measured to be 2.45 m/s, with a standard deviation of 0.67 m/s. Moreover, hydrokinetic power is directly proportional to the density of water. The water density depends on climate conditions and varies from freshwater to seawater [10]. In general, the hydrokinetic power trends are difficult to forecast particularly for the short-term trends. Water speed in a river usually changes between 1m/s and 3m/s [20].

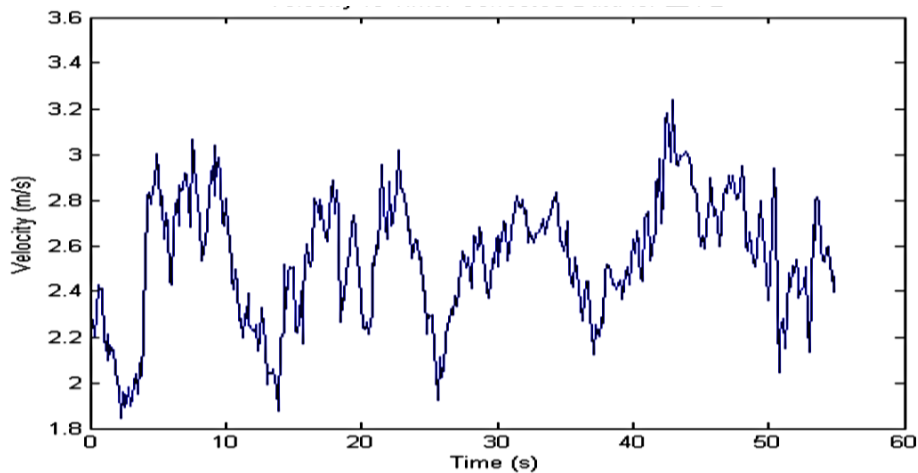


Figure 1.4 Water speed measured along the Winnipeg river, Manitoba at a constant depth, approximately 1.5 m [19].

Remote community load patterns exhibit short-term and long-term trends. They depend on several factors such as the season and environmental conditions and the local economy. However, they are relatively simple to forecast since they track the community's habit. With the knowledge of load patterns, a suitable electrical generator can be selected to provide a proper power supply [12].

The genset can operate either continuously or intermittently in the microgrid [14], [21], [22], [23]. In the latter case, the genset works for short periods, e.g., a few hours at a time, supplying electric power. Integration of the HKECS power into an existing diesel-powered microgrid is however, not straightforward due to the variable nature of the water speed. While under moderate and high penetration of the HKECS power, the HKECS may be able to supply all of the demanded power, sudden variations in the water speed or demand need the intermittent (standby) genset to step in rapidly to guarantee continuity of supply. The simplest way to integrate the HKECS with the genset, without the risk of loss of load, is parallel operation of the HKECS with the genset running continuously. In this mode of operation, the HKECS acts like a negative load, thus decreasing the average load of the diesel engine. The diesel genset responds quickly to electrical load variations to regulate the frequency and voltage of the grid within an acceptable range. This thesis focus on the continuous operation of the genset.

Energy storage systems play an important role to ensure continuity of supply in a microgrid. In the microgrid, the integration of a storage unit can

- reduce short-term fluctuations in the hydrokinetic power and/or consumer load for improvement of the grid power quality (short-term storage),
- reduce start/stop cycles of the genset and fuel consumption (short to medium-term storage),
- balance hydrokinetic power or local load surplus (long-term storage) [12], [24].

Energy storage units can be categorized by overall energy capacity, energy density per mass, average service lifetime, cost, etc. Batteries, flywheels, and hydrostatic storage are some storage systems. The storage system is one of the more expensive parts of the hybrid system and need a sophisticated control scheme. Therefore, they require a careful examination of the benefits and drawbacks. Storage-less system has lower implementation cost and less complexity [12]. A storage-less D-HK microgrid is assumed in this research work.

### **1.2.2 Power Control Considerations for HKECS**

Similar to the wind turbine (WT), an HKT can operate at fixed speed or variable speed [6], [25]. Typically, the generator of a fixed speed turbine is directly connected to the grid and runs at a rotor speed which is set by the grid frequency. An induction generator is usually selected for the fixed-speed applications. The system uses a well-established technology which is simple, inexpensive and reliable. However, despite the advantages, limited power control, lower efficiency, torque pulsations due to power fluctuations, and power quality problems in the small-scale microgrid are some drawbacks of this scheme [26]. Use of a variable speed turbine can mitigate some of these problems.

In a variable speed scheme, the turbine rotor speed can be adjusted as a function of water speed. The torque and speed of the electrical generator change so that the turbine's operating point varies. The turbine usually works at the maximum power point tracking (MPPT) mode or constant power mode (CPM) for operation above the rated water speed. The power control can be obtained by blade pitch control and generator speed control. Pitch regulated control is however not possible for most HKTs. This is the case for the cross-flow turbines considered in this research which have non-pitchable blades [6], [10]. For the HKECS with a permanent magnet synchronous generator (PMSG), a generator-side converter unit (connecting the generator to a generic DC bus) is usually responsible for the generator torque or speed control. In

this case, the power regulation, start-up, and shutdown mechanisms must be carried out with generator speed control [27]. Besides, for low-speed applications, the gearbox, which is used to step-up the shaft speed of the turbine, can be eliminated by using a PMSG with a large number of poles. This topology is more complicated than the fixed speed topology due to the requirement of power electronic converter and sophisticated control scheme.

### **1.3 Technical Issues in Small-Scale Storage-Less D-HK Microgrid**

A low level of hydrokinetic power penetration can be handled by conventional diesel genset control system. Medium or large levels of hydrokinetic power penetration can have negative impacts on the short-term (transient) and long-term (steady-state) performance of the small-scale storage-less D-HK microgrid due to the stochastic nature of water speed and variable load patterns. The conventional control scheme of the HKECS is the maximum power point tracking (MPPT) control.

In long-term conditions, under moderate and high penetration of the HKECS, the diesel genset can operate at a poor efficiency where the role of the HKECS is to reduce the electrical load on the diesel genset (light loading) [28]. The fuel consumption of typical diesel engines at no-load is about at 20-30% of the full load value and increases linearly with loading. Moreover, diesel engine manufacturers recommend a minimum load of approximately 40% of rated output to maintain high fuel efficiency, to avoid wet stacking, etc. [29], [30]. Considering the minimum loading of the diesel engine, one option is the HKECS to operate in MPPT mode and the power flow of the system balanced by the genset and the dump load. Another option is the dump load off, and the HKECS and the diesel genset regulate their output powers to balance the load demand as well as mitigate minimum load operating effects on the diesel engine. In both cases, the diesel genset usually regulates the system frequency and voltage. The fixed-pitch hydrokinetic turbine-generator can regulate its output power according to the turbine power coefficient in the low-speed (stall) region (below MPPT point) or high-speed region (above MPPT point). However, power generation in the stall region is a real challenge and require sophisticated control strategies since this region is open loop unstable. A review of power control strategies for fixed-pitched wind/ hydrokinetic turbines in the stall region available in the literature are presented in Chapter 2 and Chapter 3.

For short-term conditions, the way of balancing the power system in the short operational time (i.e. several seconds) is primarily due to the stochastic nature of the water speed and the variable load characteristics. During this time, the frequency of the grid may vary. This can lead to power quality problems (e.g. high rate of change of frequency or power, frequency fluctuations, etc.) in each rotating machine especially for the synchronous generator of the diesel genset which is directly connected to the grid. There is an interest to provide the capability of contributing to the grid's frequency support control. A hydrokinetic turbine-generator with a relatively high moment of inertia or the inertia constant ( $H$ ) can release and absorb kinetic energy (KE) stored in its rotating parts (e.g. blades, generator shaft, etc.) during the frequency disturbance. For example, for a 50 kW HKT, the equivalent moment of inertia of is about 8407 kg.m<sup>2</sup> and the inertia constant is around 3s for the shaft speed of 6 rad/s. An inertia constant of 3 seconds indicates that the kinetic energy stored in the rotating parts can supply the nominal load during 3 seconds [31], [32]. Indeed, the key issue here is how to control the turbine-generator system so as to make good use of this resource for frequency support of the microgrid. A literature review of power and frequency support control for the diesel hybrid microgrid systems are presented in Chapter 2 and Chapter 5.

Another challenging issue is a hardware-in-the-loop (HIL) platform for testing and developing a D-HK microgrid. This can allow complex dynamic hybrid systems to be correctly emulated in a simple, repeatable, and economical way. Furthermore, this emulator can be used to evaluate new control schemes. There are two types of generator emulator: electromechanical-based emulator and converter-based emulator [33], [34]. A literature review of both emulators are given in Chapter 3 and Chapter 4.

## **1.4 Contributions**

The main objective of this work is to develop and design different active power control strategies for a small-scale storage-less D-HK microgrid. These can help mitigate concerns about the short-term and long-term technical issues as mentioned in the previous Section. Designing and prototyping an electromechanical and power electronic converter-based hardware-in-the-loop emulator for the diesel genset and HKECS are other objectives of this work. The contributions of this thesis are as follows;

- **Design and implementation of an electromechanical-based D-HK microgrid emulator**

An electromechanical-based D-HK microgrid emulator is implemented. This emulator is used to experimentally validate and demonstrate the proposed control strategies in a laboratory-scale setting where the operation of a real HKT and a diesel engine is unfeasible.

- **Development of a supervisory power control strategy for a fixed-pitch PMSG-based HKT operating in the stall region**

A new dispatchable power controller for a fixed-pitch HKT with PMSG followed by a diode rectifier and a boost DC-DC converter is presented. A supervisory controller along with a cascaded outer power and inner diode rectifier voltage loop control system is proposed to obtain smooth transition between power regulation and MPPT modes.

- **Development of power and frequency support control for a storage-less D-HK microgrid**

An active power sharing control strategy for a storage-less D-HK microgrid with medium and high penetration of hydrokinetic power to mitigate: 1) the effect of the grid frequency fluctuation due to instantaneous variation in the water speed/load, and 2) light loading operation of the diesel engine is proposed. A supplementary control loop that includes virtual inertia and frequency droop control is added to the conventional control system of HKECS in order to provide load power sharing and frequency support control.

- **Development of a converter-based PMSG emulator as a testbed for renewable energy experiments**

A converter-based PMSG emulator as a testbed for designing, analysing, and testing of the generator's power electronic interface and its control system is presented. A 6-switch voltage source converter is used as a power amplifier to mimic the behaviour of the PMSG supplying linear and nonlinear loads.

This research study resulted in the following technical publications and presentations:

### **Journals**

- M. Ashourianjozdani, L. A. C. Lopes and P. Pillay, "Power Electronic Converter-Based PMSG Emulator: A Testbed for Renewable Energy Experiments," *IEEE Transactions on Industry Applications*, 2018. (Accepted)

- M. Ashourianjozdani, L. A. C. Lopes and P. Pillay, "Supervisory Power Control for Dispatchable Fixed-Pitch PMSG-Based Hydrokinetic Energy Conversion System," (under review, submitted to *IEEE Transaction on Industrial Applications*)
- M. Ashourianjozdani, L. A. C. Lopes and P. Pillay, "Power and Frequency Support Control for a Storage-less Diesel-Hydrokinetic Microgrid," (prepared for submitting to *IEEE Transaction on Sustainable Energy*)

## Conferences

- M. Ashourianjozdani, L. A. C. Lopes and P. Pillay, "Converter-Based PMSG Emulator: A Testbet for Renewable Energy Experiments", IEEE International Conference on Electric Machines and Drive Conference (IEMDC), Miami, 2017.
- M. Ashourianjozdani, L. A. C. Lopes and P. Pillay, "Power Sharing Control Strategy for a No-Storage Hydrokinetic-Diesel System in an Isolated AC Mini-Grid", IEEE International Conference Power and Energy Society General Meeting (PESGM), Boston, 2016.
- M. Ashourianjozdani, L. A. C. Lopes and P. Pillay, "Power Control Strategy for Fixed-Pitch PMSG-Based Hydrokinetic Turbine", IEEE International Conference on Power Electronics, Drives and Energy Systems (PEDES), Trivandrum, 2016.
- M. Ashourianjozdani, L. A. C. Lopes and P. Pillay, " A Laboratory-Based Hydrokinetic-Diesel Energy Conversion System Emulator ", 7th International Conference on Integration of Renewable and Distributed Energy Resources (IRED), Niagara Falls, 2016. (Poster Presentation)
- M. Ashourianjozdani, L. A. C. Lopes and P. Pillay, "A Hybrid Hydrokinetic-Diesel Energy Conversion System for Remote Applications", IEEE International Conference Power and Energy Society General Meeting (PESGM), Denver, 2015. (Poster Presentation)

## 1.5 Thesis outline

This thesis is organized as follows.

**Chapter 1** discusses the research area and some related works. It presents a review of characteristics of a D-HK microgrid. The advantages and disadvantages of such system are highlighted. Some technical issues of this system are discussed. This chapter ends with the contributions of the research work and the structure of the thesis.

**Chapter 2** presents the mathematical models of the main component of a storage-less hybrid hydrokinetic-diesel system. Some advantages and disadvantage of three common power

converter topologies used for the HKECS are discussed are discussed. Some simulations are conducted to validate the performance of models.

**Chapter 3** proposes a supervisory power control for a dispatchable fixed-pitch PMSG-based HKECS, operating in the stall region. The performance of the proposed control algorithm is verified experimentally with an electromechanical-based HKT emulator.

**Chapter 4** proposes a converter-based PMSG emulator. The design procedure and implementation of the emulator are discussed. The accuracy of the proposed emulator is investigated for the fundamental and low order voltage harmonics. Technical challenges are considered, and proper solutions are suggested.

**Chapter 5** proposes a new power sharing control strategy for a storage-less D-HK microgrid to provide steady-state and transient frequency support control and improve the operation of the diesel engine under light loading conditions. The proposed strategy is experimentally verified with an electromechanical-based HKT and diesel engine emulator.

**Chapter 6** concludes the work and suggests some recommendations and future works.

## **1.6 Summary**

This chapter has provided a discussion of the research area and some related works. A review of the characteristics of a storage-less D-HK microgrid has been presented. Advantages and disadvantages of such microgrid have been highlighted. The research targets and objectives have been defined. The contributions of the research as well as list of publications have been presented. The chapter ends with the structure of the thesis.

## Chapter 2. Theory, Modeling and Design Considerations of Diesel-Hydrokinetic Microgrid

*This chapter presents a theoretical background for the diesel-hydrokinetic (D-HK) microgrid. The steady-state and dynamic models of the HKECS and diesel genset are developed. The most recent works relevant to this subject are explored. Some technical issues related to control and operation of the HKECS and diesel gensets are explained. Simulation results are presented to show the performance of the system using Matlab<sup>®</sup> Simulink.*

### 2.1 Structure and Operation of HKECS

Figure 2.1 shows a block diagram of the HKECS structure. The kinetic energy of the flowing water is transferred to electrical energy through a HKT and an electrical generator. The power electronic interfaces (PEIs) control the output power of the generator and deliver the electrical power to the electrical grid or local load. The PEIs convert variable voltage and variable frequency input to a fixed voltage and fixed frequency output. To explain the HKECS behavior, some principles are extracted from the WECS because of many shared similarities in their physical principles.

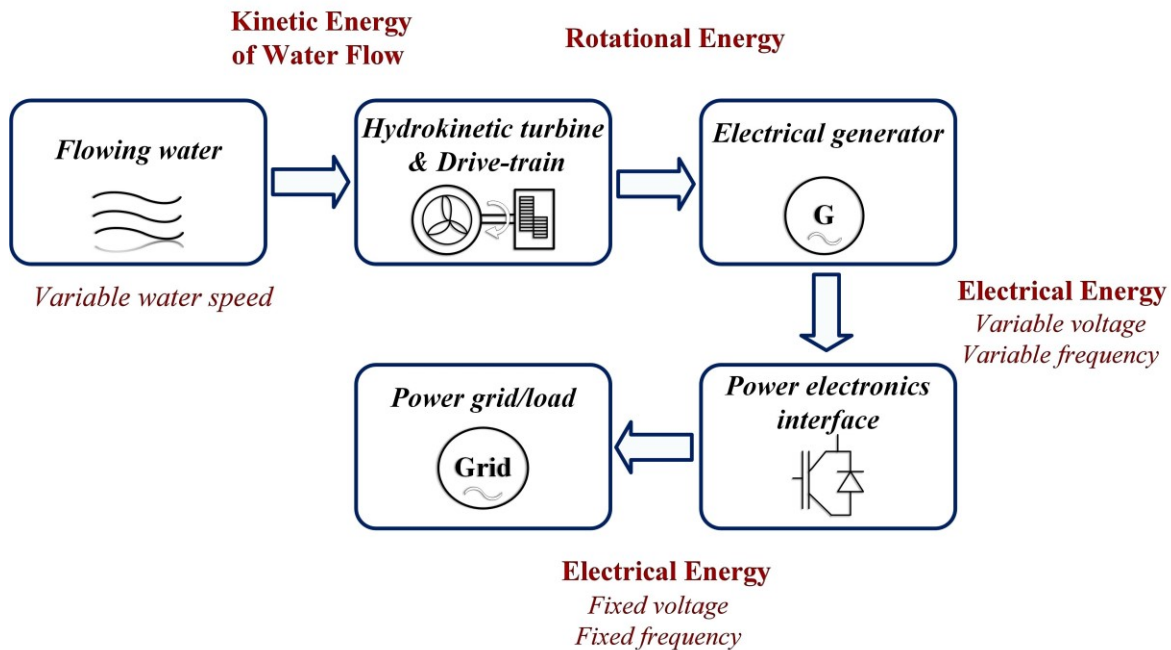


Figure 2.1 Block diagram of the HKECS structure.

### 2.1.1 Hydrokinetic Turbine (HKT)

The total power captured by an HKT depends on the density, cross-sectional area, cube of the water speed and turbine coefficient. The power and the torque generated by a fixed pitch HKT are described by [35]:

$$P_{HKT} = 0.5 \rho A C_p(\lambda) v_T^3 \quad (2.1)$$

$$T_{HKT} = \frac{P_{HKT}}{\omega_m} = 0.5 \rho A C_q(\lambda) v_T^2 \quad (2.2)$$

where  $A$  is cross-sectional area of the turbine,  $\rho$  is the density of water,  $v_T$  is the speed of water,  $\omega_m$  is the turbine shaft speed (rotor speed),  $C_p$  is the turbine power coefficient or efficiency, and  $C_q$  is the turbine torque coefficient. The factor  $C_p$  indicates that the HKT can only capture a portion of the total available kinetic power of the flowing water because of losses involved. Power and torque coefficients are a nonlinear function of the tip speed ratio ( $\lambda$ ), which is defined by:

$$\lambda = \frac{R\omega_m}{v_T} \quad (2.3)$$

where  $R$  is the radius of the turbine. The power and torque coefficients for the fixed-pitch cross-flow HKT considered in this work can be given by [27]:

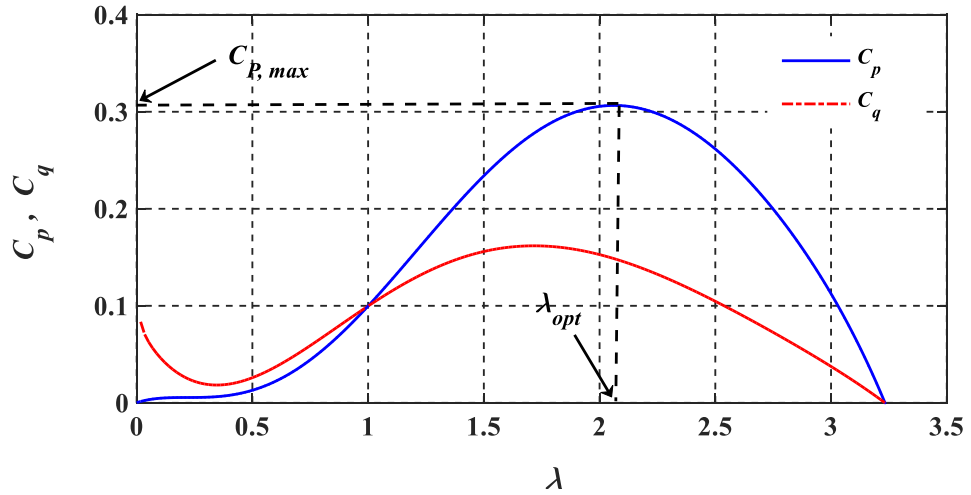
$$C_p(\lambda) = \sum_{i=0}^7 a_i \lambda^{7-i} \quad (2.4)$$

$$C_q(\lambda) = \frac{C_p(\lambda)}{\lambda} \quad (2.5)$$

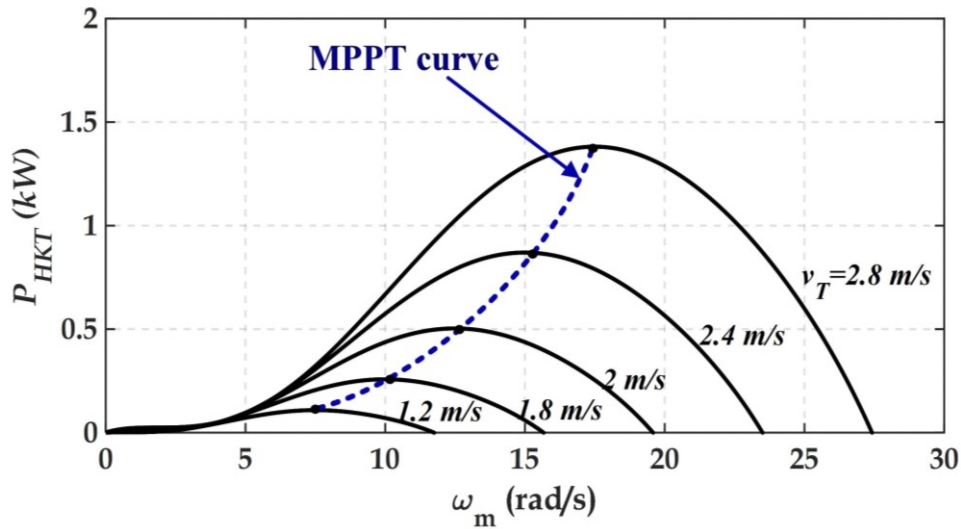
where  $a_i$  are constant values.

Figure 2.2 (a) shows  $C_p$  and  $C_q$  versus  $\lambda$  for the selected fixed-pitch cross-flow HKT. The constant values ( $a_i$ ,  $i = 0, 1, 2, 3, 4, 5, 6, 7$ ) are given in Appendix A. The maximum value of  $C_p$  and corresponding tip speed ratio ( $\lambda_{opt}$ ) are around 0.31 and 2.1, respectively. The maximum

value of  $C_q$  is around 0.16 at  $\lambda = 1.72$ . According to equation (2.1), the output power of the HKT for a given water speed can be reduced to a desired value by decreasing the power coefficient  $C_p$ . This can be done by operating at either below or above  $\lambda_{opt}$ . Figure 2.2 (b) shows the calculated output power of a HKT at different water speeds and rotor speeds. It can be observed that the maximum power of the turbine across different water speeds follows the maximum power point tracking (MPPT) curve.



(a)



(b)

Figure 2.2 (a)  $C_p$  and  $C_q$  versus  $\lambda$  curves; (b) HKT power versus turbine shaft speed ( $\omega_m$ ) at different water speeds ( $v_T$ ).

### 2.1.2 Drivetrain System

The total HKT power can be transmitted to the PMSG by a drivetrain system. The term “drivetrain” system for the HKECS mainly involves all rotating parts between the turbine and the generator including the HKT rotor blades and shaft, the gearbox with both low-speed and high-speed shafts, the generator shaft, and coupling shafts which connect two shafts together at their ends [28]. The gearbox is used to increase the low speed of the HKT to the high speed of the PMSG. The drivetrain can be modeled with different methods depending on the purpose of the study. The HKECS drivetrain is commonly modeled as a lumped single-mass model or a two-mass model [28], [33]. In the lumped single-mass model, the drivetrain components are lumped together and work as a single rotating mass. Neglecting the gearbox losses and inertia, and the flexibility of the coupling shafts, the dynamic equation of the single-mass drivetrain referred to the turbine side can be given by

$$\frac{d\omega_m}{dt} = \frac{T_{HKT}}{J} - \frac{T_{ePMSG}'}{J} - \frac{B}{J} \quad (2.6)$$

where  $J$ ,  $B$ , and  $T_{ePMSG}'$  are the total system inertia, the total system friction damping, and the generator electromechanical torque reflected to the turbine side of the gearbox, respectively.  $T_{HKT}$  and  $\omega_m$  can be related to the generator electromechanical torque  $T_{ePMSG}$  and the generator rotor speed  $\omega_g$  by the gearbox with a gear ratio  $g_r$ : 1, as given by

$$g_r = \frac{T_{HKT}}{T_{ePMSG}} = \frac{\omega_g}{\omega_m} \quad (g_r > 1) \quad (2.7)$$

$J$  and  $B$  can be calculated by

$$J = g_r^2 J_{PMSG} + J_{HKT} \quad (2.8)$$

$$B = g_r^2 B_{PMSG} + B_{HKT} \quad (2.9)$$

where  $J_{PMSG}$  and  $J_{HKT}$  are the moment of inertia of the generator and the turbine, and  $B_{PMSG}$  and  $B_{HKT}$  is the friction damping of the generator and the turbine, respectively.

When considering the flexibility of the coupling shafts, the drivetrain can be modeled as a two-mass drivetrain. The two-mass drivetrain dynamic model is given in Appendix B.

### 2.1.3 Electrical Generator, PMSG

The PMSG is an attractive option for the small-scale fixed-pitch hydrokinetic systems compared to other electrical generators such as induction generators [36]. A PMSG with large number of poles can eliminate the requirement of the gearbox and operate with a high-power density. A PMSG's output voltage and frequency are variable and proportional to the rotor speed. So, it requires a power electronic converter to link the PMSG to the electrical load or the grid.

Figure 2.3 shows the equivalent circuit of the PMSG in  $d$ -axis and  $q$ -axis frames [37]. The following equations represent the dynamic models of the PMSG.

$$\frac{di_{sd}}{dt} = -\frac{1}{L_d}v_{sd} - \frac{R_s}{L_d}i_{sd} + \frac{L_q}{L_d}pi_{sq}\omega_g \quad (2.10)$$

$$\frac{di_{sq}}{dt} = -\frac{1}{L_q}v_{sq} - \frac{R_s}{L_q}i_{sq} - \frac{L_d}{L_q}i_{sd}p\omega_g + \frac{1}{L_q}\psi_{PM}p\omega_g \quad (2.11)$$

$$\frac{d\omega_g}{dt} = \frac{T_{mec}}{J_{PMSG}} - \frac{T_{ePMSG}}{J_{PMSG}} - \frac{B_{PMSG}\omega_g}{J_{PMSG}} \quad (2.12)$$

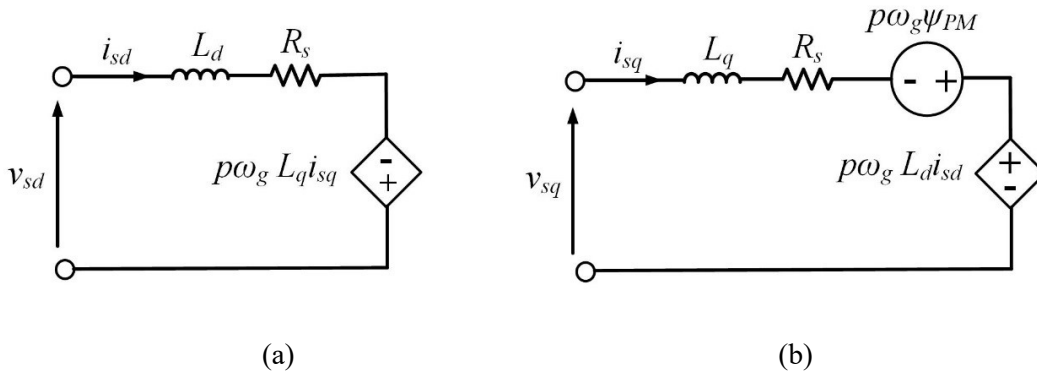


Figure 2.3 Equivalent circuit of the PMSG in  $d$ -axis and  $q$ -axis frames.

where  $v_{sd}$  and  $v_{sq}$  are the stator voltages,  $i_{sd}$  and  $i_{sq}$  are the stator currents,  $L_d$  and  $L_q$  are the equivalent inductances of stator windings in  $dq$ -frame, respectively.  $R_s$  is the stator resistance,  $\omega_g$  is the generator mechanical rotor speed,  $\psi_{PM}$  is the flux linkage produced by the permanent magnets, and  $p$  is the number of pole pairs.  $T_{mec}$  is the mechanical input torque which is equal to  $T_{HKT}/g_r$  for a single-mass drivetrain.  $J_{PMSG}$  and  $B_{PMSG}$  are the system moment of inertia and damping of the generator, respectively.

The electromagnetic torque is equal to:

$$T_{ePMSG} = 1.5p(\psi_{PM}i_{sq} - (L_q - L_d)i_{sd}i_{sq}) \quad (2.13)$$

For constant flux operation when  $i_{sd}$  equals to zero, the electromagnetic torque is equal to

$$T_{ePMSG} = 1.5p\psi_{PM}i_{sq}, \Rightarrow T_{ePMSG} = K_T i_{sq} \quad (2.14)$$

where  $K_T$  is the generator torque constant.

#### 2.1.4 Control Strategies for Fixed-Pitch HKT

Figure 2.4 shows the power coefficient versus rotor speed at a constant water speed for a fixed-pitch HKT. The turbine can work in either the low-speed (stall) region (section I), the MPPT point or the high-speed region (section II).

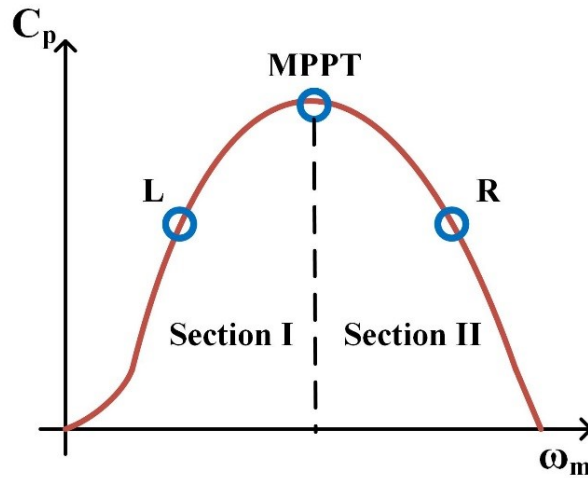


Figure 2.4 the power coefficient ( $C_p$ ) versus rotor speed ( $\omega_m$ ) for a constant water speed ( $v_T$ ).

**Low-speed (stall) region:** in this region, the output power of the HKT varies between zero and the maximum available power, while its rotor speed changes from zero to MPPT speed. Since the turbine rotor speed can be zero, one can implement the shutdown procedure in this region. For a fixed-pitch HKT, the shutdown procedure includes reducing the shaft speed to zero by controlling generator speed, and then applying the mechanical braking system at zero rotor speed. It is highly recommended to stop the rotor turbine when the water speed is very high to avoid electrical and mechanical problems [28]. However, direct power control in this region requires a sophisticated control scheme because of the inherent instability characteristics of the HKT [27], [38]. From nominal water speed to the maximum water speed (cut-off speed), the output power must be limited to the rated value of the HKT; an operation mode called a constant power mode (CPM). The transition between the MPPT and the CPM at rated water speed is important. During this transition, the rotor speed should be limited to the rated level to keep centrifugal forces below values tolerated by the rotor [25]. However, based on the application of HKT turbine in the power system, the selection of operating parameters such as the nominal water speed and the cut-off water speed can change during the design procedure [39].

**MPPT point:** the MPPT algorithm extracts maximum power from the HKT. In MPPT operation, the generator speed controller regulates the rotor speed ( $\omega_m$ ) so that the turbine rotates at the optimal tip speed ratio for various water speeds. The rotor turbine speed changes linearly with the water speed through the MPPT operation. Usually, if the MPPT is used, it begins from the cut-in water speed and finishes at the rated water speed as shown in Figure 2.2 (b). The cut-in speed is the speed at which the turbine and generator begin rotating and generating power.

Table 2.1 gives a summary of some MPPT algorithms available in the literature [40], [41], [42]. The MPPT methods can be broadly classified into searching algorithms, optimal curve characteristic techniques, and the combination of searching and optimal curve methods. Advantages and disadvantages of each method are mentioned in Table 2.1. In this research, an optimal curve characteristic method such as power signal feedback (PFS) will be used because of its simple and satisfactory steady-state and dynamic performance. This method can later be improved to take advantage of the combination of searching and optimal curve characteristics algorithms. A diode rectifier followed by DC-DC converters (boost type) or active rectifiers are

the most common power converter structures suggested in the literature to implement the MPPT procedure for the PMSG speed control.

Table 2.1 A summary of some MPPT algorithms used in the HKECS.

<b>MPPT Methods</b>	<b>Features</b>
<b>Searching method such as hill climbing searching (HCS)</b>	<p><b>Advantages:</b></p> <ul style="list-style-type: none"> <li>• Does not require any prior knowledge of the system characteristics.</li> <li>• Can be implemented without using water speed sensor.</li> </ul> <p><b>Disadvantages:</b></p> <ul style="list-style-type: none"> <li>• Its performance significantly deteriorates under rapidly change of water speed.</li> <li>• The speed of convergence and the efficiency of the MPPT depends on the perturbation step size.</li> <li>• Oscillations are unavoidable in the HCS control.</li> </ul>
<b>Optimal curve characteristics methods such as power signal feedback (PSF), tip speed ratio (TSR), etc.</b>	<p><b>Advantages:</b></p> <ul style="list-style-type: none"> <li>• Very fast and efficient</li> <li>• Satisfactory steady-state and dynamic characteristics</li> <li>• A-priori system specific knowledge is required.</li> </ul> <p><b>Disadvantages:</b></p> <ul style="list-style-type: none"> <li>• The non-constant efficiencies of the generator-converter subsystems can result in the deviation of the actual optimum points from the stored data.</li> <li>• Cannot be used together with variable-pitch control or stall region control.</li> </ul>
<b>Combination of searching and optimal curve characteristics</b>	<p><b>Advantages:</b></p> <ul style="list-style-type: none"> <li>• Fast tracking capability under high rate of change of water speed conditions</li> <li>• Does not require any prior knowledge of the system characteristics</li> <li>• Water speed measurement is not required</li> </ul> <p><b>Disadvantages:</b></p> <ul style="list-style-type: none"> <li>• Require a complex control procedure</li> </ul>

**High-speed region:** in this region, the output power of the HKT can change from the MPPT value to zero, while the rotational speed operates above the MPPT speed. During very low power operation, the turbine rotor speed is much higher than the MPPT speed, which may lead to the problem of over-speed [27] during high water speeds. The PMSG/turbine must work below the rated value of the rotor speed. However, some control strategies exist in the literature regarding the operation of the turbine in this region [43], [44], [45]. The rated value of the generator rotor speed is increased when the operation of the HKT in the high-speed region is desirable. In this region, the turbine operates at a deloading (DL) mode by decreasing turbine power efficiency, obtained with the help of generator power/torque control [44]. The HKECS can contribute to frequency support control and active power sharing of the microgrid by adding power reserves obtained from the deloaded turbine and the stored kinetic energy in the rotating parts to the grid during a disturbance, e.g., a sudden load change. Ignoring losses, Figure 2.5 shows the HKECS power flow while increasing the load power  $P_{load}$  and the HKT working in section II. The load power increase should trigger a speed reduction to increase the HKT power  $P_{HKT}$  and decrease stored mechanical power  $P_{mech}$  at the same time. Therefore, the load power increase is compensated by releasing the stored kinetic energy and converting to electrical energy. The DL percentage should be determined based on prevailing water speed and the maximum allowable limit of the generator rotor speed [45]. Furthermore, it is important to use an appropriate control strategy to control rotor speed so that sufficient stored power is injected into the microgrid.

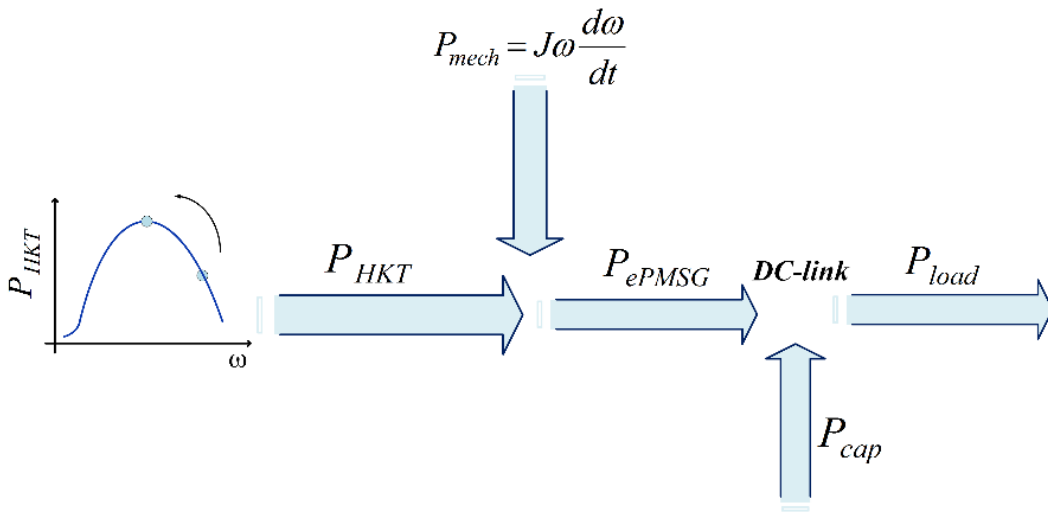


Figure 2.5 HKECS power flow during deceleration when HKT works in section II.

### 2.1.5 HKECS Power Electronic Interfaces

A PMSG is commonly connected to a load/grid through a power electronic interface (PEI), which usually includes a generator-side and a grid/load-side converter. The generator-side and grid-side converter are connected back-to-back through a DC-link capacitor. Control strategies of the grid-side and the generator-side can be developed based on HKECS and grid requirements. Figure 2.6 shows three most common generator-side configurations that can be used with the PMSG in low voltage (LV) operations where voltages are below 1000V [46]. A 2-level voltage source inverter (2L-VSI) is selected for the grid-side converter. A review of these configurations used in the literature is given in following sections.

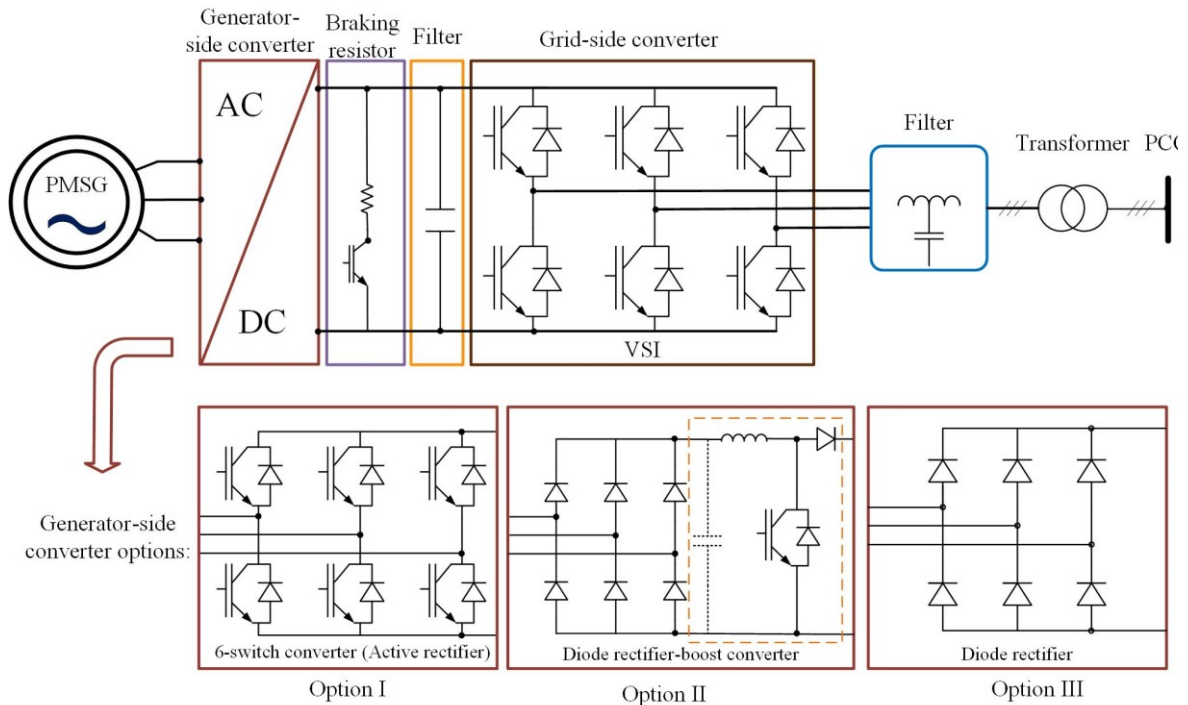


Figure 2.6 Different generator-side converter topologies.

#### 2.1.5.1 Option I: 6-switch converter and 2L-VSI

In this option, a 6-switch converter (active rectifier) and a 2L-VSI are connected through the DC-link capacitor. The PMSG can operate with a variable rotor speed and power factor control by using the 6-switch converter as the generator-side converter. This converter usually controls the torque (or speed) of the PMSG by controlling  $dq$ -frame currents ( $i_{sd}$  and  $i_{sq}$ ). In this case, the

torque (or speed) of the PMSG is controlled with  $i_{sq}$ , while  $i_{sd}$  can be kept at zero [47]. Figure 2.7 shows the schematic diagram of the PMSG controller based on the 6-switch converter in the  $dq$ -frame. The current feedback signals are converted from  $abc$  to  $dq$ -frame using the Park transformation and passed through the controllers to generate the required control signals. Then, control signals are converted from  $dq$  to  $abc$ -frame and delivered to the pulse width modulation (PWM) inverter [37]. Park transformation and its inverse are given in Appendix B. Although the six-switch converter makes the control scheme more complicated and sensitive than the simple structures such as the diode rectifier, it provides a full-scale control for the PMSG. Moreover, the harmonic distortion developed in the output current of the generator is lower than the diode rectifier structures. Also, the generator losses can be minimized by optimal control of the  $d$ -axis stator current [48]. Another benefit of this topology is bi-directional operation, which can help starting up the turbine system [27].

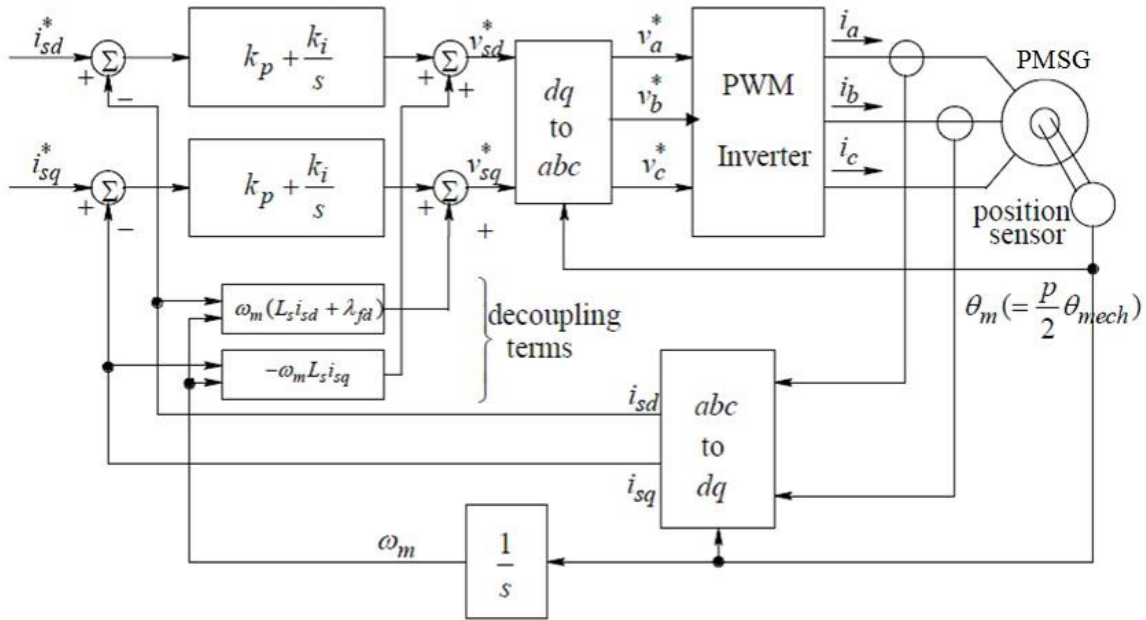


Figure 2.7 PMSG controller in  $dq$ -frame [37].

The grid-side converter is controlled so as to transfer the available DC-link power into the grid. The controller can be designed to operate as a current-controlled voltage source inverter (CC-VSI) or voltage-controlled voltage source inverter (VC-VSI) [49]. The CC-VSI serves to control the active and reactive power generated to the grid based on desirable power factor while

VC-VSI makes desirable output voltage and frequency at the load side for a stand-alone operation.

Figure 2.8 shows the schematic diagram of the 2-level CC-VSI and its electronic interface. It essentially involves two cascaded control loops. An internal current loop is responsible for regulating the inverter output current and an external DC-link voltage loop (or power-flow controller) is used to balance the power flow into the intermediate DC bus [50]. The output current of the inverter and grid voltage are transferred from the  $abc$ -frame to the  $dq$ -frame using the Park transformation and a phase-locked loop (PLL) controller [51]. The PLL provides an estimation of the grid frequency and phase angle from the grid voltage.

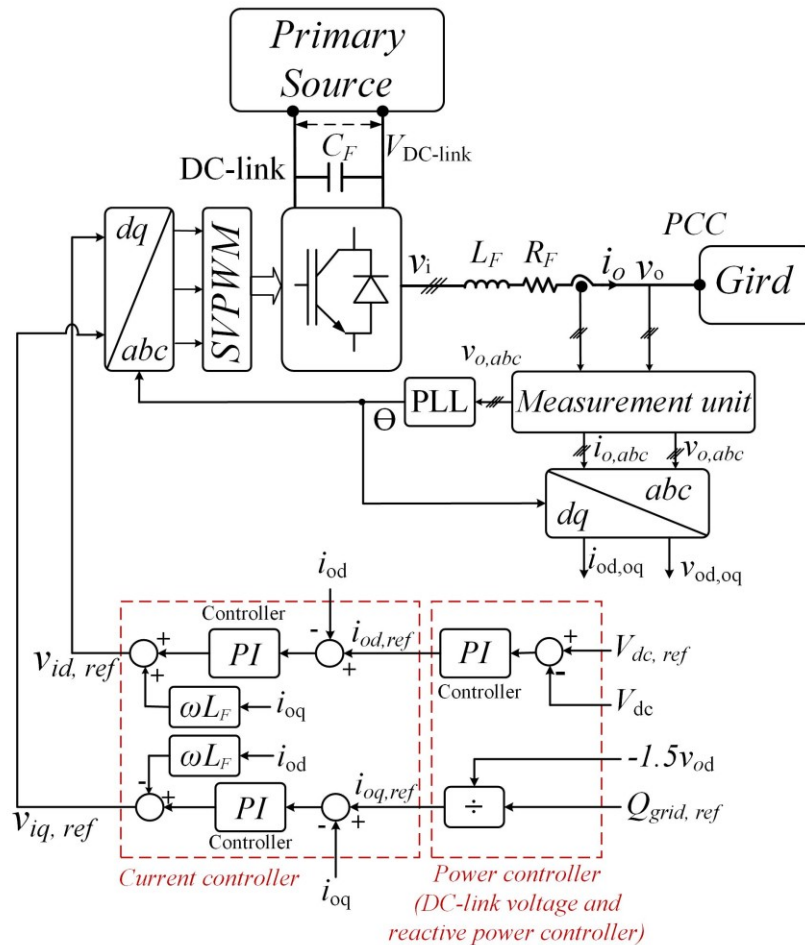


Figure 2.8 Schematic of CC-VSI and its electronic interface.

The AC-side dynamics of the CC-VSI in the  $dq$ -frame can be given by the following equations.

$$\frac{di_{od}}{dt} = -\frac{R_F}{L_F}i_{od} + \omega i_{oq} + \frac{v_{od}}{L_F} - \frac{v_{id}}{L_F} \quad (2.15)$$

$$\frac{di_{oq}}{dt} = -\frac{R_F}{L_F}i_{oq} - \omega i_{od} + \frac{v_{oq}}{L_F} - \frac{v_{iq}}{L_F} \quad (2.16)$$

where  $R_F$  and  $L_F$  are the resistance and inductance of the filter, respectively.  $(v_{od}, v_{oq})$ ,  $(v_{id}, v_{iq})$ , and  $(i_{od}, i_{oq})$  are the grid voltage, the output voltage of inverter, and the output current of inverter in the  $dq$ -frame, respectively.

According to equation (2.15) and (2.16), the control block diagram of the inner current loops of the CC-VSI in the  $dq$ -frame is developed and shown in Figure 2.9. In this figure, the closed-loop transfer function of the current control loop in the s-domain can be given as

$$G_{cil}(s) = \frac{i_o(dq)}{i_o(dq),ref} = \frac{G_i(s)G_{PWM}(s)}{sL_F + R_F + G_i(s)G_{PWM}(s)} \quad (2.17)$$

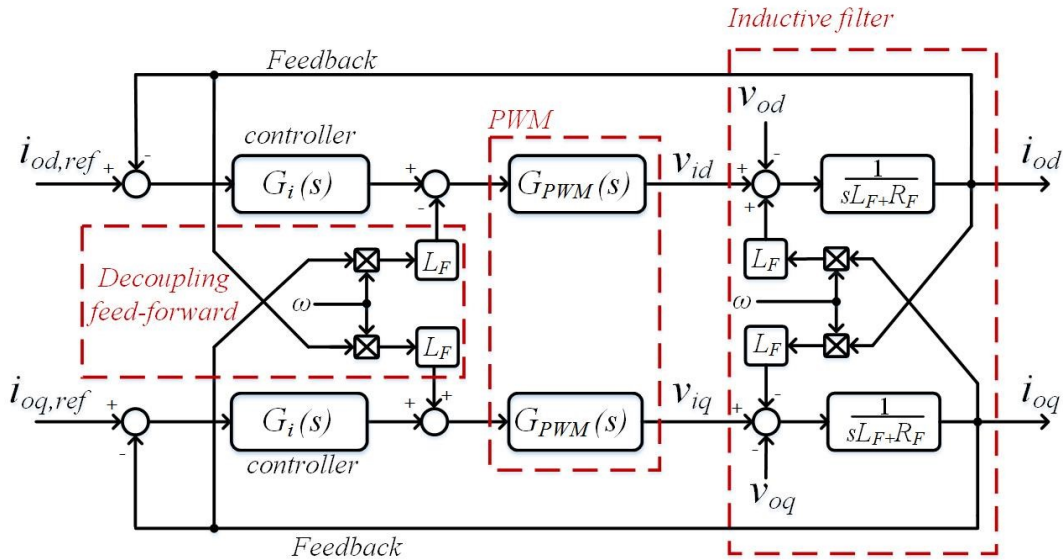


Figure 2.9 control block diagram of internal current controlled VSI in  $dq$ -frame.

$G_{PWM}(s)$  is the transfer function of the PWM inverter and it can be determined in the s-domain as

$$G_{PWM}(s) = \frac{M_{PWM}}{1 + s(T_s/2 + T_D)} \quad (2.18)$$

where  $M_{PWM}$  is the gain of the PWM block,  $T_s$  is the controller sampling time, and  $T_D$  is the inverter delay. The current controller  $G_i(s)$  is a proportional-integral (PI) type controller whose transfer function is given by

$$G_i(s) = K_{pc} + \frac{K_{ic}}{s} \quad (2.19)$$

where  $K_{pc}$  and  $K_{ic}$  are the proportional and integral gains of the PI controller. The PI controller gains are designed so that  $G_{icl}(s)$  yields a unity DC gain and an adequate bandwidth with a rejection of high-frequency disturbances. Setting  $K_{pc}$  and  $K_{ic}$  to  $L_F/\tau_i$  and  $R_F/\tau_i$ , respectively, then,  $G_{icl}(s)$  can be approximated as the first-order transfer function [50]

$$G_{cil}(s) = \frac{1}{\tau_i s + 1} \quad (2.20)$$

where  $\tau_i$  is the time-constant of the current controller.  $\tau_i$  represents the bandwidth of the current control loop and is a design choice. Here, the bandwidth of the current control loop is designed one-tenth of the inverter switching frequency  $f_{sw}$ . The current controller parameters are designed for a 1.2 kHz bandwidth and a  $73^\circ$  phase margin. The Bode plot of the open-loop and closed-loop of the inner current control are shown in Figure 2.10. From the closed-loop plot, the gain at a frequency of 0.1 Hz (low frequency) is 0 dB with a phase of  $0^\circ$  and the bandwidth (3 dB below its magnitude at DC) is about 1.2 kHz.

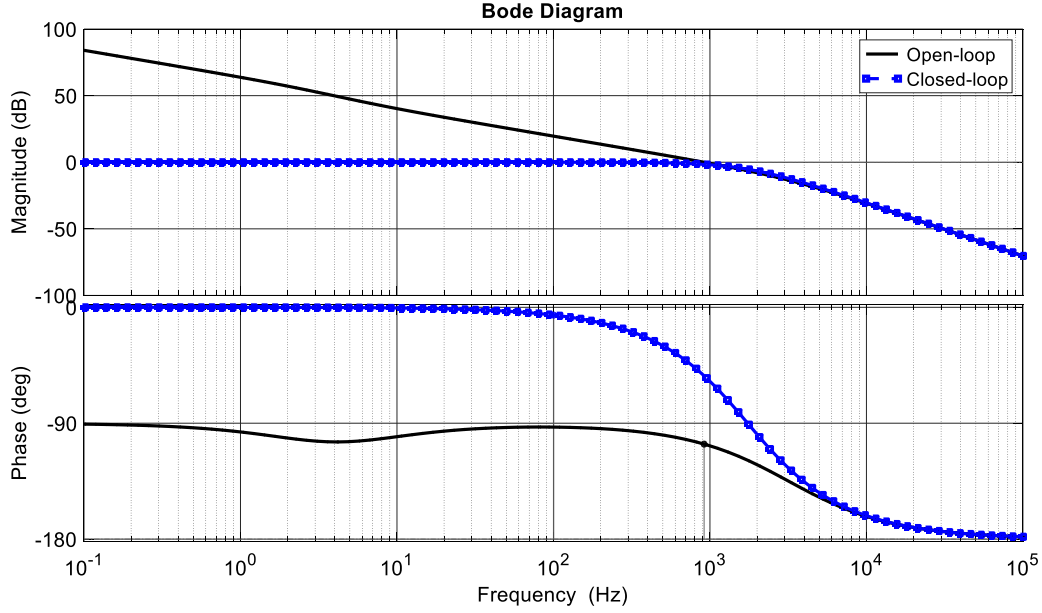


Figure 2.10 Bode plot for closed-loop and open-loop current controller. VSI parameters:  $R_F = 0.1 \Omega$ ,  $L_F = 2 \text{ mH}$ ,  $\tau_i = 0.0008 \text{ s}$ ,  $M_{PWM}=1$ ,  $T_s = 80 \text{ } \mu\text{s}$ ,  $T_D = 20 \text{ } \mu\text{s}$ .

The output active and reactive power of the inverter in  $dq$ -frame can be given as [50]

$$P_{grid} = \frac{3}{2} (v_{od} i_{od} + v_{oq} i_{oq}) \quad (2.21)$$

$$Q_{grid} = \frac{3}{2} (v_{oq} i_{od} - v_{od} i_{oq}) \quad (2.22)$$

To obtain a decoupled active and reactive power control scheme of the CC-VSI, the  $d$ -axis voltage  $v_{od}$  is aligned with the grid voltage as shown in Figure 2.11. Therefore,  $v_{od}$  is equal to grid voltage magnitude  $|V_o|$ , and the resultant  $q$ -axis voltage  $v_{oq}$  is equal to zero. So, the equation of (2.21) and (2.22) can be simplified as

$$P_{grid} = \frac{3}{2} |V_o| i_{od} \quad (2.23)$$

$$Q_{grid} = -\frac{3}{2} |V_o| i_{oq} \quad (2.24)$$

From (2.24), the  $q$ -axis current reference  $i_{oq,ref}$  is obtained as

$$i_{oq,ref} = \frac{Q_{grid, ref}}{-1.5|V_o|} \quad (2.25)$$

where  $Q_{grid, ref}$  is the reactive power reference, which can be set to zero, a negative value, and a positive value for unity power factor operation, leading power factor operation, and lagging power factor operation, respectively. The generated active power is represented by the  $d$ -axis current reference  $i_{od,ref}$ . It is produced by a PI controller for the DC-link voltage control. The controller (DC-link controller) is chosen to have slower response than the inner current control loop. The controller gains were selected using MATLAB control system toolbox in order to obtain a zero steady-state error to a step reference signal and desired bandwidth and phase margin. Here, a bandwidth of 100 Hz and  $73^\circ$  phase margin is selected to provide a good DC-link voltage regulation. The controller gains are given in Appendix A.

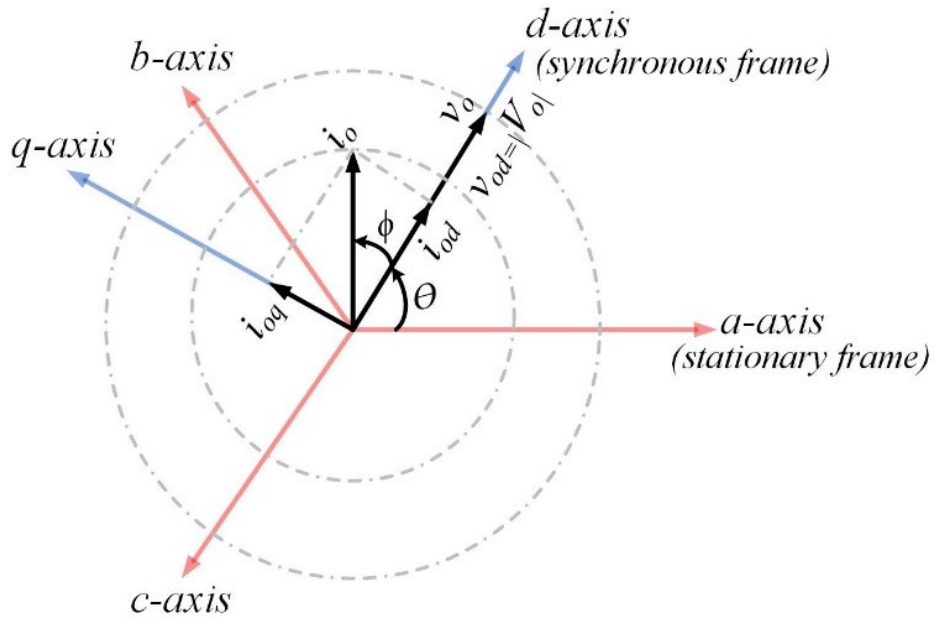


Figure 2.11 Space vector diagram CC-VSI control scheme.

The control task of the generator-side and grid-side converters may also change based on their application. In [52], the function of the generator-side converter is to regulate the DC-link voltage while the grid-side converter controls the active and reactive power injected into the grid,

independently. This method of control is suitable for the direct drivetrain multi-pole PMSG to damp the torsional oscillations actively in the drivetrain whenever the system gets excited, i.e., during water speed fluctuations.

- Synchronous reference frame PLL

Figure 2.12 shows the block diagram of the PLL system implemented based on three-phase synchronous reference frame (SRF) [53]. It provides an accurate frequency and phase angle estimation of the grid voltage. The basic concept of the SRF-PLL is explained in [53]. For a balanced three-phase system when the PLL is locked, the  $q$ -axis voltage decreases to zero. When the PLL is not locked, the  $q$ -axis voltage is not zero and it has a small error. So, a closed-loop control system using a PI controller is applied on the  $q$ -axis voltage to remove steady-state error and then to lock the PLL.  $f_o$  is the frequency feedforward which is set at the nominal frequency, e.g. 60 Hz. Figure 2.13 shows the performance of the PLL under both a phase jump of  $90^\circ$  and an increment step change of the grid frequency from 60 Hz to 59 Hz at 0.6 s. The applied proportional and integral gains of the PI controller were 2500 and 3200, respectively. It is shown that the locked AC voltage and estimated voltage phase angle are able to follow grid voltage and phase angle within 2 ms. Also, the grid frequency is estimated within 6 ms.

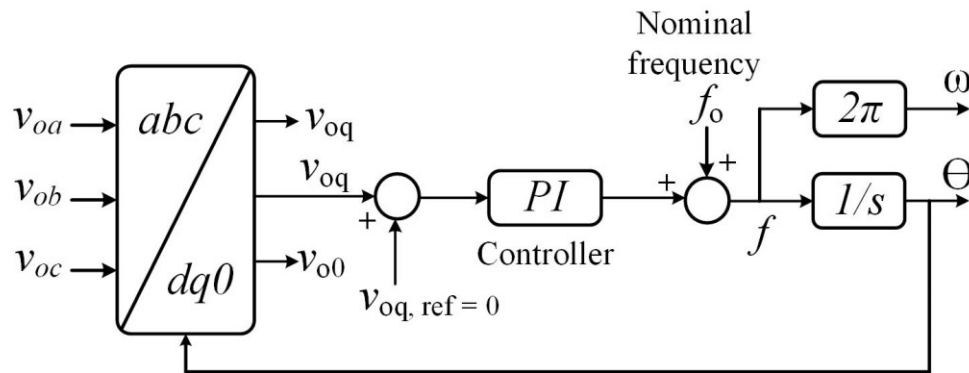


Figure 2.12 Block diagram of three phase SRF-PLL.

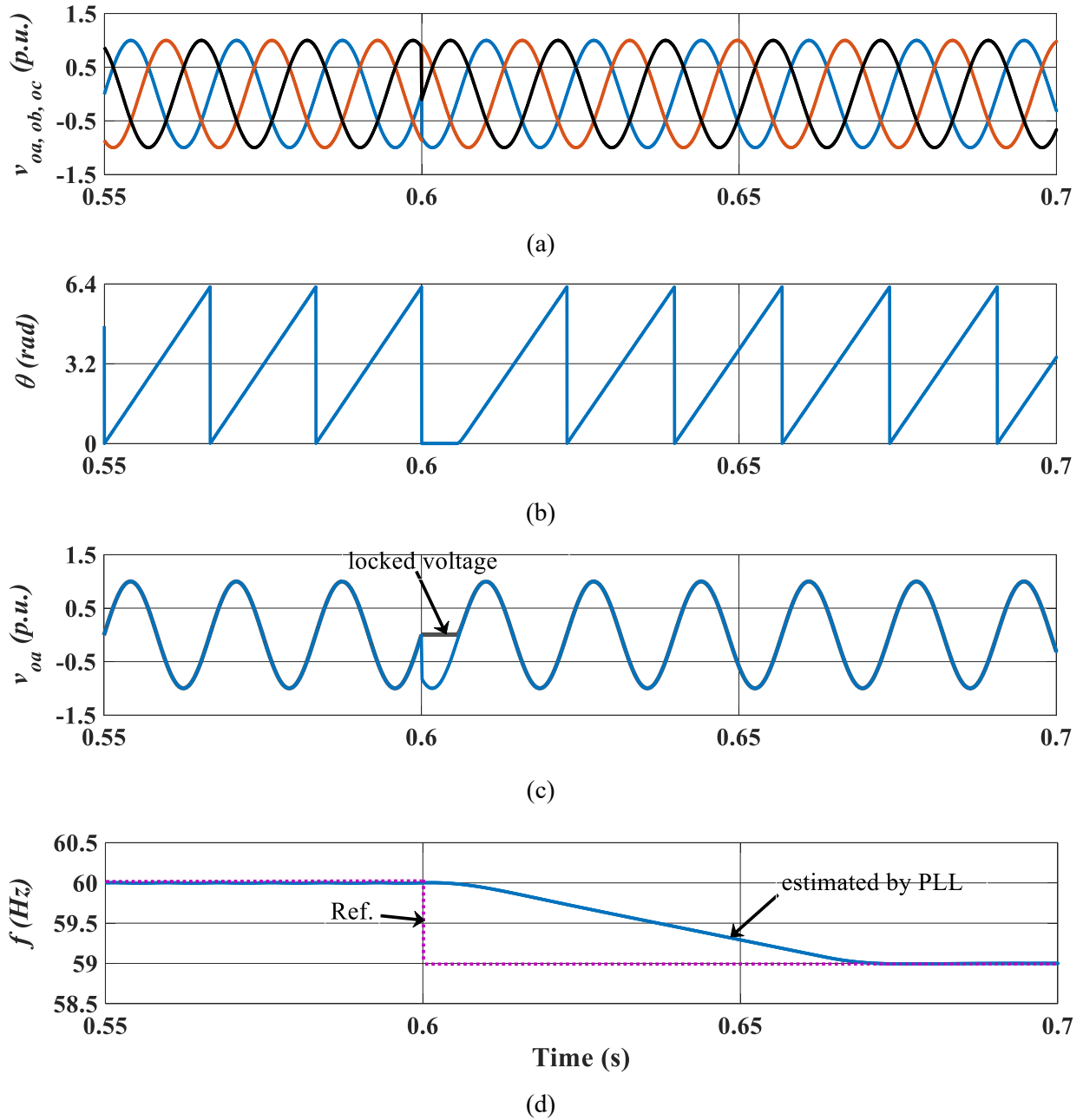


Figure 2.13 Simulation results of SRF-PLL performance under both a phase jump of  $90^\circ$  and a step change of frequency from 60 Hz to 59 Hz. (a) the grid voltage in  $abc$ -frame, (b) the phase angle of the grid voltage, (c) input ideal and locked grid voltage, and (d) the grid and estimated frequency.

### 2.1.5.2 Option II: diode rectifier, DC-DC converter (boost type) and 2L-VSI

Compared to the 6-switch converter and the 2L-VSI, this topology is simpler, cheaper and its control strategy has the benefits of lower parameter sensitivity and lower switching losses [54]. However, harmonic distortion including both low and high switching-frequency harmonics is developed in the output current of the generator. They cause power losses in the generator. Moreover, it is impossible to obtain the optimal current control such as loss-minimization control and flux-weakening control for the PMSG [21]. It increases the output voltage of the diode-rectifier to a higher level which is appropriate for the VSI operation. Therefore, this topology improves the performance of the HKECS, especially during low water speeds. The grid-side converter can work to control the injected active and reactive power into the grid, or to regulate the output voltage and frequency at the load side of a stand-alone operation, as explained in previous section.

For the PMSG connected to a diode rectifier, the per-phase equations in balanced steady-state operation are [37]

$$V_s = E_g - I_s(R_s + jp\omega_g L_s) \quad (2.26)$$

$$E_g = K_E \omega_g \quad (2.27)$$

$$T_{ePMSG} = K_T I_s, \quad K_T = \frac{3}{2} \sqrt{2} p \lambda_m \quad (2.28)$$

$$P_{ePMSG} = T_{ePMSG} \omega_g \quad (2.29)$$

where  $R_s$ ,  $L_s$ ,  $E_g$ ,  $V_s$ ,  $I_s$ ,  $\lambda_m$ , and  $\omega_g$  are the stator resistance, the stator inductance, the back electromotive force (back-EMF), the generator terminal voltage, the generator line current, the flux linkage produced by the permanent magnets, the generator electrical speed of rotor, and the generator mechanical speed of rotor, respectively.  $p$  is the number of pole pairs.  $K_T$  and  $K_E$  are the torque constant and the back-EMF constant, respectively.  $P_{ePMSG}$  and  $T_{ePMSG}$  are the generator output power and the electromechanical torque, respectively.

Neglecting the power losses, the average values of the output voltage, current and power of the diode rectifier in steady-state conditions are approximately given by

$$V_{dc} = \frac{3\sqrt{6}}{\pi} V_s \quad (2.30)$$

$$I_{dc} = \frac{\pi}{\sqrt{6}} I_s \quad (2.31)$$

$$P_{dc} = V_{dc} I_{dc} \approx P_{ePMSG} = 3V_g I_g \approx P_{HKT} (V_T, \omega_m) \quad (2.32)$$

From equation (2.26), (2.27), and (2.30)  $V_{dc}$  can be deducted as

$$V_{dc} = \frac{3\sqrt{6}}{\pi} K_E \omega_g - \frac{3\sqrt{6}}{\pi} I_s (R_s + jp\omega_g L_s) \quad (2.33)$$

From equation (2.33) , it is possible to obtain an approximation for  $V_{dc}$  as a function of generator rotor speeds and water speeds. Using the parameters listed in Appendix A, the theoretical relationship between output voltage of the diode rectifier and the generator rotor speed for various water speeds is obtained and shown in Figure 2.14. There one can observe that the  $V_{dc} - \omega_g$  relationship is approximately linear and can be expressed as

$$V_{dc} = K_V \omega_g \quad (2.34)$$

where  $K_V$  is the voltage constant. Equation (2.34) helps to implement a simple control scheme and to avoid the generator speed measurement [55]. With this method, the shaft speed of the PMSG/HKT can be regulated by adjusting the value of  $V_{dc}$ . This can be realized using the PWM DC-DC boost converter.

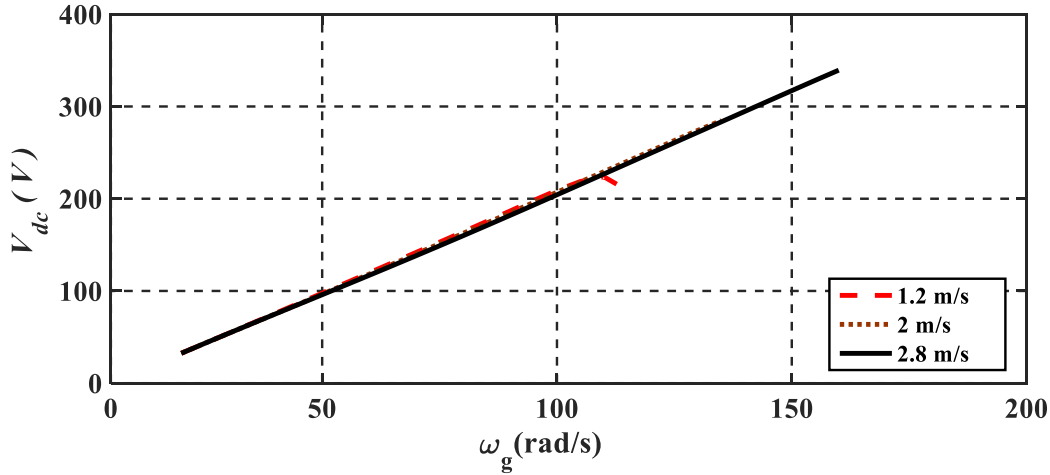


Figure 2.14  $V_{dc}$  vs. PMSG rotor speed  $\omega_g$  across various water speeds.

- Averaged model of the boost converter

The simplified circuit and nonlinear averaged model of the boost converter are shown in Figure 2.15 (a) and (b) [56]. The dynamics of the idealized boost converter can be described by the following equations:

$$\frac{di_{dc}}{dt} = \frac{1}{L_c} [\bar{v}_{dc} - d' \bar{v}_o] \quad (2.35)$$

$$\frac{d\bar{v}_o}{dt} = \frac{1}{C} [d' \bar{i}_{dc} - \frac{\bar{v}_o}{R}] \quad (2.36)$$

where  $v_{dc}$ ,  $i_{dc}$ ,  $v_o$ ,  $L_c$ , and  $C$  are the input voltage, the input current, the output voltage, the input inductor and the output capacitor of the DC-DC boost converter, and overbars denote average values.  $d' = 1 - d$ , where  $d$  is the duty cycle. From equation (2.15) and (2.16), if the output voltage is regulated by the grid-side converter at a given value, the input voltage as well as input current of the boost converter can be controlled through a feedback control system.

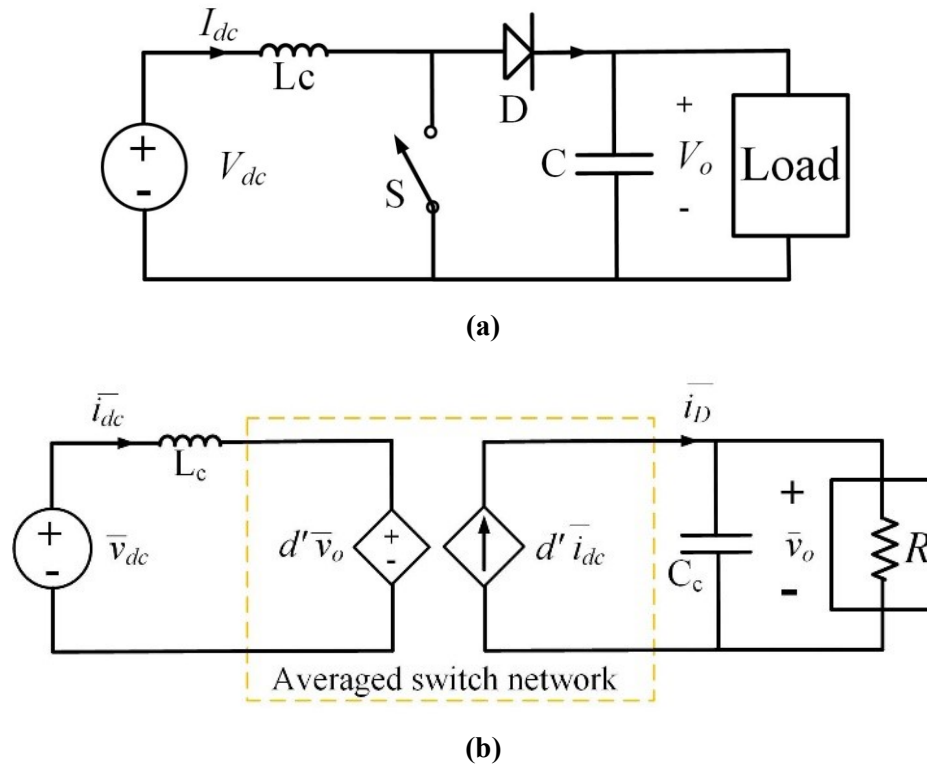


Figure 2.15 a) Simplified circuit of the boost converter, b) nonlinear averaged model of the boost converter.

Figure 2.16 shows simulation results of the HKECS when a PMSG is connected to a three-phase grid through a diode rectifier, a DC-DC boost converter and a 2L-VSI. The input mechanical torque of the PMSG is set at -15 N.m. The grid is 120 V L-L and 60 Hz. The function of the 2L-VSI is to regulate the DC-link voltage at 280 V while it regulates the output reactive power of the HKECS  $Q_{HKECS}$  at 0 VAR (unity power factor). Other simulation parameters are given in Appendix A. A step change from 0.5 to 0.6 at 20 s is applied to the duty cycle of the boost converter. Figure 2.16 (a) shows the input voltage  $v_{dc}$  and the output voltage  $V_{dc-link}$  of the boost converter. One can see that  $V_{dc-link}$  is regulated at 280 W while  $v_{dc}$  is changed from 140 V to 111 V according to the duty cycle change.  $v_{dc}$  decreases with increasing the duty cycle and vice versa. The HKECS output active and reactive power are shown in Figure 2.16(b). One can see that the generated active power is changed with duty cycle variation while the HKECS is controlled to operate at unity power factor. The fundamental waveforms of HKECS output current and grid voltage are also shown in Figure 2.16(c).

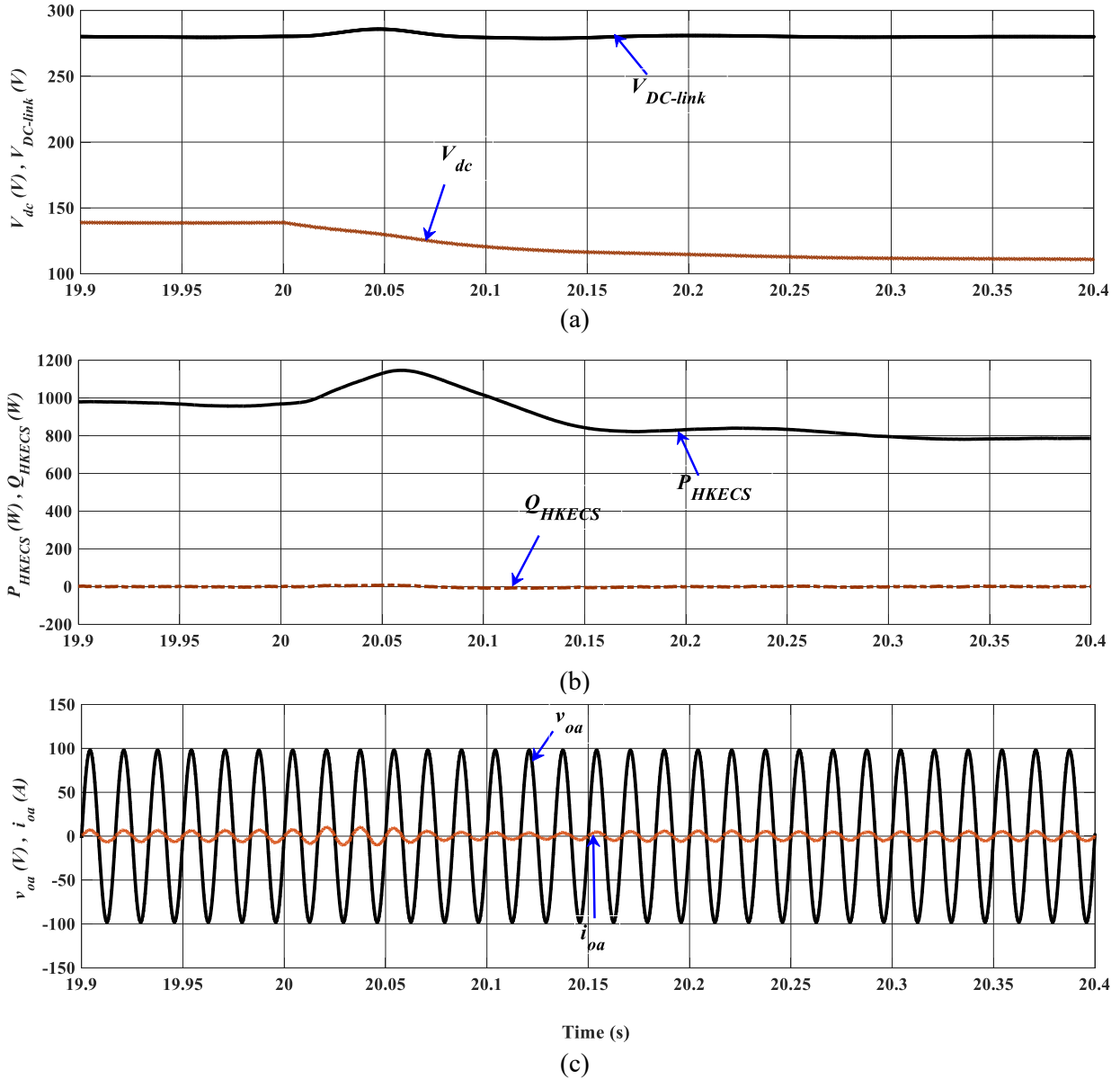


Figure 2.16 Simulation results of the power electronics interface performance of the HKECS performance for an increase step change from 0.5 to 0.6 in duty cycle of the boost converter. a) output voltage of diode rectifier and DC-link voltage b) output active and reactive power of the HKECS, c) output current and voltage of the HKECS.

### 2.1.5.3 Option III, diode rectifier + 2L-VSI

In this configuration, a DC-link capacitor links the diode rectifier and 2L-VSI as shown in Figure 2.6. This structure is simpler, cheaper and more reliable than the 6-switch converter and 2L-VSI [57]. The VSI controls the HKECS active and reactive power. In this way, the speed of

the PMSG can be controlled by the inverter output current/power. However, the magnitude of the DC-link voltage changes widely, which can lead to overvoltage, with potential damage to the equipment, and under voltage, with a loss of power control by the inverter. In [58], [59], and [60], a braking resistor or controllable DC load (CDCL) is suggested for assisting with the regulation of the DC-link voltage for overvoltage and active power curtailment (APC). To obtain the DC-link voltage regulation with the CDCL, sizing of braking resistor and capacitor is an important issue. The minimum DC-link voltage should be selected to be more than grid line voltage magnitude to operate the inverter properly. The DC-link voltage decreases when the equivalent resistance reduces. Sizing the capacitor depends on DC-link voltage ripple, voltage recovery time, and other factors.

Furthermore, the output voltage of the diode rectifier becomes relatively low during low water speeds. As mentioned earlier, the DC-link voltage must be higher than the grid line-line voltage magnitude. One alternative solution can be that the VSI absorbs reactive power from the grid to deal with this limitation [61]. Figure 2.17 shows the VSI vector diagram under unit power factor (UPF) and leading power factor (LPF) operation. Neglecting losses, for the constant output active power, the output voltage of the inverter can be lower than the grid voltage when the inverter works at the LPF. However, some issues such as the over-current of the converter and synchronous generator may limit this application. Another solution is using a gearbox. This helps to increase the shaft speed as well as DC-link voltage. However, the maintenance problem of the gearbox introduces another issue. Similar to the option II, high harmonic distortion develops in the output current of the generator due to the diode rectifier. It may cause heating issues, efficiency reduction, and torque ripple in the PMSG.

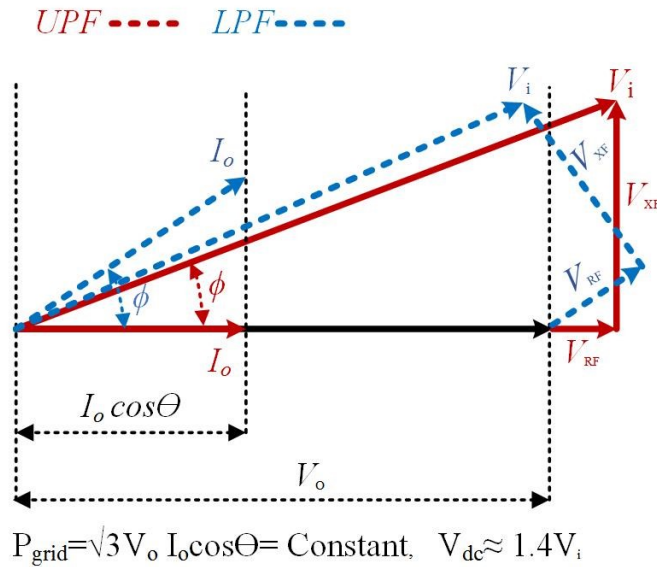


Figure 2.17 VSI vector diagram for unit power factor (UPF) and leading power factor (LPF) operation.

## 2.2 Diesel Generator Set

Figure 2.18 shows the diesel genset model. It includes five main components: a diesel engine as a prime mover, a coupling shaft, an electrical generator i.e. a synchronous generator, a speed governor, and automatic voltage regulator (AVR) [22]. The mathematical model of the genset subsystems are described in following sections.

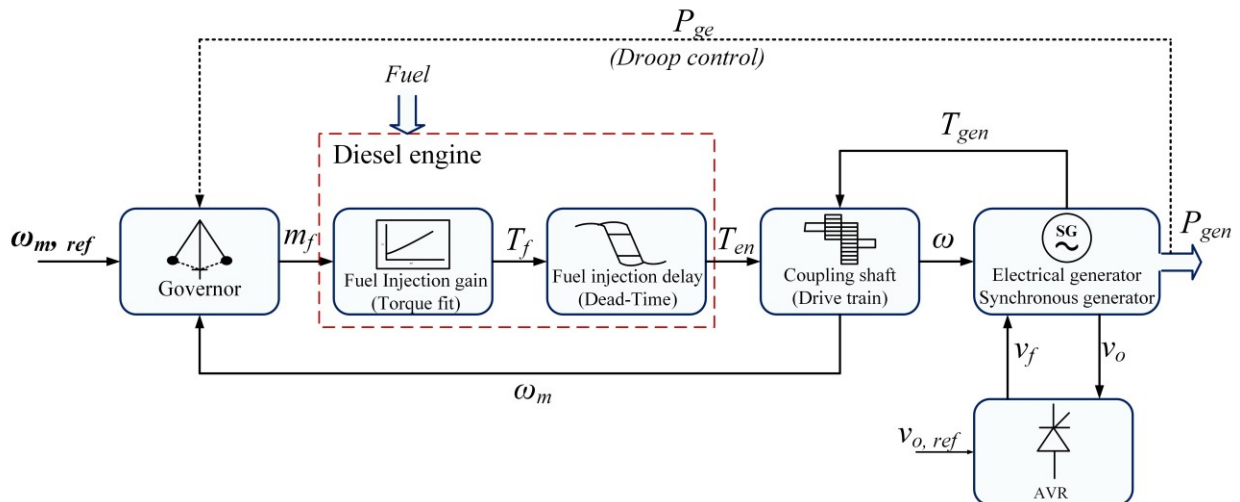


Figure 2.18 Diesel genset model.

### 2.2.1 Diesel Engine and Coupling Shaft

The mathematical model of the diesel engine consists of three main elements: fuel injection gain, fuel injection delay, and the inertia of rotating parts including the engine and flywheel [34], [62]. The fuel injection gain and delay model can be described as

$$T_{en} = T_f(m_f)e^{-\tau_s t} \quad (2.37)$$

where  $T_{en}$  is the engine mechanical torque and  $T_f$  is a nonlinear function of the diesel engine fuelling rate,  $m_f$ .  $\tau_s$  is dead-time of the diesel engine which depends on the engine characteristics. The shaft dynamic of the diesel engine torque and the generator can be represented by the mathematical equations similar to equation (2.6).

### 2.2.2 Electrical Generator

The genset is usually equipped with a wound rotor synchronous generator. It can be modeled in the  $dq$ -frame based on model 1.0 of IEEE Std. 1110-2002 [63], [34]. This model includes the dynamics of the field and stator circuits. The model equations are

$$\frac{di_{sd}}{dt} = -\frac{R_s}{L_s}i_{sd} + \omega_e i_{sq} - \frac{v_{sd}}{L_s} - \frac{L_m}{L_f} \frac{di_f}{dt} \quad (2.38)$$

$$\frac{di_{sq}}{dt} = -\frac{R_s}{L_s}i_{sq} + \omega_e i_{sd} - \frac{v_{sq}}{L_s} - \omega_e \frac{L_m}{L_f} i_f \quad (2.39)$$

$$\frac{di_f}{dt} = -\frac{R_f}{L_f}i_f + \frac{v_f}{L_f} - \frac{L_m}{L_f} \frac{di_{sd}}{dt} \quad (2.40)$$

where  $v_{sd}$ ,  $v_{sq}$  and  $i_{sd}$ ,  $i_{sq}$  are the stator voltage and currents in the  $dq$ -frame, respectively.  $R_s$  and  $L_s$  are the stator resistance and inductance,  $L_f$  is the field excitation circuit inductance and  $L_m$  is the mutual inductance between field circuit and the  $d$ -axis of the stator.  $v_f$  and  $i_f$  represent the excitation circuit voltage and current, and  $\omega_e$  is the electrical angular speed of the generator.  $\omega_e$  is synchronized with the generator shaft speed (mechanical)  $\omega_m$  as

$$\omega_m = \frac{\omega_e}{p} = \frac{2\pi f_e}{p} \quad (2.41)$$

where  $p$  is the number of pole pairs and  $f_e$  is the electrical frequency of the generator.

The active power, reactive power, electromagnetic torque generated by the synchronous generator based on the  $dq$ -frame parameters are given as [50]

$$P_{gen} = \frac{3}{2}(v_{sd}i_{sd} + v_{sq}i_{sq}) \quad (2.42)$$

$$Q_{gen} = \frac{3}{2}(v_{sd}i_{sq} - v_{sq}i_{sd}) \quad (2.43)$$

$$T_{gen} = \frac{P_{gen}}{\omega_m} = \frac{3}{2}n_{pp}L_m i_{sq}i_f \quad (2.44)$$

### 2.2.3 Speed Governor

The speed governor adjusts  $\omega_m$ , as well as  $\omega_e$ , after load turbulence on the diesel genset. It can operate either in an isochronous control mode or a droop speed control mode. In the isochronous mode,  $\omega_m$  will return to a reference speed set point after a load change. With the droop regulation, the droop control provides a reference speed for the governor control as a function of the diesel genset output power [64]. The reference generator shaft speed can be calculated as

$$\omega_{m, ref} = \omega_{m, nl} - m_1 P_{gen} \quad (2.45)$$

where  $\omega_{m, nl}$ ,  $P_{gen}$  and  $m_1$  are the no-load generator shaft speed (rad/s), the diesel genset output power (W), and the droop gain (rad/sW), respectively. With isochronous regulation, the droop gain is disabled ( $m_1=0$ ), and  $\omega_{m, nl}$  is set to a constant value, e.g., 188.49 rad/s (or 60 Hz for 4 poles machine).

Figure 2.19 (a) illustrates the speed governor block diagram. The governor speed structure is a PI controller with feedback of the actual shaft speed. The PI controller is designed to eliminate

the steady-state error between the actual generator shaft speed and reference generator shaft speed, and to obtain a fast dynamic response. The actual generator shaft speed can be estimated from the generator output voltage based on the PLL [65] as discussed in previous Section.

### 2.2.4 Automatic Voltage Regulator (AVR)

The excitation system regulates the output voltage of the synchronous generator. It includes an electronic AVR and an exciter circuit. The VAR adjusts the synchronous generator terminal voltage by regulating the excitation level of the synchronous generator. It is modelled based on IEEE Std. 412.5. It includes a thyristor-based rectifier controlled by a closed-loop PI controller as shown in Figure 2.19 (b). Regarding the dynamics of the rectifier, it can be represented as a first-order transfer function with time-constant  $\tau_{rec}$ , and a linear gain  $g_{rec}$ .

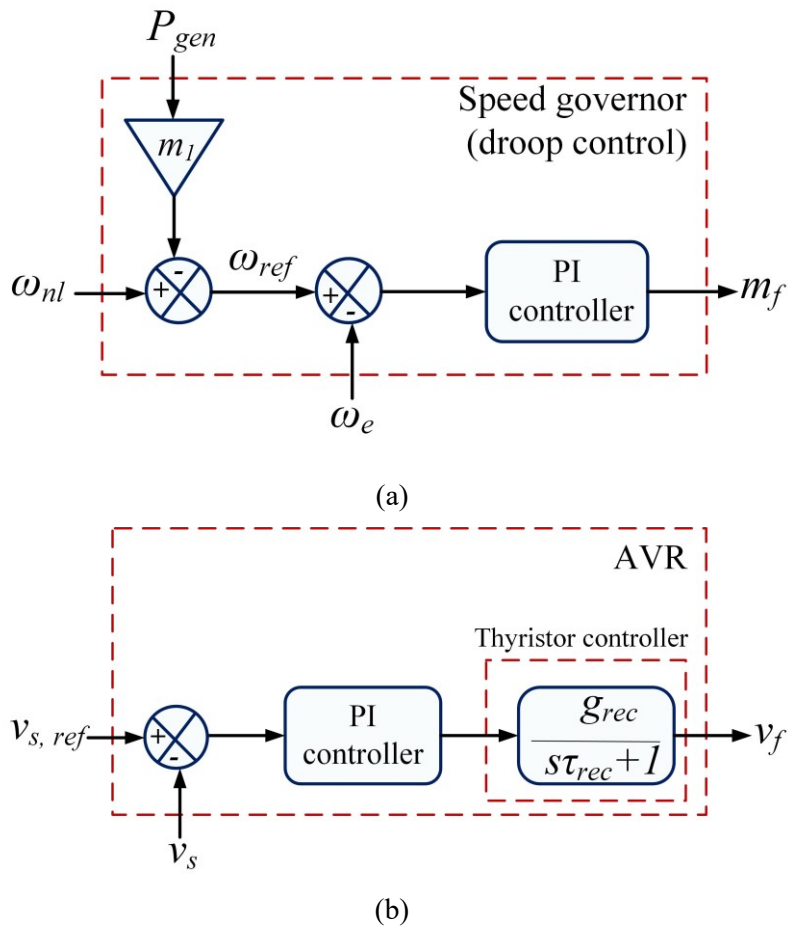


Figure 2.19 The model of (a) speed governor, (b) AVR.

Figure 2.20 shows simulation results of an isochronous controlled diesel genset which is connected to a three-phase load. The initial value of the load is 1.25 kW and then changes to 2 kW at 20s. The no-load generator shaft speed is selected at 188.49 rad/s (60 Hz) while the droop gain value is zero. Other parameters of the diesel genset are given in Appendix A. Figure 2.20 (a) shows that the generator frequency (or speed) is returned to its reference value (60 Hz) after the load change, regardless of the output power of the diesel genset. The output power, current and voltage of the diesel genset are shown in Figure 2.20 (b), (c), and (d), respectively.

Figure 2.21 shows simulation results for the diesel genset and load change similar to the previous test, while the diesel genset operates based on the droop control mode. In the droop mode, the no-load generator shaft speed and the droop gain value are selected 194.77 rad/s (62 Hz) and 0.0005 rad/sW, respectively. Figure 2.21 (a) shows the generator frequency performance before and after the load change. It can be seen that the steady-state value of the generator frequency changes with the diesel genset output power based on equation (2.45). Figure 2.21 (b), (c), and (d) show the output power, output current and voltage of the diesel genset, respectively.

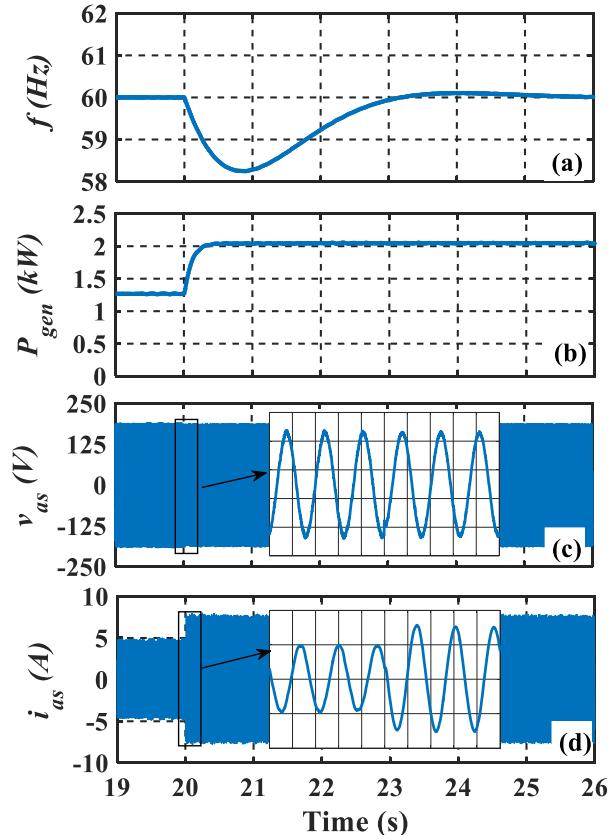


Figure 2.20 Isochronous mode operation of diesel genset; (a) frequency, (b) output active power, (c) output phase voltage, and (d) output current.

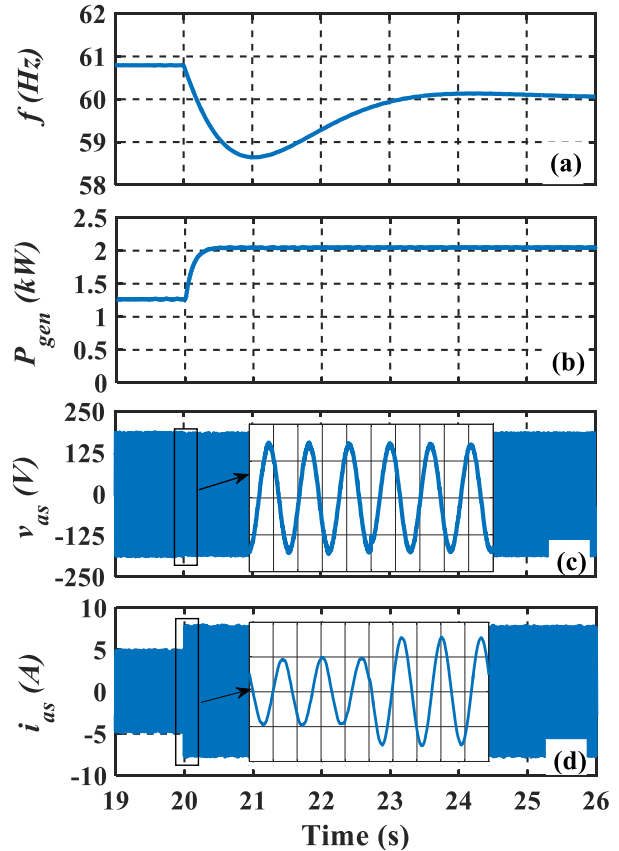


Figure 2.21 Droop mode operation of diesel genset; (a) frequency, (b) output active power, (c) output phase voltage, and (d) output current.

### 2.3 Summary

This chapter presented the theoretical background and modeling of the storage-less D-HK microgrid. The power tracking control challenges in the HKECS have been discussed. The operation of the HKT in both low and high-speed regions have been compared. The HKECS can dispatch its output power in the low-speed region from the maximum available power to zero. Moreover, the shutdown procedure is achieved in this region. However, an instability problem appears due to the inherent characteristics of the HKT. The HKT can be deloaded in the high-speed region where the power reserve is obtained from the stored kinetic energy in rotational parts of the HKECS. However, the deloading percentage and the control strategy to control the rotor speed so that sufficient stored power can be injected into the grid, are some of the challenges.

Some advantages and disadvantages of three conventional power converter topologies have been highlighted. A 6-switch converter plus 2L-VSI (back-to-back converter) and diode rectifier plus DC-DC converter plus 2L-VSL allow continuous power regulation from zero to the highest turbine speed. The diode rectifier plus DC-DC converter is simpler and cheaper than the 6-switch converter. However, the problems of harmonic distortion and power losses in the generator arise. The diode rectifier plus 2L-VSI can operate at both maximum power tracking and over-speed operation. Moreover, in order to achieve active power curtailment and regulate DC-link voltage, a controllable DC load can be connected at the DC-link of this topology. However, the sizing of the controllable DC load should be considered. Some simulations have shown and discussed in order to investigate characteristics and some features of the storage-less D-HK microgrid.

## Chapter 3. Supervisory Power Control for a Dispatchable Fixed-Pitch PMSG-Based Hydrokinetic Energy Conversion System

*This chapter presents a new dispatchable power controller for a fixed-pitch cross-flow hydrokinetic energy conversion system (HKECS) operating in the low rotational speed (stall) region. It delivers a given power requested by an operator ( $P_{dc, sp}$ ) provided that the water speed is high enough. If not, it delivers as much as possible, operating with a maximum power point tracking (MPPT) algorithm while meeting the basic operating limits (i.e. generator voltage and rotor speed, rated power and maximum water speed), shutting down automatically if necessary. All this with smooth transitions between modes of operation and without sensing neither water speed nor generator speed. The HKECS employs a permanent magnet synchronous generator (PMSG), a diode rectifier and a boost DC-DC converter connected to a generic DC bus. The control strategy is realized with a single variable, the duty cycle of the boost DC-DC converter. It employs an inner diode rectifier output voltage loop and an outer HKECS power control loop. The control system is designed and developed based on a linearized model of the system. The performance of the proposed dispatchable power controller and supervisory control algorithm is verified experimentally with an electromechanical-based hydrokinetic turbine (HKT) emulator.*

### 3.1 Introduction

A hydrokinetic energy conversion system (HKECS) extracts kinetic energy from the running water in a river or from tidal currents in the sea. It produces electricity without dams and the associated infrastructure required for the conventional hydropower generation [8]. Most hydrokinetic turbines (HKTs), such as the cross-flow, operate with a fixed pitch angle. In order to control the power absorbed from the water flow, the HKT's rotational speed has to be controlled which can be done using a variable-speed generator control [66], [67]. The mechanical power absorbed by the HKT is then converted into electrical power what is usually done with a permanent magnet synchronous generator (PMSG) and a power electronics interface. A three-phase diode rectifier followed by a boost DC-DC converter is very common as the “generator side converter” of small (1 kW – 100 kW) commercial HKECSs [68]. A three-

phase 6-switch voltage source converter (VSC) has also been considered for HKECSs [69]. It can draw a less distorted current from the PMSG and offers more control flexibility at the expense of higher costs.

Usually, below rated water speed ( $v_{T,N}$ ), the HKECS operates with a maximum power point tracking (MPPT) algorithm. From  $v_{T,N}$  to the cut-off water speed ( $v_{T,cut-off}$ ), the output power should be limited to the rated value of the HKECS, while can be described as a constant power mode (CPM), with the HKT operating in the low rotational speed (stall) region. For the connection of the HKECS to an AC or DC grid, it is important that it can respond to a grid dispatcher's request to regulate its power production to a given reference value [69]. This can be seen as a power regulation mode (PRM) in which the output power should be controlled anywhere between zero and the maximum power, as defined by the power vs. water speed curve envelope. In addition, the system should shut down if the water speed exceeds  $v_{T,cut-off}$ . This can be done with mechanical brakes, but using the power electronics interface would be highly desirable.

Operation of HKECSs and WECSs with MPPT and CPM, above rated water/wind speed, have been discussed in [15], [70], [71], [72], [73], [74]. In the majority of the cases, a diode rectifier followed by a boost DC-DC converter has been used. A robust gain scheduled control scheme for an HKT operating in MPPT and CPM with a single rotor speed control loop was proposed in [15]. In [70], operation in CPM in the stall region was accomplished with a cascaded outer power and inner speed/voltage control scheme. Besides, a power control strategy to ensure safe switching between MPPT and CPM at the rated water speed was presented. In [71], a soft-stall method employing cascaded outer rotor speed (diode rectifier voltage) and inner current controllers for operating the turbine in CPM during high wind conditions is discussed. In [72], operation in CPM in the stall region is carried out based on a single speed/voltage control loop and a boost DC-DC converter. In [73] using a buck DC-DC converter, a robust overall power control strategy for operation in MPPT, speed limiting mode (SLM) and CPM is reported. This is achieved with an adaptive controller used as a speed regulator in an outer power and inner speed/voltage control loop. In [74], also with a buck DC-DC converter, the smooth transition between MPPT and CPM is obtained by a cascaded outer power, middle voltage and inner current control scheme. However, in all these methods, a control scheme that allows HKECSs

with a diode rectifier and DC-DC converter to operate anywhere within the envelope of the power vs. water speed has not been reported. Such a control scheme was achieved in [27] with the more sophisticated and costly three-phase 6-switch VSC using a cascaded inner current and outer power control loop. Nonetheless, it did not discuss a supervisory control system that yields an operator set reference power, provided that the water speed is high enough, or the maximum possible otherwise. It should also automatically adjust to water speed variations, delivering when possible the requested power, with seamless transitions, while respecting generator voltage and rotor speed as well as water speed limits.

In this chapter, such a supervisory control system is developed for an HKECS with a PMSG-based fixed-pitch HKT. A diode rectifier followed by a boost DC-DC converter is selected as a generator-side converter. It is realized with a cascaded inner speed/voltage and outer power control loop.

### 3.2 Description of HKT Operating Conditions

Figure 3.1 shows the conventional envelope of the output power of a HKT ( $P_{HKT}$ ) as a function of the water speed ( $v_T$ ). From cut-in ( $v_{T,cut\_in}$ ) to  $v_{T,gN}$ , the water speed at which the generator rotor speed reaches its rated value, the HKT operates in the MPPT mode. From  $v_{T,gN}$  to rated water speed ( $v_{T,N}$ ), the generator speed should be limited to its rated value, what can be described as a speed limiting mode (SLM). The SLM can be ignored from the envelope with increasing the rated value of generator rotor speed in some application when the operation of the HKT in the high speed region is desirable. From  $v_{T,N}$  to the cut-off water speed ( $v_{T,cut-off}$ ), the output power is limited to the rated value of the HKT, while can be described as a constant power mode (CPM). The system should shutdown if the water speed exceeds  $v_{T,cut-off}$ . Unlike this conventional approach, where a value of  $v_T$  implies a single value of  $P_{HKT}$ , the HKT should be able to regulate its output power to a given reference value anywhere between zero and the maximum value of the  $P_{HKT}$  vs.  $v_T$  envelope. This can be achieved with a power control scheme at the stall region called power regulation mode (PRM). In order to achieve safe and seamless transition between operating modes, a supervisory power control system is required. Such a supervisory control system is discussed in details in Section 3.4.

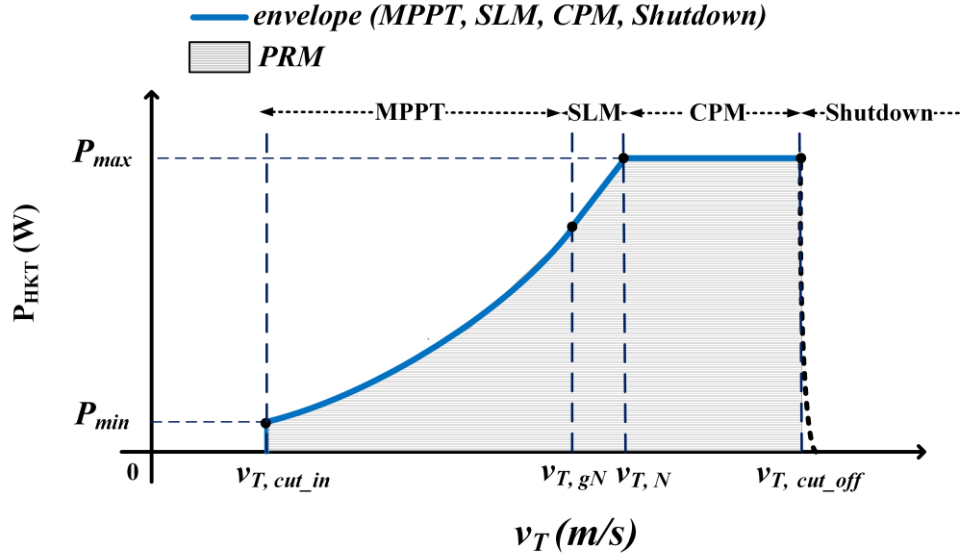


Figure 3.1 HKT output power ( $P_{HKT}$ ) vs. water speed curve ( $v_T$ ).

Figure 3.2 shows the schematic diagram of the HKECS considered in this chapter. It consists of a fixed-pitch HKT including a gear box, a PMSG connected to a diode rectifier, a boost DC-DC converter and a generic DC bus. The latter represents either an autonomous DC microgrid, with loads and energy storage system (ESS), or the DC side of an inverter for interfacing the HKT to an AC grid. It is assumed that the DC bus is regulated by the DC microgrid or grid-tied inverter. The boost DC-DC converter is used to step up the voltage level to a suitable value for the generic DC bus but mostly to control the output power of the HKECS. The control unit consists of a cascaded outer power and inner output diode rectifier voltage (rotor speed) control loop and a supervisory control system as discussed in details next Section. The input signal provided by an operator is a reference output power ( $P_{dc, sp}$ ) that can be used for shut-down if set to zero. The required feedback signals are the output voltage ( $v_{dc}$ ) and current ( $i_{dc}$ ) of the diode rectifier. No measurements of water nor generator rotor speeds are required. The main parameters of the HKECS considered in this chapter are shown in the Appendix A.

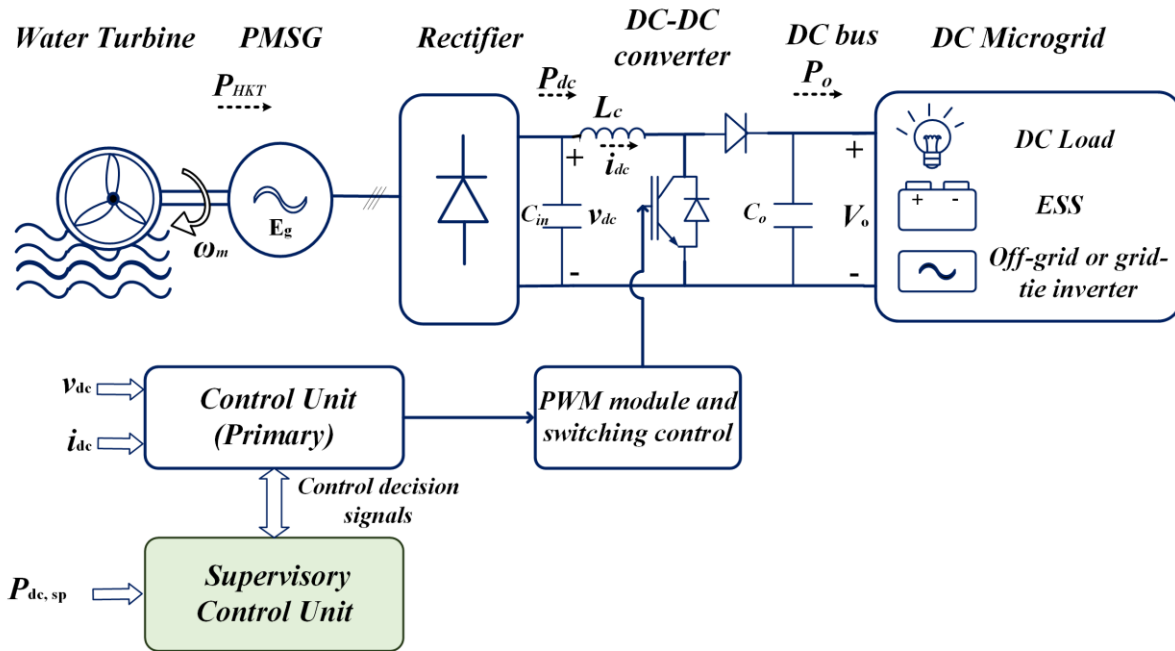


Figure 3.2 Schematic diagram of the HKECS.

The output power and torque of a fixed-pitch cross-flow type HKT were introduced in the Section 2.1.1. According to equation (2.1), the output power of the HKT, for a given water speed, can be reduced by decreasing the power coefficient  $C_p$ . This can be done by operating at either below or above the tip speed ratio for maximum  $C_p$ . ( $\lambda_{opt}$ ). Regulating the HKT's output power below the  $\lambda_{opt}$  region is desirable since it can prevent high rotor speeds [71]. However, it requires a more sophisticated control strategy since this region is open loop unstable [15]. This subject will be discussed in next Section.

### 3.2.1 MPPT Operation

As shown in Figure 2.2, the HKT operates at maximum power tracking mode (MPPT) for various water speeds when it operates at the tip speed ratio for maximum  $C_p$  ( $\lambda_{opt}$ ). There are several methods to control a HKECS and a WECS to operate in the MPPT mode [75], [76]. Many require measurements of  $v_T$  and/or  $\omega_m$ , what makes the system more costly. An interesting and simple MPPT algorithm which does not require either one was proposed in [35].

From equation (2.1), the maximum power from the HKT can be written as follow:

$$P_{HKT\_max} = 0.5\rho AC_{p, max}v_t^3 \quad (3.1)$$

Substitute equation (2.3) into equation (3.1),  $P_{HKT\_max}$  can be obtained as

$$P_{HKT\_max} = K_{opt}\omega_m^3 \quad (3.2)$$

where  $K_{opt}$  is a constant value depending on the HKT parameters and is given by

$$K_{opt} = \frac{0.5\rho AR^3 C_{p, max}}{\lambda_{opt}^3} \quad (3.3)$$

Taking into account that  $V_{dc}$  is proportional to  $\omega_m$ , the reference voltage corresponding to  $P_{HKT\_max}$  for any value of  $v_T$  is obtained by substituting equation (2.34) into equation (3.2), resulting in

$$V_{dc, MPPT} = K_V' \sqrt[3]{\frac{P_{dc}}{\mu K_{opt}}} \quad (3.4)$$

where  $\mu$  is the efficiency of the system and  $K_V'$  is equal to  $g_r K_V$ .  $K_{opt}$  and  $\mu$  can be obtained through off-line tests or simulations on the HKT, generator, and diode rectifier [35]. Therefore, in order to operate the HKT in the MPPT mode,  $P_{dc}$  can be measured and used to calculate a reference value for  $V_{dc}$  according to equation (3.4). The control loop for  $V_{dc}$  is analyzed and designed in next Section.

### 3.3 Design of the Controllers for Power and Speed/Voltage Regulation in the Stall Region

In order to design a control system for obtaining a desired performance in the low rotational speed (stall) region, it is necessary to have a model that represents the behaviour of the HKECS at its various operating points. Due to the nonlinear nature of the HKECS, a linearized model of the system is needed if one wishes to employ a linear proportional-integral-derivative (PID) type controller [38], [77]. Since the electrical dynamics related to the stator of the PMSG, and power

electronics interface is much faster than the electromechanical dynamics, the former can be neglected.

Using a single-mass lumped model for the drivetrain of the HKECS and neglecting the friction losses the torque equation of the HKT and PMSG is given by

$$T_{HKT} - T_{ePMSG}' = J \frac{d\omega_m}{dt} \quad (3.5)$$

where  $J$  and  $T_{ePMSG}'$  are the total system inertia and the generator electromechanical torque reflected to the turbine side of the gear box.

Using Taylor series expansion on equations of (2.1), (2.28), and (3.5) around one equilibrium point (E.P.), defined by  $(I_{dc0}, \omega_{m0}, V_{T0})$  and ignoring the high-order terms, the linearized small-signal dynamics of the system is given as

$$\Delta T_{HKT} - \Delta T_{ePMSG}' = J \frac{d\Delta\omega_m}{dt} \quad (3.6)$$

where

$$\Delta T_{HKT} = \left. \frac{\partial T_{HKT}}{\partial \omega_m} \right|_{\omega_{m0}, V_{T0}} \Delta\omega_m + \left. \frac{\partial T_{HKT}}{\partial v_T} \right|_{\omega_{m0}, V_{T0}} \Delta v_T \quad (3.7)$$

where “ $\Delta$ ” is the variation of the variable with respect to the E.P. “ $\frac{\partial}{\partial \omega_m}$ ” and “ $\frac{\partial}{\partial v_T}$ ” are the derivative as a function of  $\omega_m$ , and  $v_T$ , respectively, and can be calculated as

$$\left. \frac{\partial T_{HKT}}{\partial \omega_m} \right|_{\omega_{m0}, V_{T0}} = \alpha = 0.5\rho AR^2 V_{T0} \left( \frac{1}{\lambda_0} \left. \frac{\partial C_p}{\partial \lambda} \right|_{\lambda_0} - \frac{C_{p0}}{\lambda_0^2} \right) \quad (3.8)$$

$$\left. \frac{\partial T_{HKT}}{\partial v_T} \right|_{\omega_{m0}, V_{T0}} = \beta = \frac{0.5\rho AR V_{T0}}{\lambda_0} \left( -\lambda_0 \left. \frac{\partial C_p}{\partial \lambda} \right|_{\lambda_0} + 3C_{p0} \right) \quad (3.9)$$

, and

$$\Delta T_{ePMSG}' = \frac{\partial T_{ePMSG}'}{\partial I_{dc}} \Delta I_{dc} = K'_T \Delta I_{dc}, \quad K'_T = \frac{2\sqrt{3}}{\pi g_r} K_T \quad (3.10)$$

where  $\frac{\partial}{\partial I_{dc}}$  is the derivative as a function of  $I_{dc}$ ,

Substituting equation (3.7) and (3.10) into equation (3.6), and taking Laplace “dynamic of the system, the linearized small-signal model of the HKECS showing how the rotor speed varies with the average value of the output current of the diode rectifier ( $I_{dc}$ ) and water speed ( $v_T$ ) can be expressed as

$$\omega_m(s) = \frac{-K'_T}{Js - \alpha} I_{dc}(s) + \frac{\beta}{Js - \alpha} v_T(s) \quad (3.11)$$

where  $\alpha$  and  $\beta$  are parameters that change according to the steady-state operating points.

As pointed out in Section 3.1, HKECSs are usually controlled with a cascaded inner voltage/speed and an outer power loop. Mathematical models for these loops as well as the design of suitable (linear) PID-type controllers are discussed in the following Sub-Sections.

### 3.3.1 The Inner Speed/Voltage Loop

As mentioned before, besides stepping up the output voltage of the diode rectifier, the boost DC-DC converter provides a single parameter control means for the HKECS. According to equation (2.35), the relationship between the average output voltage ( $V_{dc}$ ) and current ( $I_{dc}$ ) of the diode rectifier and the duty cycle ( $d$ ) of the boost DC-DC converter in the Laplace domain is given as

$$V_{dc}(s) = L_c s I_{dc}(s) + d'(s) V_o(s) \quad (3.12)$$

where  $d'(s) = 1 - d(s)$  and  $V_o(s)$  is the DC-link voltage. Since the DC-link is assumed to be regulated to a certain value,  $V_o(s)$  can be represented by constant value,  $K_m$ . Substituting equation (2.34), (2.28), (2.32) and (3.12) into equation (3.11) and considering  $V_o(s) = K_m$ , one can obtain an equation that represents how the average value of the output voltage of the diode

rectifier, which is proportional to the rotor speed, varies with the control variable of the boost converter and the (uncontrollable) water speed.

$$V_{dc}(s) = \frac{K'_T K'_V K_m}{L_c J s^2 - L_c \alpha s + K'_T k K'_V} d'(s) + \frac{L_c \beta}{L_c J s^2 - L_c \alpha s + K'_T K'_V} v_T(s) \quad (3.13)$$

where  $K'_T = \frac{2\sqrt{3}}{\pi g_r} K_T$ . In order to design a controller for the voltage loop, one needs a transfer function relating the duty cycle of the boost DC-DC converter to  $V_{dc}$ , which can be obtained from equation (3.13):

$$\frac{V_{dc}(s)}{d'(s)} = \frac{K'_T K'_V K_m}{L_c J s^2 - L_c \alpha s + K'_T K'_V} \quad (3.14)$$

From equation (3.14), the system poles can be calculate as

$$s_{1,2} = \frac{L_c \alpha \pm \sqrt{(L_c \alpha)^2 - 4 L_c J K'_T K'_V}}{2 J L_c} \quad (3.15)$$

Figure 3.3 shows the real part of the plant poles for the cut-in (1.2 m/s) and cut-out (3 m/s) water speeds considering the typical range of  $\lambda$ . The system poles have a positive value, being located in the right-half-plane (RHP) of the complex plane, for  $0.3 < \lambda < 1.72$ . This range corresponds to the region where the slope of the  $C_q$  vs.  $\lambda$  curve ( $\frac{\partial C_q}{\partial \lambda}$ ) is positive.  $\lambda = 1.72$  corresponds to  $C_{q,max}$  as shown in Figure 2.2 (a). Moreover, the most critical condition, at which the poles of the plant present the largest positive real part, occur for  $v_T = 3$  m/s and  $\lambda = 0.8$ . In the MPPT condition where  $\lambda = \lambda_{opt} = 2.1$ , the real part of the plant poles is negative.

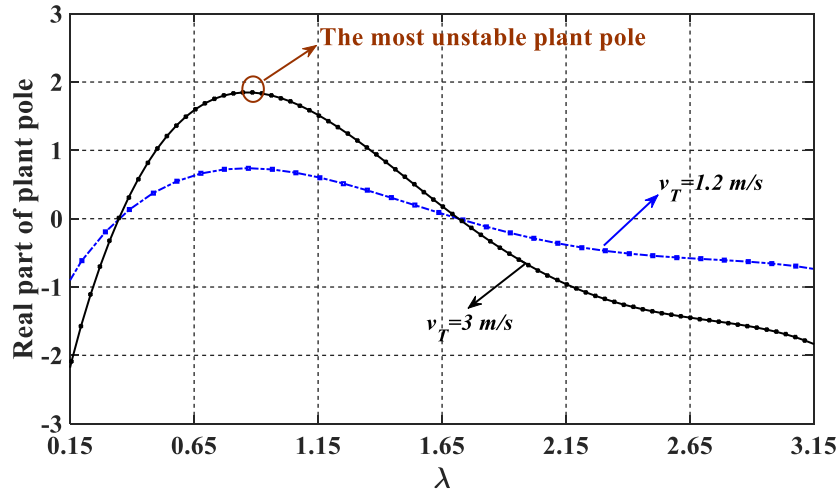


Figure 3.3. The real part of plant poles vs. tip speed ratio at water speed 1.2 m/s and 3 m/s.

To stabilize the system dynamics in the stall region, the plant is compensated using a standard PID controller and a unity feedback closed-loop voltage control system. The voltage controller transfer function,  $C_V(s)$ , is defined as

$$C_V(s) = K_p + \frac{K_i}{s} + K_d s \quad (3.16)$$

where  $K_p$ ,  $K_i$  and  $K_d$  are the proportional, integral and derivative gains, respectively. The voltage controller gains were selected using MATLAB control system toolbox in order to obtain a zero steady state error to a step reference signal, with a maximum overshoot of 15%, and a settling time of less than 0.2 s [78]. The controller is designed for the most critical operating point,  $v_T = 3 \text{ m/s}$  and  $\lambda = 0.8$ . The values of the gains of the voltage controller are given in the Appendix A. Figure 3.4 shows the root locus of the system with the designed controller. The closed-loop poles have positive real parts, meaning that a stable system is ensured. To observe the behavior of the designed controller in the time-domain, the step responses for different values of  $\lambda$  and for  $v_T = 3 \text{ m/s}$  and  $v_T = 1.2 \text{ m/s}$  are shown in Figure 3.5. It is clear that the system presents virtually the same response irrespective of the operating point on the  $C_p$  and  $C_q$  vs.  $\lambda$  curves.

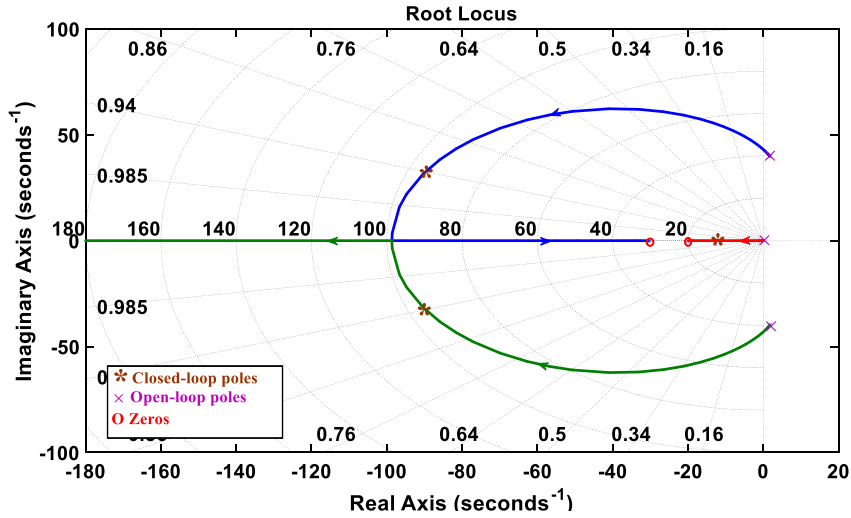


Figure 3.4 Root locus of the system with the designed voltage controller at  $v_T = 3 \text{ m/s}$  and  $\lambda = 0.8$ .

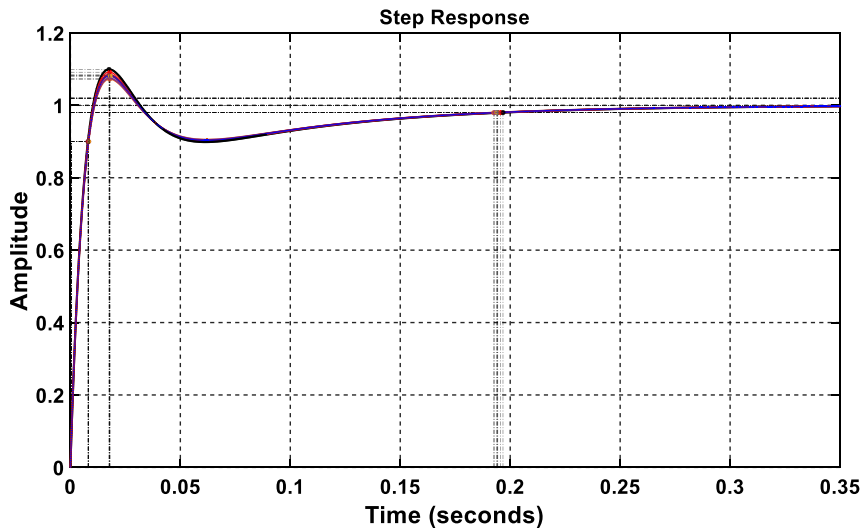


Figure 3.5 Step response of the voltage loop for  $v_T = 1.2 \text{ m/s}$  and  $3 \text{ m/s}$  at  $\lambda = [0.15, 0.8, 2.1, 3]$ .

### 3.3.2 The Outer Power Loop

The output power of the diode rectifier ( $P_{dc}$ ) can be regulated to a desirable reference value in the stall region using an outer power control loop as shown in Figure 3.6. The error between the reference and measured powers passes through a power controller to produce a reference value

for the inner voltage loop. For the design of this controller, one needs a relation that shows how the actual power is affected by the output voltage of the diode rectifier. Since  $P_{dc}$  is the product of  $V_{dc}$  and  $I_{dc}$ , the latter being internal to the voltage loop, obtaining a transfer function analytically is not straightforward.

One method that can be used to obtain an approximate transfer function between  $P_{dc}$  and  $V_{dc}$  is to apply a step variation in the reference voltage and observe the output power [78]. In principle, from the response of the measured power, one can obtain gain and time constants that represent this relation. An experimental test, with the set-up described in Section 2.6, was performed to determine the dynamic relation between  $P_{dc}$  and  $V_{dc}$ . The response of  $P_{dc}$ , with the power loop open, to a variation in  $V_{dc}^*$  from 80 V to 85 V, with  $v_T = 3$  m/s is shown in Figure 3.7. One can see that the output power first decreases, then increases before reaching a steady-state value higher than before. This indicates a non-minimum-phase system where the power loop has an RHP zero. The transfer function corresponding to the relation between  $P_{dc}$  and  $V_{dc}$  can be approximated as [78]

$$\frac{P_{dc}(s)}{V_{dc}(s)} = \frac{M(1 - T_z s)}{(1 + T_p s)} \quad (3.17)$$

where  $M$ ,  $T_z$ , and  $T_p$  are the gain and time constants corresponding to the zero and pole locations. The transfer function parameters identified from Figure 3.7 using MATLAB transfer function estimation (*tfest*) function are given in the Appendix A. In order to obtain a zero steady-state error to a step input, an integral controller was selected for the power control loop. It is represented by

$$C_p(s) = \frac{K_{ip}}{s} \quad (3.18)$$

where  $K_{ip}$  is the integral gain.

$K_{ip}$  was selected as 0.1, so as to also mitigate the impact of the RHP zero. The dynamic response of the power loop to a step input variation is shown in Figure 3.8 for  $v_T = 1.2$  m/s and  $v_T = 3$  m/s at  $\lambda = 0.8$ . There one sees a relatively slow dynamic response, but this is not critical

since the power reference value does not change frequently. The settling time for  $v_T = 3$  m/s and  $v_T = 1.2$  m/s are around 5 s and 9 s, respectively.

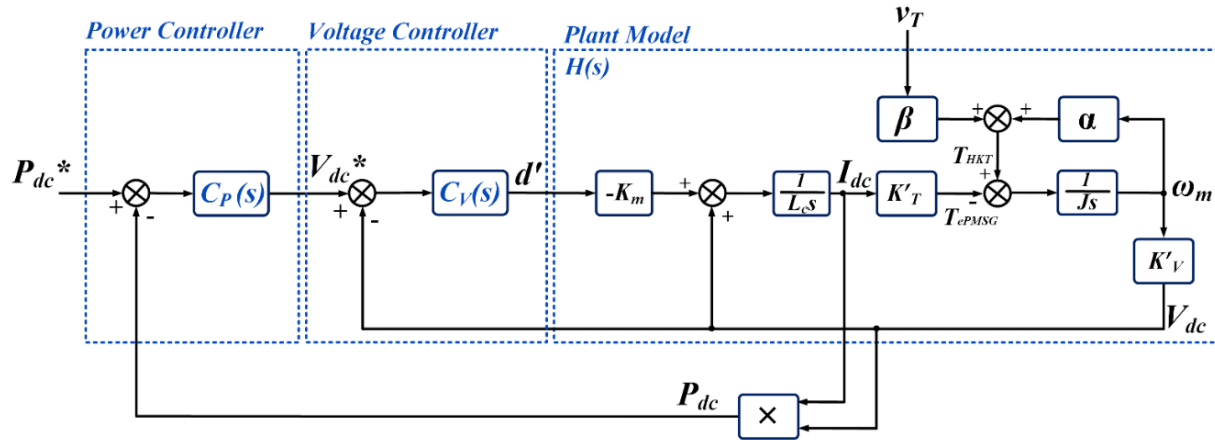


Figure 3.6 A cascaded inner voltage and outer power loop control block diagram of the system for operation in the stall region.

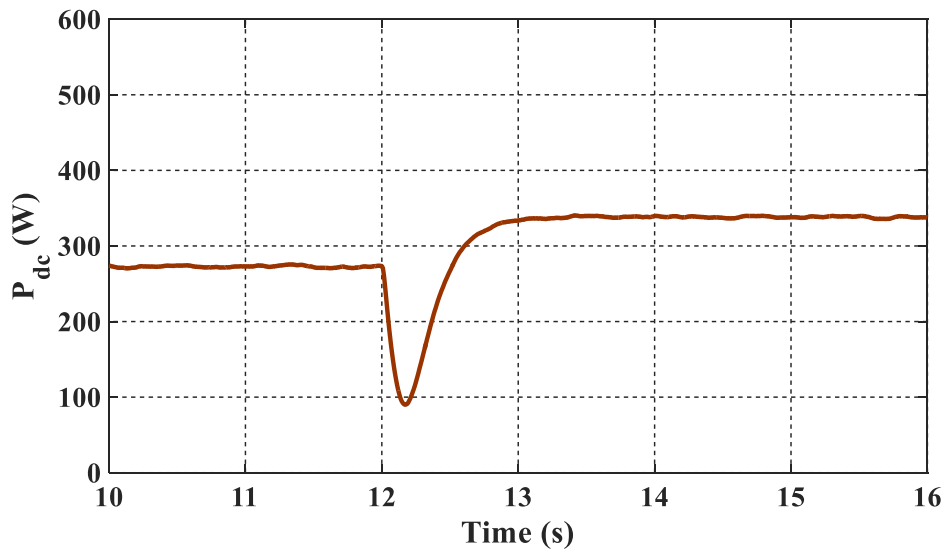


Figure 3.7  $P_{dc}$  open-loop response to a variation in  $V_{dc}^*$  from 80 V to 85 V with  $v_T = 3$  m/s.

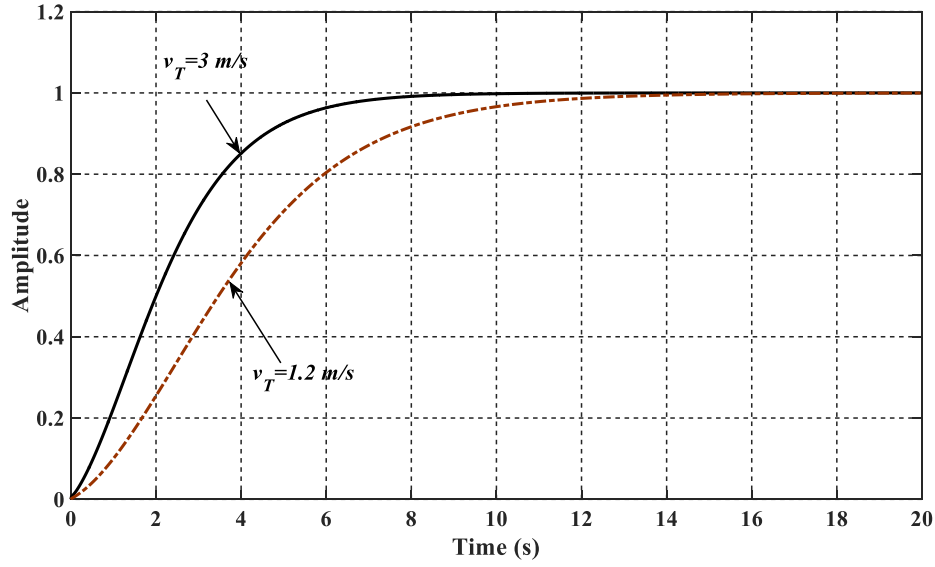


Figure 3.8 Step responses of the power loop for  $v_T = 1.2$  m/s and 3 m/s at  $\lambda = 0.8$ .

### 3.4 Proposed Supervisory Power Control System

In most conventional power sources, an operator requests a given amount of power which is equal to or less than the known rated power. However, for renewable sources such as HKECS, the maximum power they can deliver varies with the fluctuating water speed. Ideally, if the renewable source cannot provide the required power ( $P_{dc,sp}$ ), then it should provide as much as possible, according to the actual water speeds. This would correspond to operation in either MPPT or SLM as described in the Section 3.2. Regarding shutting down, this should be either due to an operator request, by making  $P_{dc,sp} = 0$  W, or automatically as the water speed exceeds  $v_{T,cut\_off}$ . This is what is achieved with the proposed supervisory control system, without measuring the water and the generator speeds.

The operating conditions of the HKECS considered in this Chapter can also be described by means of the power ( $P_{dc}$ ) vs. output voltage of the diode rectifier ( $V_{dc}$ ) curves shown in Figure 3.9. The envelope region concerns the curves connecting points A – B – C and D. The curve linking points A (at  $v_{T,cut\_in}$ ) to B (at  $v_{T,gN}$ ) corresponds to operation in the MPPT mode while that between points B and C (at  $v_{T,N}$ ) is related to SLM, where  $V_{dc}$  remains constant. The

operating points on line C – D (at  $v_{T,cut\_off}$ ) concern the CPM. In this region, as  $v_T$  increases  $V_{dc}$  decreases, reaching a minimum value ( $V_{dc,cut\_off}$ ) that can be used for determining that  $v_T$  has exceeded  $v_{T,cut\_off}$ . In fact, a value of  $V_{dc}$  that corresponds to  $v_{T,cut\_off}$  for any value of  $P_{dc} \leq P_{dc,N}$  can be obtained from the curve D – E and used for shutting down the system due to excessive water speed, even without sensing  $v_T$ . This curve is transcribed into a  $P_{dc}$  vs.  $V_{dc}$ , cut-off lookup table used in the proposed supervisory power control system.

The overall block diagram of the proposed supervisory power control system for the HKECS is shown in Figure 3.10. The reference signal for the inner voltage loop ( $V_{dc}^*$ ) comes from the lowest of the output of the MPPT/SLM block ( $V_{dc,12}$ ) or the output of the integral controller of the outer power loop ( $V_{dc,I}$ ), with  $P_{dc}^* = P_{dc,sp} \leq P_{dc,N}$ . It is evident that the transitions between MPPT/SLM and CPM/PRM will be smooth due to the Min function. Let's assume initially that the power requested by the operator ( $P_{dc,sp}$ ) is less than the maximum available power ( $P_{dc,MPPT}$ ) for a water speed of, say,  $v_T = 2.8$  m/s. As can be seen in Figure 3.10, the value of  $V_{dc}$  at the intersection of the horizontal line  $P_{dc,sp}$  with the  $v_T = 2.8$  m/s power curve, is lower than the value of  $V_{dc}$  obtained at the intersection of  $P_{dc,sp}$  with the MPPT/SLM (A – B – C) curve. Since the former corresponds to the value of  $V_{dc,I}$  and the latter to  $V_{dc,12}$ , in steady-state, the system should operate in PRM with  $V_{dc}^* = V_{dc,I}$ . If the value of  $v_T$  decreases, the value of  $V_{dc,I}$  should increase, equalling that of  $V_{dc,12}$  at  $v_T = 2.7$  m/s. For  $v_T < 2.7$  m/s, the system would not be able to deliver the requested power despite operating in MPPT with  $V_{dc}^* = V_{dc,12}$ . In such a case,  $P_{dc} = P_{dc,MPPT} < P_{dc,sp}$  and the HKECS supplies as much power as possible but less than the amount required by the operator.

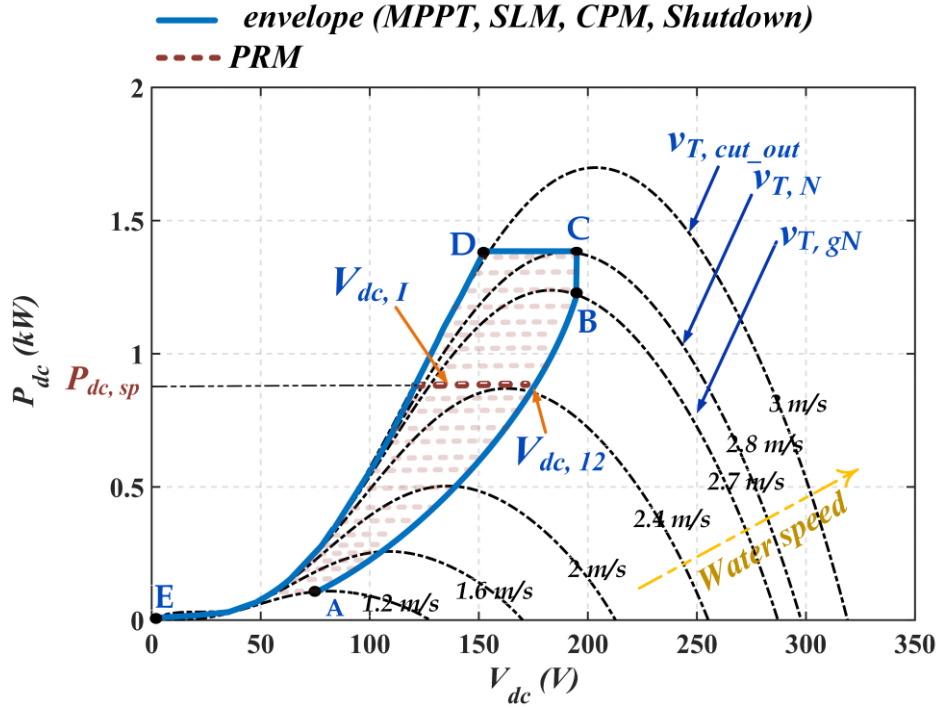


Figure 3.9 Power vs. output voltage of the diode rectifier for various water speeds and operating conditions of the HKECS.

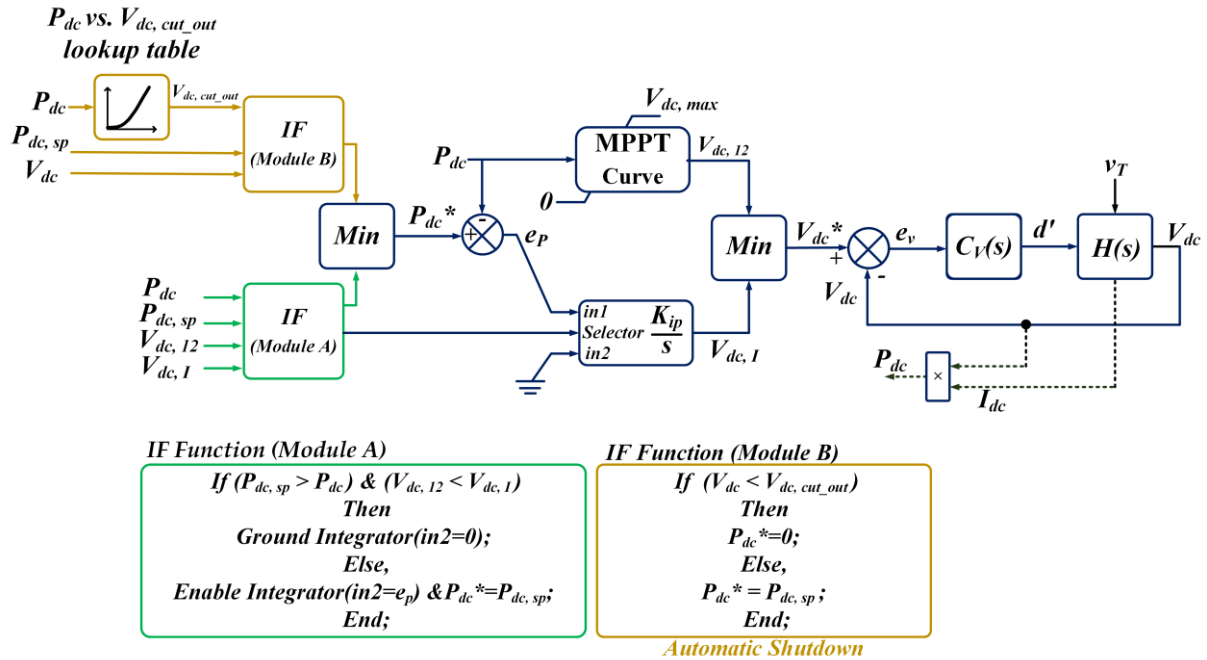


Figure 3.10 Overall control diagram of the proposed supervisory power control system.

However, with  $P_{dc,sp} > P_{dc,MPPT}$ , the power error ( $e_p = P_{dc,sp} - P_{dc}$ ) remains positive and the output of the integrator increases with no possibility of increasing  $P_{dc}$ . This results in the wind-up of the integrator, making the system response very sluggish as the water speed recovers or  $P_{dc,sp}$  decreases. This is the only critical condition that can appear but can be prevented using a simple If – Then – Else function (Module A). It sets the input of the integrator to  $in_2 = 0$  when  $P_{dc,sp} > P_{dc}$  AND  $V_{dc,l} > V_{dc,12}$ . For all other conditions, the integrator should be allowed to process the power error ( $e_p = in_1$ ), while should be minimized.

Regarding the automatic shutdown of the system due to excessive water speeds ( $v_T \geq v_{T,cut\_off}$ ), this can be done by setting  $P_{dc}^* = 0$ , by using an If – Then – Else function (Module B). When the measured value of the output voltage of the diode rectifier ( $V_{dc}$ ) is lower than the critical value obtained from the  $P_{dc}$  vs.  $V_{dc}$ , cut-off lookup table,  $P_{dc}^*$  is set to zero automatically.

### 3.5 Electromechanical-based HKT Emulator

An experimental set-up was assembled in the laboratory to verify the performance of the proposed unified power controller for a fixed-pitch PMSG-based HKECS with a three-phase diode rectifier and a DC-DC boost converter as the power electronics interface. The development and application of HKT and wind turbine (WT) emulators have been discussed in various references [33], [79].

Figure 3.11 (a) shows the schematic diagram of the power circuit and control logic of the HKT emulator. It is based on a DC motor, whose torque is controlled through its armature current. This is achieved with a DC-DC buck converter operating with hysteresis current control (HCC) and fed from the AC grid through a three-phase diode rectifier. The reference signal for the HCC comes from the model (torque vs. shaft speed) of the cross-flow HKT. The inertia of the HKT is also emulated using a single-mass model for the drivetrain. The model of the HKT and drivetrain are implemented in a dSPACE DS1103 rapid control prototyping system. Figure 3.11 (b) shows a picture of the complete system implemented in the laboratory: HKT emulator and unified controller of the HKECS, with power converters, rotating machines and control platform. The experimental results shown in the following Section were obtained with a single DS1103 controlling the HKT emulator and realizing the proposed unified power controller algorithm.

Moreover, simulations results are shown in Appendix B to demonstrate the performance of proposed supervisory power control system while water speed profile containing ripple.

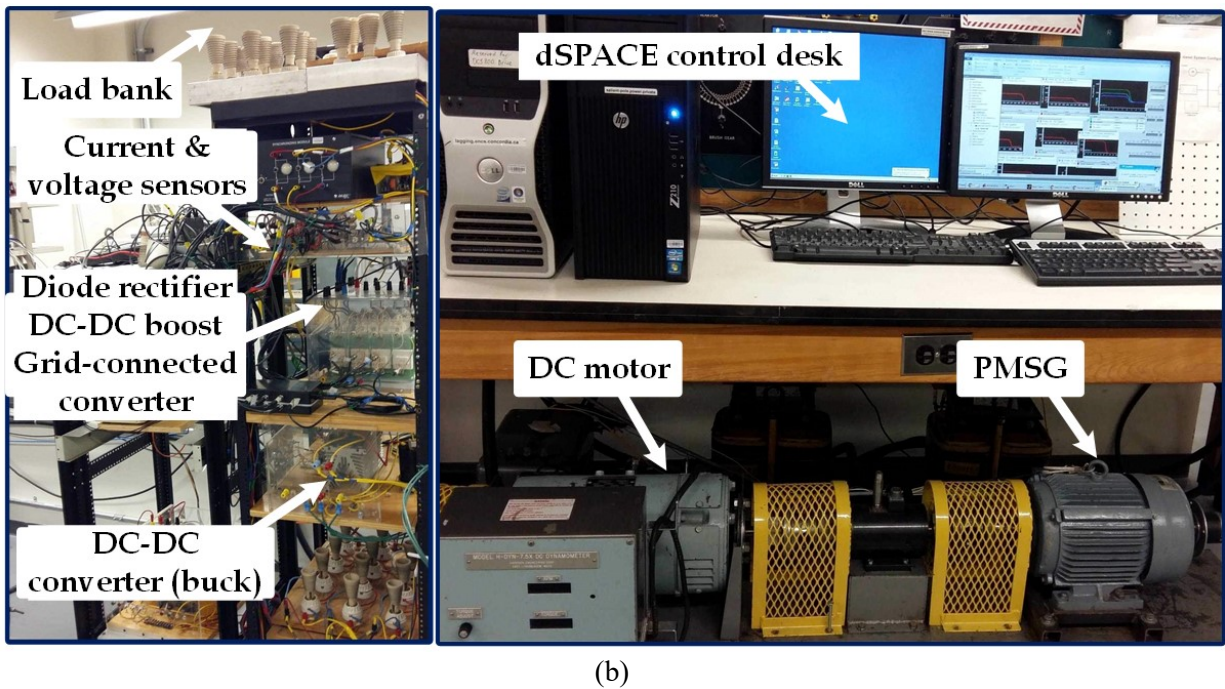
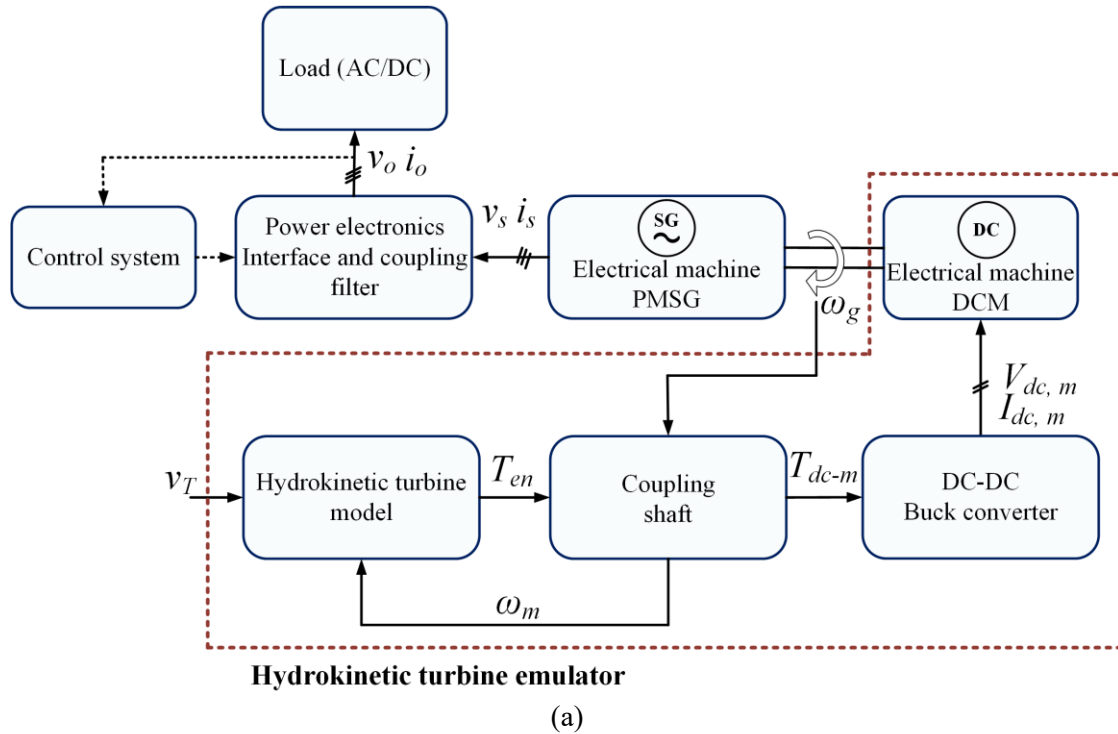


Figure 3.11 (a) Electromechanical-based emulator block diagram, (b) Experimental setup of the HKECS system.

## 3.6 Experimental Results and Discussion

### 3.6.1 Power Control Strategy Procedure

In this Section, selected test results are presented to demonstrate the effectiveness of the proposed control strategy. The rated power of the HKT is 1.45 kW. Considering the efficiency of the system to be 0.87,  $P_{dc,N}$  is calculated as 1.26 kW. The rated generator speed is 105 rad/s, and the corresponding value of  $v_{T,gN}$  and  $V_{dc,max}$  can be calculated as 2.7 m/s and 195 V, respectively. The water speed variations are shown in Figure 3.12 (a). Figure 3.12. (b), (c), (d), and (e) show the resulting output power, the output voltage of the rectifier, the generator rotor speed, and the power coefficient of the HKT, respectively, for various operating conditions.

From  $t = 20$  s to 40 s,  $P_{dc,sp}$  is set to 0.6 kW-while the water speed is constant at 2.9 m/s. Since  $P_{dc,sp}$  is less than the maximum available  $P_{dc}$ , the integrator is enabled and the *Min* function outputs  $V_{dc,I}$ . One can see that  $V_{dc}$  follows  $V_{dc,I}$ . The system operates in the PRM and  $P_{dc}$  is regulated at 0.6 kW as shown in Figure 3.12 (b). In this segment, the average values of the output voltage of the rectifier and the generator rotor speed are found to be 113 V, and 61 rad/s, respectively. The power coefficient is found to be around 0.14, indicating that the HKT operates in the stall region.

From  $t = 40$  s to 140 s,  $P_{dc,sp}$  is changed to 1.26 kW. During this period, three operating conditions are expected according to the water speed variations. It decreases linearly from 2.9 m/s at  $t = 60$  s to 2.5 m/s at  $t = 120$  s. From  $t = 40$  s to 70 s, the water speed is more than  $v_{T,N}$ . Therefore, the control system must limit  $P_{dc}$  to its rated value for operation in CPM. The output power is limited to the rated value as shown in Figure 3.12 (b). Since,  $P_{dc,sp}$  is set at  $P_{dc,N}$ , the integrator is enabled and the Min function outputs  $V_{dc,I}$  as can be observed in Figure 3.12. (c), with decreasing water speed to about  $v_{T,N}$  (2.8 m/s),  $V_{dc}$  and  $\omega_g$  are increased to 182 V and 97 rad/s. From  $t = 70$  s to 90 s, the water speed is between  $v_{T,gN}$  and  $v_{T,N}$ . Therefore, the system operates in SLM, with constant  $V_{dc}$  and constant  $\omega_g$ . This can clearly be observed in Figure 3.12 (c) and (d), respectively.  $V_{dc}$  is restricted to the rated value, (195 V) and  $\omega_g$  is limited to its rated value, 105 rad/s. In this segment,  $P_{dc}$  decreases with decreasing water speed.

From  $t = 90$  s to  $140$  s, water speed is below  $v_{T, gN}$ , meaning that the system can no longer supply  $P_{dc,N}$ . Therefore, the system operates at MPPT. This is achieved with the Min function outputting  $V_{dc,12}$  which is lower than  $V_{dc,I}$  as shown in Figure 3.12 (c).  $V_{dc,I}$  remains constant since the integrator is grounded by the If-then-else function when  $P_{dc,sp} > P_{dc}$  AND  $V_{dc,12} < V_{dc,I}$ . The values of the HKT's power coefficient is found to be around 0.3, the value of  $C_{p,max}$  as presented in Figure 2.2.

At  $t = 140$  s,  $P_{dc,sp}$  is changed to 0.6 kW, remaining in this condition until  $t = 160$  s. The water speed is kept constant at 2.5 m/s. Since  $P_{dc,sp} < P_{dc,MPPT}$ , the power error ( $ep = P_{dc,sp} - P_{dc}$ ) becomes negative and the output of the integrator decreases. Soon,  $V_{dc,I}$  becomes less than  $V_{dc,12}$  and the Min function outputs  $V_{dc,I}$  and the system operates in the PRM. After a brief transient,  $P_{dc}$  is regulated at 0.6 kW as shown in Figure 3.12 (b). The value of the HKT's power coefficient is set at 0.22.  $V_{dc}$  and  $\omega_g$  are found to be 124 V, and 65 rad/s, respectively.

As the experimental results demonstrate, the proposed supervisory power control system works properly while complying with the necessary operation limits. Moreover, the theoretical analyses discussed in previous Sections are found to agree with the experimental results.

### 3.6.2 Shutdown Procedure

As mentioned in Section IV, when  $V_{dc}$  falls below the value obtained from the  $P_{dc}$  vs.  $V_{dc,cut\_out}$  lookup table, the HKECS should automatically shut down. This successful operation is shown in Figure 3.13. The system operates initially with  $P_{dc, sp} = 1$  kW and  $v_T = 2.8$  m/s. At  $t = 20$  s, the water speed starts to increase, reaching the value of 3 m/s ( $v_{T,cut\_out}$ ) at  $t = 40$  s. This condition can be identified without the need for measuring  $v_T$  based on the value of  $V_{dc}$ . One can see from Figure 3.13 (c) that the value of  $V_{dc}$  decreases as  $v_T$  increases, falling below  $V_{dc,cut\_out}$ , computed from the lookup table for  $P_{dc} = 1$  kW, when  $v_T = 3$  m/s. At this moment, the shutdown algorithm sets  $P_{dc,sp}$  to zero. Figure 3.13 (b) shows the output power of the rectifier decreasing following the beginning of the shutdown process. At the same time,  $V_{dc}$  and  $\omega_g$  start to decrease to zero, as shown in Figure 3.13 (c) and (d). Therefore, the proposed algorithm can shut down the HKECS automatically as the water speed exceeds  $v_{T,cut\_out}$ .

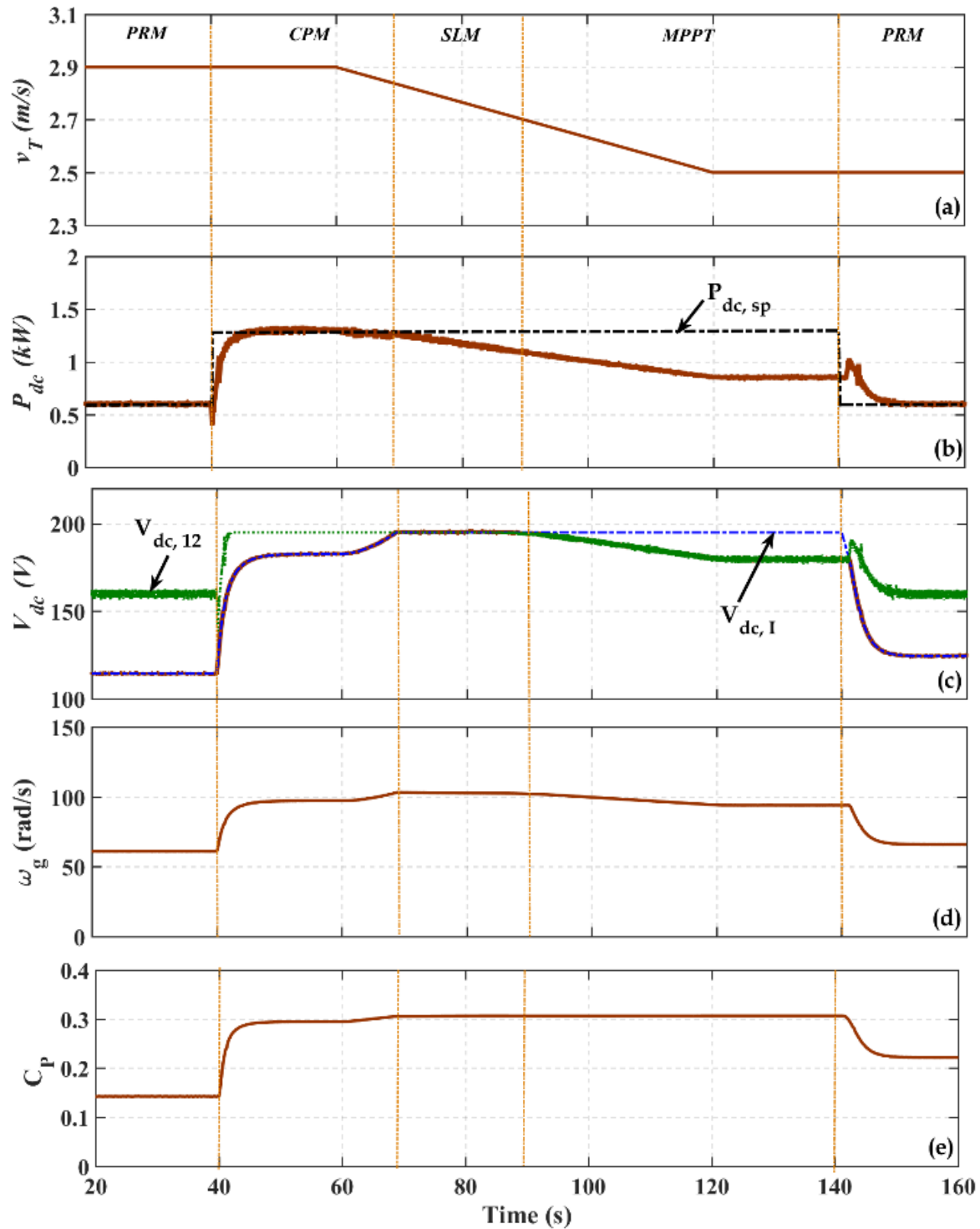


Figure 3.12 HKECS system parameters: (a) water speed variations, (b) output DC power, (c) output DC voltage, (d) PMSG rotor speed, and (e) turbine power coefficient.

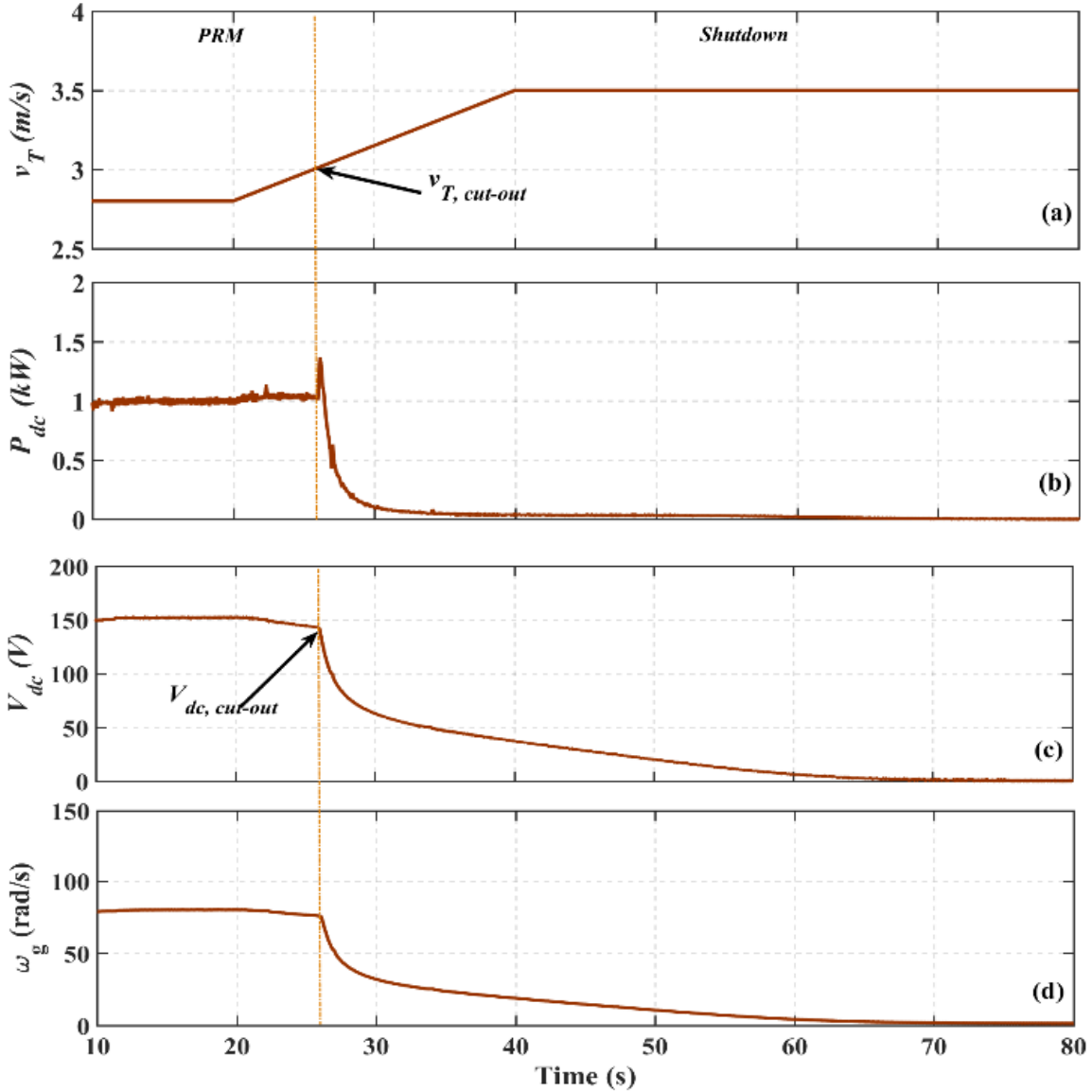


Figure 3.13 HKECS system measurements during shut-down procedure at water speed 3 m/s: (a) water speed variations, (b) output DC power, (c) output DC voltage, (d) PMSG rotor speed.

### 3.6.3 Power vs Water Speed Characteristic

Finally, Figure 3.14 shows the assessment of the DC-link power characteristic with respect to the water speed. This was achieved by increasing the value of  $v_T$  linearly from 1.2 m/s to 4 m/s. From  $v_{T,cut-in}$  (1.2 m/s) to  $v_{T,N}$  (2.8 m/s), the HKECS operates at MPPT and SLM regions. The generated power of the HKT depends on the water speed cubed. Then, it is followed by the CPM region, from  $v_{T,N}$  to  $v_{T,cut-out}$  (3 m/s), where the captured power of the HKT is limited to its

rated value: 1.26 kW. For water speeds above 3 m/s,  $P_{dc}$  becomes zero, and the system shuts down. It looks quite similar to the theoretical power vs. water speed curve shown in Figure 3.9.

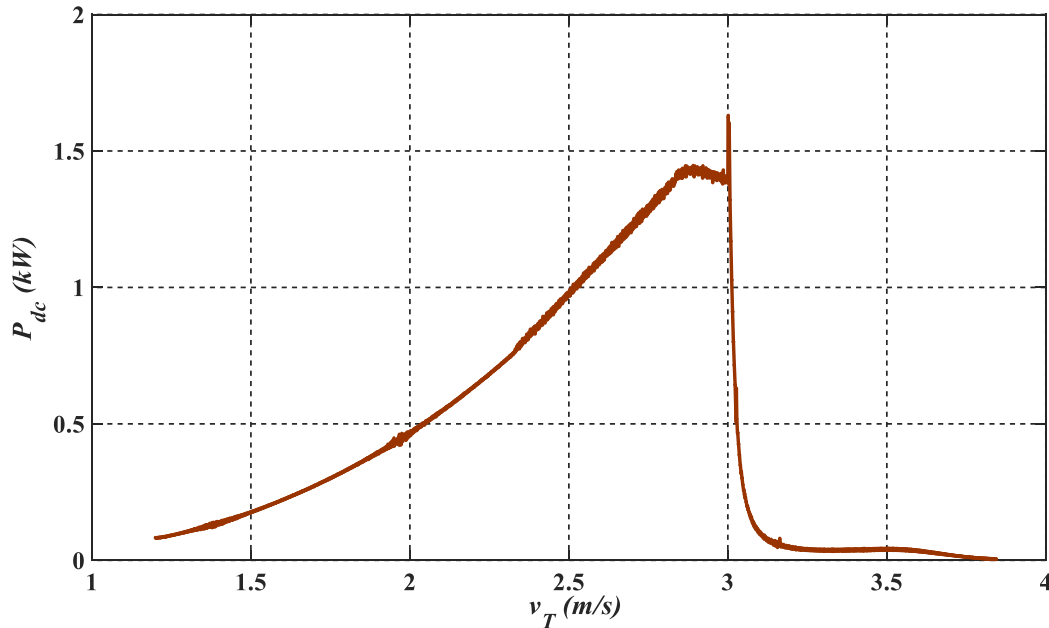


Figure 3.14 DC-link power characteristic with respect to the water speed.

### 3.7 Summary

In this Chapter, a new dispatchable power controller for a fixed-pitch HKT with a PMSG followed by a diode rectifier and a boost DC-DC converter was presented. It allows an operator to set a reference power which is delivered, provided that the water speed is high enough. If not, it delivers as much as possible, operating with MPPT or in a speed limiting mode with an automatic shutdown in case of excessive water speeds. The transition between modes of operation occur smoothly as the water speed and reference power from the operator vary. This is achieved with a novel supervisory controller with simple If – Then – Else and Min functions along with a cascaded outer power and inner diode rectifier voltage loop control system with linear controllers. There is no need for sensing the water speed and the generator speed. The performance of the proposed supervisory controller was demonstrated experimentally with various tests conducted with an electromechanical HKT emulator with the PMSG, diode rectifier and boost DC-DC converter controlled by a DS-1103 dSPACE® system.

## Chapter 4. Power Electronic Converter-Based PMSG Emulator: A Testbed for Renewable Energy Experiments

*This chapter presents a converter-based permanent magnet synchronous generator (PMSG) emulator as a testbed for designing, analyzing, and testing of the generator's power electronic interface and its control system. The permanent magnet synchronous generator model is formulated in a real-time digital simulator. A voltage type ideal transformer model (ITM) combined with a virtual impedance is presented as an interface algorithm between the software and hardware sides. The design procedure and implementation of the virtual impedance in a simulation platform is discussed. A 6-switch voltage source converter (VSC) is used as a power amplifier to mimic the behavior of the PMSG supplying linear and nonlinear loads. A proportional integral plus resonant (PI+res) controller is proposed as a voltage loop controller for tracking a distorted output voltage reference signal. The accuracy of the proposed emulator is investigated for the fundamental and low order voltage harmonics. Technical challenges of the PMSG emulator are considered, and proper solutions are suggested. The performance of the proposed emulator is compared with an actual PMSG.*

### 4.1 Introduction

Permanent magnet synchronous generators (PMSGs) are widely used in wind/hydrokinetic energy conversion systems due to their high efficiency and power density, capability of variable speed operation and elimination of the rotor dc excitation system [80]. To control the power flow and quality, it is commonly connected to the load/grid by means of a power electronic interface (PEI), which usually includes a generator-side and a grid/load-side converter.

A method to develop and test the generator's power electronic interface (PEI) and the emulation of the generator is rapid control prototyping (RCP) [81]. The mathematical model of the generator and its associated prime mover, and the control sub-systems e.g. current and voltage control loops of the converter-based amplifier are programmed in a real-time simulator e.g. dSPACE controller. The simulator provides the reference signals for the power amplifier that replicates the output voltage of the generator. The power amplifier can be interfaced with an actual load to make a real-time simulation configuration with the load current being fed-back into the real-time simulation

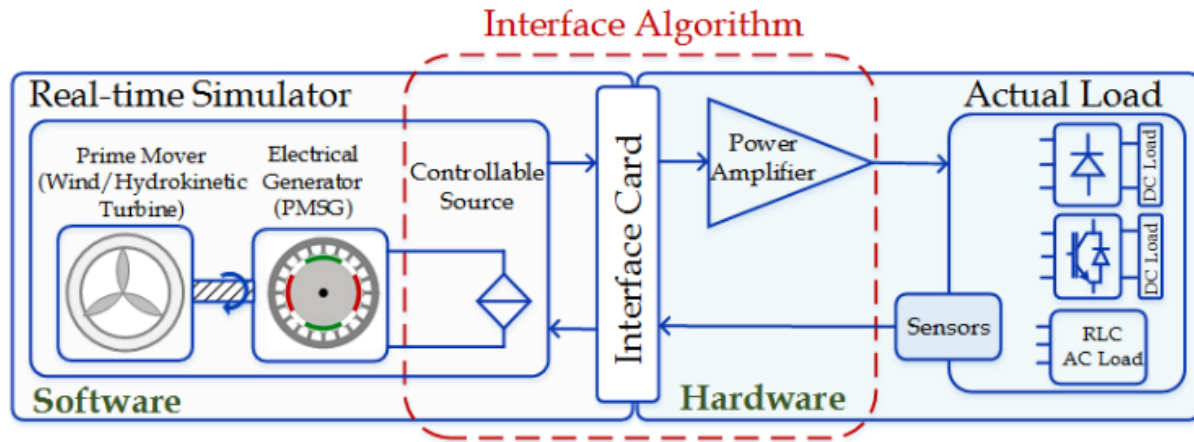


Figure 4.1 Basic block diagram of the emulator of the PMSG-based energy conversion system.

software as shown in Figure 4.1 [82]. Indeed, the emulation of the permanent magnet synchronous generator (PMSG) with RCP method and utilization of the power amplifier permits to develop a power hardware-in-the-loop (PHIL) testbed for testing and validating the generator's PEI controller without the need for an actual PMSG and prime mover.

An interface algorithm is required to link the software side with the hardware side as shown in Figure 4.1. It can be implemented using different methods leading to different degrees of accuracy and system stability. A general comparison of five core interface algorithms consisting of the ideal transformer method (ITM), the transmission line approximation (TLA), the transient first-order approximation (TFA), damped impedance method (DIM), and partial circuit duplication (PCD) is presented in [83]. The ITM is commonly used in many PHIL applications due to its simplicity of implementation and high accuracy [82]. Therefore, the ITM interface algorithm is chosen for this work. Depending on the application, one can use voltage amplification with current feedback, called voltage type ITM, or current amplification with voltage feedback, called current type ITM. Since the PMSG operates as a variable voltage and frequency source, the voltage type ITM is preferred as an interface algorithm. Furthermore, the stability of the voltage type ITM is guaranteed for most generator operating conditions. In fact, the stability of the voltage type ITM is guaranteed if the amplitude ratio of the source impedance to load impedance is less than one, while the stability of current type ITM is guaranteed in the opposite manner [83]. On the other hand, the voltage type ITM on the software side acts as a

controllable current source which is directly connected in series with the PMSG model. The dynamics of electric machines is defined by a set of mechanical and electrical differential equations [84] and the PMSG's terminal voltage depends on the derivative of the generator's current leading to computational problems. Therefore, using the voltage type ITM for the generator emulation presents some issues. A capacitor [85], an inductor [86], and a small parasitic resistor [87] have been included at the terminals of the machine model to avoid computation of derivative terms. However, the procedure of selecting the type and parameters of this impedance and its impact on the machine's dynamics as well as emulator performance has not been discussed.

The type of power amplifier is another important aspect of the development of a PHIL simulation. Linear and converter-based (or switch-mode) power amplifiers are used for PHIL simulations [88]. The linear ones provide high dynamic performance with high bandwidth, up to 20 kHz, and fast response time with few challenges regarding stability. However, they are much more costly and are considered to be viable for PHIL applications ranging from small up to medium power levels. Converter-based amplifiers are less expensive and can more easily be built from the small to the megawatt power levels. However, they provide dynamic characteristics of bandwidths up to 2-10 kHz, which is much lower than linear amplifiers. Their dynamic performance depends on the type of controller, the output filter topology (L, LC, LCL ...) and the switching frequency. Some published papers for a generator/grid emulator have used a voltage-controlled voltage source converter (VC-VSC) [50], [59], [89]. A cascaded outer voltage and inner current control loop based on load current feedforward and decoupling compositions techniques in the  $dq$ -frame is common in this case. However, the voltage reference shall present low-order harmonic components when the PMSG is connected to a nonlinear load or PEI with a diode rectifier, which is very common in practice [90]. Tracking a reference voltage with low-order harmonic components leads to yet another challenge.

The utilization of the PHIL simulation for emulating electrical motors has been discussed in several papers [87], [91]. However, there are just a few published papers on emulation of electric generators [81], [85], [92], especially PMSGs. In [81], a wound rotor synchronous generator (WRSG) is emulated by a VSC with an L filter with the converter employing a single voltage loop using a proportional-integral (PI) controller. In order to avoid the computation of derivative parts, these are neglected and the machine's dynamic characteristics are only represented by the

estimated transfer functions in a voltage type ITM. However, the performance of the emulator under nonlinear loading conditions where the derivative terms play an important role in the computation of the terminal voltages is not presented. In [85], a PMSG is emulated by a VSC with an LC filter using a voltage type ITM. A cascaded inner current and outer voltage control loop with PI controllers is used for regulating the output voltage and frequency of the converter. To deal with computational of the derivative terms, a capacitor is placed at the terminal of the PMSG in the simulation side. However, the sizing of the capacitor and its impact on the emulator performance are not discussed. Moreover, the accuracy of the emulator is not assessed with nonlinear loading conditions. A WRSG emulator is developed in [92] using the current type ITM with which the PMSG emulator cannot operate in standalone mode. Furthermore, the emulator performance is not tested under non-linear loading conditions.

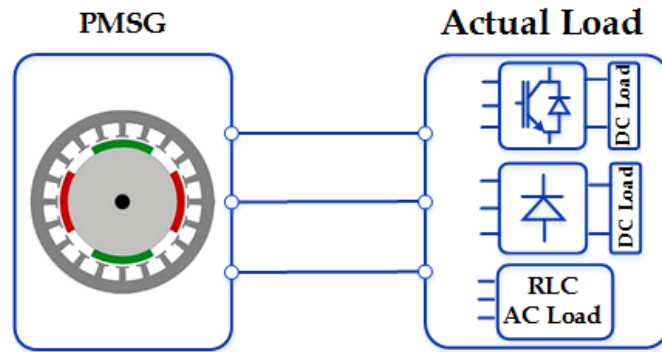
This chapter presents the idea of the PMSG's emulator. A 6-switch converter-based power amplifier combined with a voltage type ITM interface are used to interface the simulation platform with the power amplifier. This is a VC-VSC with an LC filter. A cascaded inner current and outer voltage control scheme using a load compensating feedforward technique is employed to regulate the output voltage and frequency from zero to the maximum rated value. The voltage type ITM method is modified using a virtual impedance connected at the terminals of the generator model in the simulation environment. A procedure for selecting the virtual impedance so as to increase accuracy is employed. A proportional integral plus resonant (*PI+res*) compensator is used in the outer voltage loop, in the *dq*-frame, and inner current control loop to reduce the steady-state error and improve the transient response for both fundamental and low-order harmonic components, e.g. 5<sup>th</sup> and 7<sup>th</sup>. In addition, by using this control strategy, the accuracy performance of the VC-VSC becomes independent of the load characteristics. The emulator is tested, and evaluated with linear and nonlinear loads. Finally, the effectiveness of the modified voltage type ITM with the virtual impedance and developed control strategy and compensation techniques of the converter for the PMSG emulator are verified with experimental results.

## 4.2 PMSG Emulator Configuration

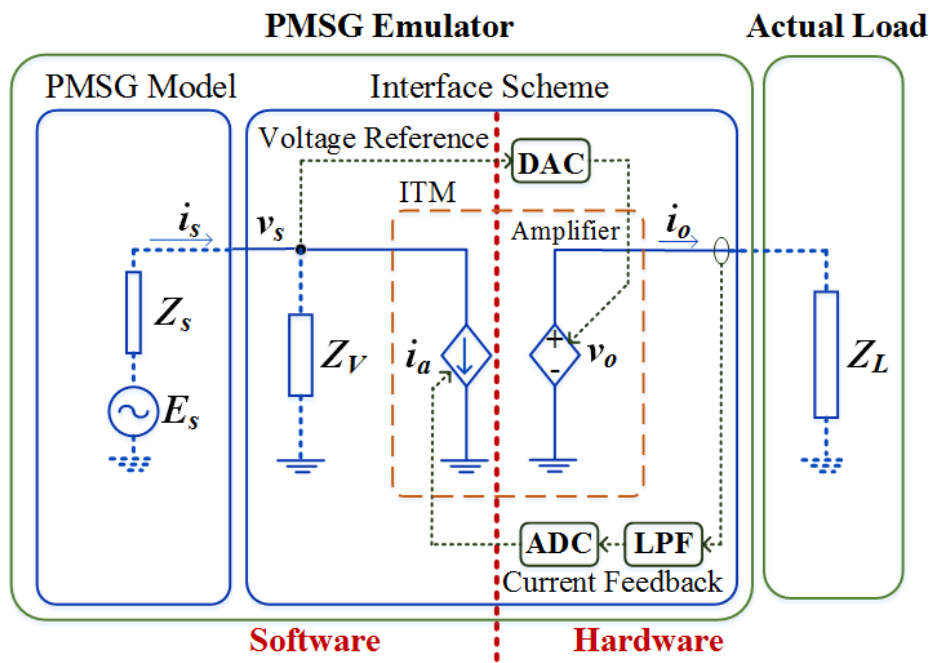
A PMSG emulator system normally consists of three parts, namely [88]: 1) a real-time simulation system, 2) a power amplifier and 3) an interface that connects the simulated system

with the hardware system. Consider the system illustrated in Figure 4.2 (a), where the actual PMSG is directly connected to the actual load in the original system. Figure 4.2 (b) shows a PHIL simulation of the PMSG emulator in which the PMSG and its associated prime mover are modeled in the software and are connected to the actual load through the “interface scheme”. A voltage type ITM is selected for the interface algorithm. In this case, the PMSG terminal voltage  $v_s$  in the simulator is amplified by the power amplifier after passing through the digital-to-analog converter (DAC). The power amplifier operates as a controllable voltage source. The actual load current  $i_o$  from the hardware is measured and transmitted to the real-time simulator, as a feedback signal. A unity-gain current-controlled current source is used to represent the actual load current in the software.

A current sensor, a low pass filter (LPF) to attenuate high-frequency components, and an analog-to-digital converter (ADC) are used in the feedback path. The actual load can be any PEI or RLC load under test. A virtual impedance ( $Z_V$ ) is placed at the generator terminal as shown in Figure 4.2 (b). It helps to build-up voltage at the PMSG stator terminals and then to solve the machine’s ordinary differential equations (ODEs). In fact, the load current feedback with the virtual impedance in the software are used to update the current, voltage, and speed calculation of the PMSG, thus closing the loop. The selection procedure and impact of the virtual impedance on the emulator system performance are addressed in Section 4.5.



(a)



(b)

Figure 4.2 (a) The original system. (b) PHIL simulation for the PMSG emulator.

### 4.3 PMSG Modeling in the Real-Time Simulator

The mathematical model of a PMSG in the rotor reference frame can be formulated using the  $dq$ -frame equivalent circuits which represent the dynamic behavior of the stator voltages and currents, flux linkage and electromechanical torque of the PMSG [84]. The following assumptions are made in the choice of the machine equations.

- Saturation is ignored although it can be considered by parameter changes.

- The back electromotive force (back emf) is considered as sinusoidal.
- Eddy currents and hysteresis losses are ignored.

These assumptions are accurate enough to describe the performance of the PMSG during normal operating conditions. However, a more accurate machine model can be used based on a finite-element analysis (FEA) to accurately describe the machine performance during faults, saturation, etc.

The mathematical model can be represented as

$$\frac{di_{sd}}{dt} = -\frac{1}{L_d}v_{sd} - \frac{R_s}{L_d}i_{sd} + \frac{L_q}{L_d}pi_{sq}\omega_m \quad (4.1)$$

$$\frac{di_{sq}}{dt} = -\frac{1}{L_q}v_{sq} - \frac{R_s}{L_q}i_{sq} - \frac{L_d}{L_q}i_{sd}p\omega_m + \frac{1}{L_q}\psi_{PM}p\omega_m \quad (4.2)$$

$$\frac{d\omega_m}{dt} = \frac{\eta_t}{J_h\omega_m}P_{mec} - \frac{1.5p}{J_h}[\psi_{PM}i_{sq} - (L_d - L_q)i_{sq}i_{sd}] \quad (4.3)$$

where  $v_{sd}$ ,  $v_{sq}$ ,  $i_{sd}$ ,  $i_{sq}$ ,  $L_d$  and  $L_q$  are the stator voltages, the stator currents, and the equivalent inductances of stator windings in  $dq$ -frame, respectively.  $R_s$  is the stator resistance,  $\omega_m$  is the generator mechanical rotor speed,  $\psi_{PM}$  is the flux linkage produced by permanent magnets, and  $p$  is the number of pole pairs.  $P_{mec}$  is the mechanical input power, and  $J_h$  is the system moment of inertia. It is assumed that the PMSG losses can be presented by  $\eta_t$  which is the overall efficiency of the PMSG.

The  $dq$  variables are obtained from  $abc$  variables through the Park transformation and the electrical rotor angular position is given by,

$$\theta = \int p\omega_m dt \quad (4.4)$$

The approximate solution of the mathematical equations of the PMSG and prime mover are obtained using a fourth-order Runge-Kutta method with constant time step. This method is used to solve ODE systems numerically and has the advantage of simplicity and self-starting

regarding implementation on the real-time digital simulator. Figure 4.3 shows the block diagram of the PMSG in the real-time simulator. After solving the generator differential equations, the calculated stator voltages are sent to the power amplifier. The electrical specifications of the emulated PMSG are given in Appendix A.

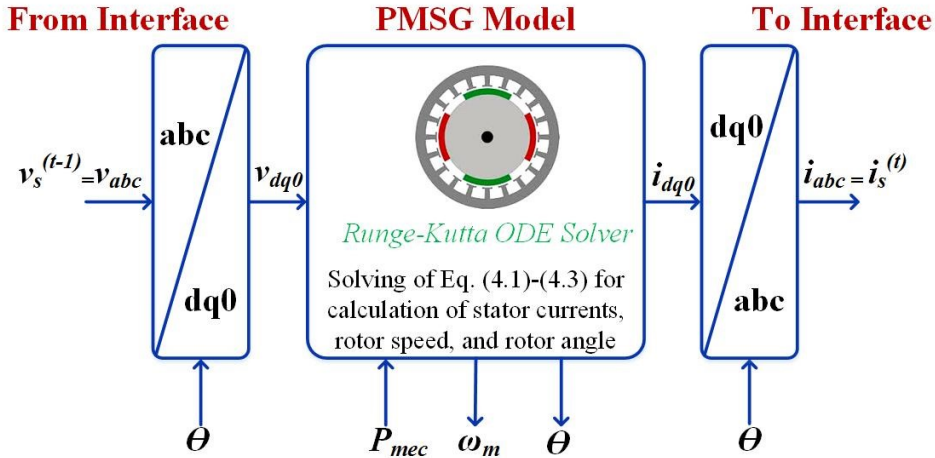


Figure 4.3 Block diagram of the PMSG in real-time simulation platform, where ‘ $t$ ’ is the sampling time.

#### 4.4 VSC Modeling and Control

The converter-based power amplifier includes a 6-switch VSC and a three-phase LC filter, as shown in Figure 4.4 (a). The filter, consisting of the series inductor  $L_F$ , parasitic resistor  $R_F$  and shunt capacitor  $C_F$ , is designed to remove the high-frequency switching components originated by the pulse-width modulation (PWM). A cascaded inner current and outer voltage control scheme in the  $dq$ -frame is employed to regulate load voltage and frequency to the desired reference values. The desired frequency  $\omega$  is set corresponding to the generator frequency. Angle  $\Theta$  required for the  $abc$ -frame to  $dq$ -frame transformation and its inverse is obtained from equation (4.4). The desired output/reference voltages  $v_{od,ref}$  and  $v_{oq,ref}$  are set corresponding to the generator stator voltages,  $v_{sd}$  and  $v_{sd}$ . Figure 4.4 (b) shows the control block diagram including the voltage control scheme, the closed-loop current controller and the model of the capacitor filter in the  $dq$ -frame. It is assumed that the current and voltage controllers of the VSC are designed based on a balanced system. Therefore, the negative and zero-sequence components

in the Park transformation are ignored. A step-by-step procedure to design the current controller and to model the VSC and LC filter in the  $dq$ -frame was presented in Chapter 2. As Figure 4.4 (b) illustrates, the feed-forward compensation terms,  $C_F\omega v_{od}$  and  $C_F\omega v_{oq}$ , have been added to eliminate the coupling between  $v_{od}$  and  $v_{oq}$ . According to the figure,  $v_{od}$  and  $v_{oq}$  can be controlled by the output signals from the voltage control scheme  $i_{id,ref}$  and  $i_{iq,ref}$ . In addition, the feedforward of the load current  $i_{od}$  and  $i_{oq}$  have been added to the voltage control process in order to minimize the impact of the load current on the capacitor voltage [93]. Hence, the voltage closed-loop controller can perform under a wide range of load conditions.

Referring to Figure 4.4 (b),  $i_{id,ref}$  and  $i_{iq,ref}$  in the s-domain are determined as

$$\begin{bmatrix} i_{id,ref}(s) \\ i_{iq,ref}(s) \end{bmatrix} = \begin{bmatrix} u_d(s) \\ u_q(s) \end{bmatrix} + C_F \begin{bmatrix} -\omega v_{oq}(s) \\ \omega v_{od}(s) \end{bmatrix} + \begin{bmatrix} i_{od}(s) \\ i_{oq}(s) \end{bmatrix} \quad (4.5)$$

and

$$\begin{bmatrix} u_d(s) \\ u_q(s) \end{bmatrix} = G_V(s) \begin{bmatrix} v_{od,ref}(s) - v_{od}(s) \\ v_{oq,ref}(s) - v_{oq}(s) \end{bmatrix} \quad (4.6)$$

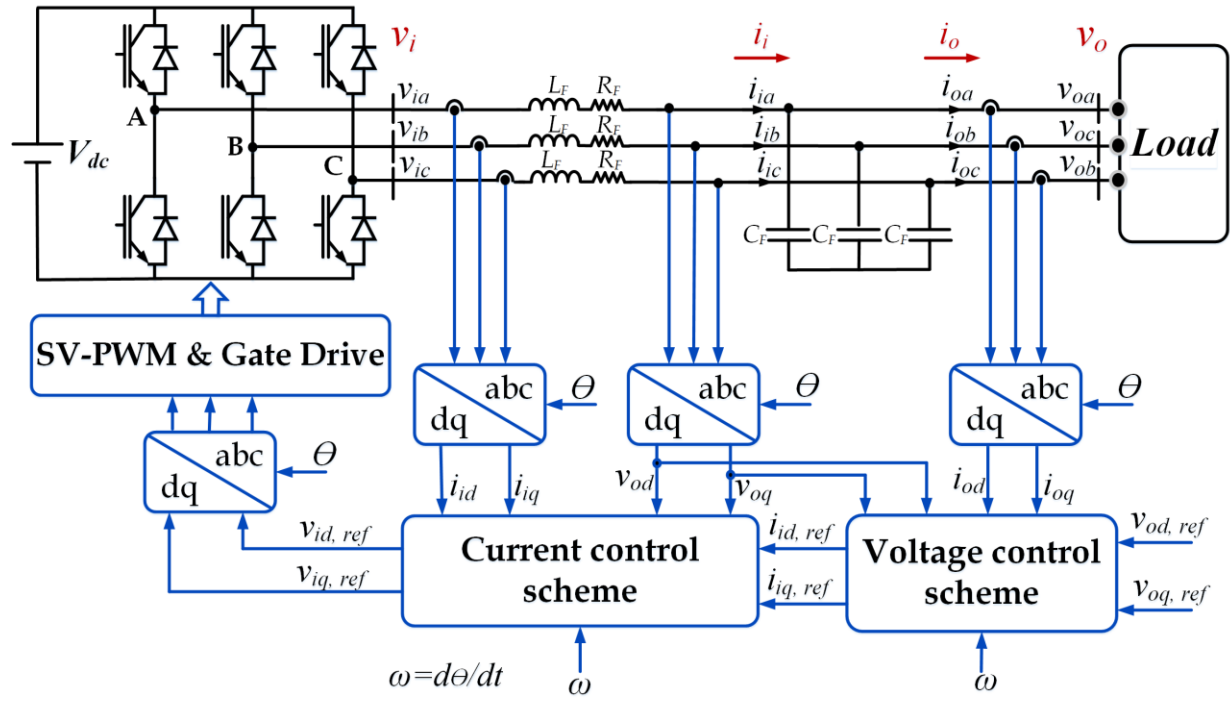
where  $G_V(s)$  represents the voltage controller. The dynamics of the load voltage can be determined in the state-space domain by using Kirchoff's current law at the capacitor node as

$$\frac{dv_{o,abc}}{dt} = \frac{1}{C_F} (i_{i,abc} - i_{o,abc}) \quad (4.7)$$

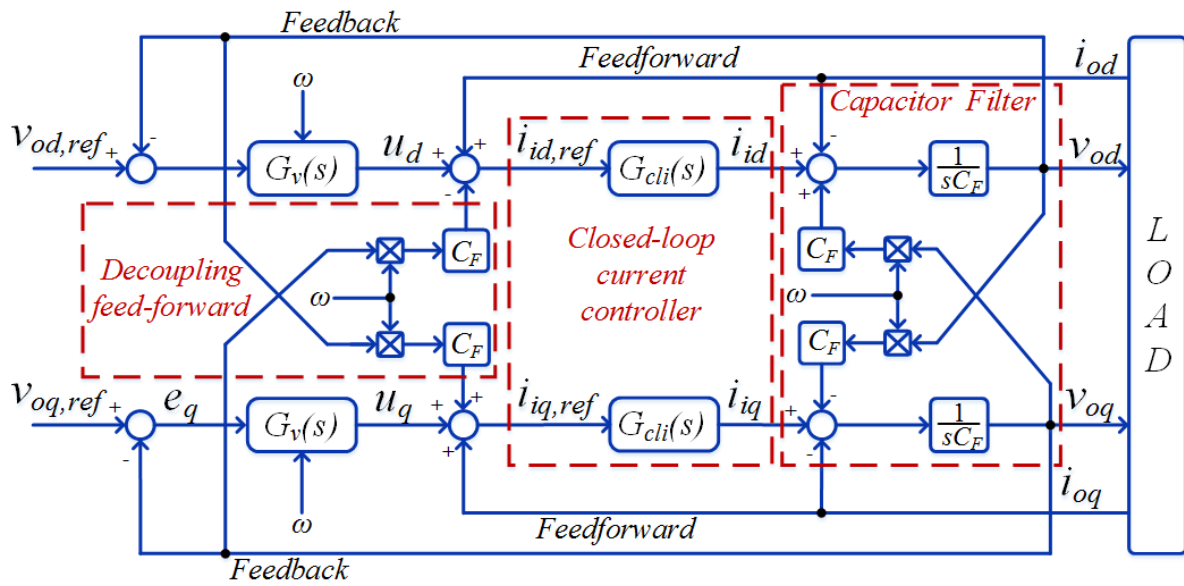
Taking Park and Laplace transformations for both sides of equation (4.7), one obtains:

$$s \begin{bmatrix} v_{od}(s) \\ v_{oq}(s) \end{bmatrix} = \begin{bmatrix} \omega v_{oq}(s) \\ -\omega v_{od}(s) \end{bmatrix} + \frac{1}{C_F} \begin{bmatrix} i_{id}(s) - i_{od}(s) \\ i_{iq}(s) - i_{oq}(s) \end{bmatrix} \quad (4.8)$$

The relationship between  $i_{id}$ ,  $i_{iq}$  and  $i_{id,ref}$ ,  $i_{iq,ref}$  can be determined as



(a)



(b)

Figure 4.4 (a) Schematic diagram of the VC-VSC for the converter-based power amplifier, (b) Control block diagram of the VC-VSC.

$$\begin{bmatrix} i_{id}(s) \\ i_{iq}(s) \end{bmatrix} = G_{cli}(s) \begin{bmatrix} i_{id,ref}(s) \\ i_{iq,ref}(s) \end{bmatrix} \quad (4.9)$$

where  $G_{cli}(s)$  is the closed-loop current controller transfer function and is given as

$$G_{cli}(s) = \frac{G_i(s)G_{PWM}(s)}{L_F s + R_F + G_i(s)G_{PWM}(s)} \quad (4.10)$$

where  $G_{PWM}(s)$  is the transfer function of the PWM block which can be modeled as a first-order transfer function. A proportional-integral (PI) type compensator is chosen for the current controller  $G_i(s)$  as

$$G_i(s) = K_{pc} + \frac{K_{ic}}{s} \quad (4.11)$$

where  $K_{pc}$  and  $K_{ic}$  are the proportional and integral gains of the compensator.  $G_{cli}(s)$  is designed to yield a unity DC gain and a bandwidth with a good rejection of high-frequency disturbances, e.g. one-tenth of the converter switching frequency  $f_{sw}$ .

In order to design the voltage controller, one substitutes  $i_{id}(s)$  and  $i_{iq}(s)$  from equation (4.9) into equation (4.8) and then  $i_{id,ref}$  and  $i_{iq,ref}$  from equation (4.8) in equation (4.5), yielding

$$\begin{bmatrix} v_{od}(s) \\ v_{oq}(s) \end{bmatrix} = G_A(s) \begin{bmatrix} v_{od,ref}(s) \\ v_{oq,ref}(s) \end{bmatrix} + \underbrace{C_F H_Z(s) \begin{bmatrix} \omega v_{oq}(s) \\ -\omega v_{od}(s) \end{bmatrix} - H_Z(s) \begin{bmatrix} i_{od}(s) \\ i_{oq}(s) \end{bmatrix}}_{\text{Transient terms}} \quad (4.12)$$

where

$$G_A(s) = \frac{G_{cli}(s)G_v(s)}{C_F s + G_{cli}(s)G_v(s)} \quad (4.13)$$

$$H_Z(s) = \frac{(1 - G_{cli}(s))}{C_F s + G_{cli}(s)G_v(s)} \quad (4.14)$$

From equation (4.12), one can see that the output voltage is a function of both the reference voltage and the load current.  $G_A(s)$  is the closed-loop voltage transfer function and  $H_Z(s)$  is the

system output impedance transfer function which determines the “transient terms” of equation (4.12).

In equation (4.12),  $[1-G_{cli}(s)]$  has a zero DC gain because  $G_{cli}(s)$  is designed to yield unity DC gain. Therefore,  $H_Z(s)$  as well as the “transient terms” of equation (4.12) reduce to zero in the steady-state. To obtain a fast attenuation to zero of the “transient terms” of equation (4.12),  $G_{cli}(s)$  must have a fast transient response.

The voltage controller  $G_V(s)$  needs to be designed so that the load voltages can achieve an asymptotic tracking of the reference voltages with a fast transient response under linear and nonlinear loading conditions. If the converter is connected to a linear load leading to sinusoidal PMSG load currents as well as PMSG stator voltages, the  $dq$ -frame components are DC quantities. So, a standard proportional-integral (PI) controller can be employed for  $G_V(s)$ . The controller has a large gain at zero frequency eliminating the steady-state error and  $G_A(s) \rightarrow 1$ . However, when the converter is connected to a nonlinear load, distortion appears in the PMSG stator voltage due to the load current harmonics. This will create additional AC components in the  $dq$  variables at specific frequencies related to the fundamental and low-order harmonics in the stationary frame. Hence, PI controllers encounter difficulties to eliminate the error in steady-state since they have a large gain only at zero Hz. A proportional plus resonant ( $P+res$ ) controller has been proven to eliminate the steady-state error effectively for a sinusoidal reference signal in the stationary frame [94]. In this Chapter, to obtain an effective reference voltage tracking a proportional-integral plus resonant ( $PI+res$ ) is employed for the voltage control loop in the  $dq$ -frame. The transfer function of the  $PI+res$  controller is given by equation (4.15).

$$G_V(s) = \underbrace{K_{Pv} + \frac{K_{Iv}}{s}}_{PI} + \underbrace{\frac{2K'_{Iv}\omega_{cu}s}{s^2 + 2\omega_{cu}s + \omega_0^2}}_{Resonance} \quad (4.15)$$

where  $K_{Iv}$ ,  $K_{Pv}$ , and  $K'_{Iv}$  are the gains of the proportional, integral and resonant terms of the voltage controller.  $\omega_{cu}$  and  $\omega_0$  are the cut-off and resonant frequencies. At  $\omega_0$ , the controller introduces a large gain, making the steady-state error very small.  $\omega_0$  must be tuned continually since the emulator is supposed to work under variable frequency. In addition, the  $PI+res$

controller has the capability of double harmonic compensation [95]. For example, when the converter is connected to a three-phase nonlinear load e.g. diode rectifier, the fifth ( $-5\omega$ ) and seventh ( $7\omega$ ) harmonic components are present in the PMSG stator voltage. In the dq-frame, the 5th and 7th harmonic components appear in two rotating frames at  $-5\omega - \omega = -6\omega$  and  $7\omega - \omega = 6\omega$ . By setting  $\omega_0$  at  $6\omega$ , one provides a high gain for replicating the 5<sup>th</sup> and 7<sup>th</sup> voltage harmonic components. The parameter values of the converter-based power amplifier are provided in the Appendix A. The controller gains were selected using MATLAB control system toolbox in order to obtain a zero steady-state error to a step reference signal and desired bandwidth and phase margin [78]. Considering the given LC filter and switching frequency, the current controller was designed for 1.2 kHz bandwidth and  $68^\circ$  phase margin and the voltage controller was designed for 100 Hz bandwidth and  $50^\circ$  phase margin. The resonance gains of the voltage controller were selected so that a finite gain of around 40 dB was obtained for the resonant peak, which is satisfactory for attenuating the harmonics tracking error. The parameter values of the VC-VSC are provided in the Appendix A.

Figure 4.5 shows the Bode plot of  $G_v(s)$ ,  $G_A(s)$  and  $H_Z(s)$  when  $\omega_0$  is  $2\pi 60 \times 6$  rad/s, corresponding to the sixth order harmonic of the fundamental frequency of the generator terminal voltage at the maximum rotor speed (60 Hz). Indeed, based on the generator rotor speed,  $\omega_0$  changes from zero to  $2\pi 60 \times 6$  rad/s which 60 is the maximum electrical frequency. From the voltage controller  $G_v(s)$ , the gain at a very low frequency (e.g. 0.01 rad/s) is 50 dB and the gain at the resonance frequency is 40 dB. From the closed-loop voltage transfer function  $G_A(s)$ , the gain at a very low frequency (e.g. 0.01 rad/s) is 0 dB with a phase of  $0^\circ$  and the gain at the resonance frequency is -0.0082 dB with a phase of  $0.0056^\circ$  in response to the reference voltage. From the system output impedance transfer function  $H_Z(s)$ , at a very low frequency (e.g., 0.01 rad/s) is -150 dB and the gain at the resonance frequency is -106 dB in response to the load current. Therefore, the output voltage should track the reference voltage effectively while the VC-VSC closed-loop control performance becomes independent of the load dynamic properties, e.g. linear or nonlinear loads.

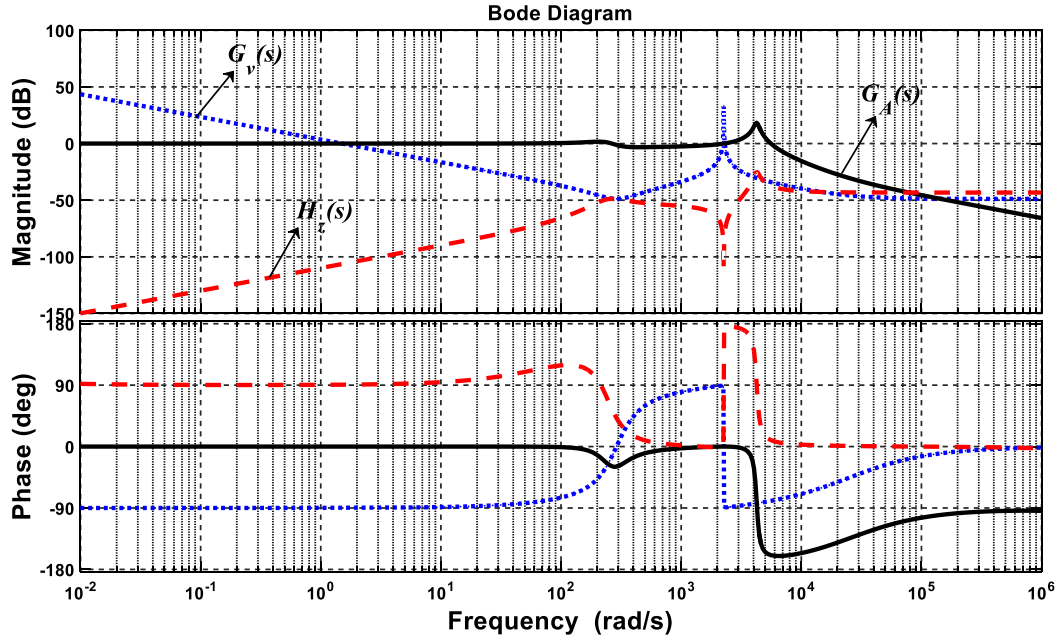


Figure 4.5 Bode plot of  $G_v(s)$ ,  $G_A(s)$  &  $H_r(s)$  when  $\omega_0 = 2\pi 60 \times 6$  rad/s.

#### 4.5 Virtual Impedance Selection and Performance Considerations

Figure 4.6 (a) and (b) show the block diagram of the original system and the PMSG emulator system developed with a voltage type ITM and the virtual impedance, respectively. In this figure,  $E_s$  is the generator back electromotive force (EMF),  $G_A(s)$  is the power amplifier transfer function (equation (4.13) ),  $G_I(s)$  is the current feedback filter transfer function,  $Z_S(s)$  is the PMSG stator equivalent impedance,  $Z_L(s)$  is the load equivalent impedance and  $e^{-Ts}$  is the total delay of the emulator including measuring and converting devices and the power amplifier where  $T$  is the time delay.

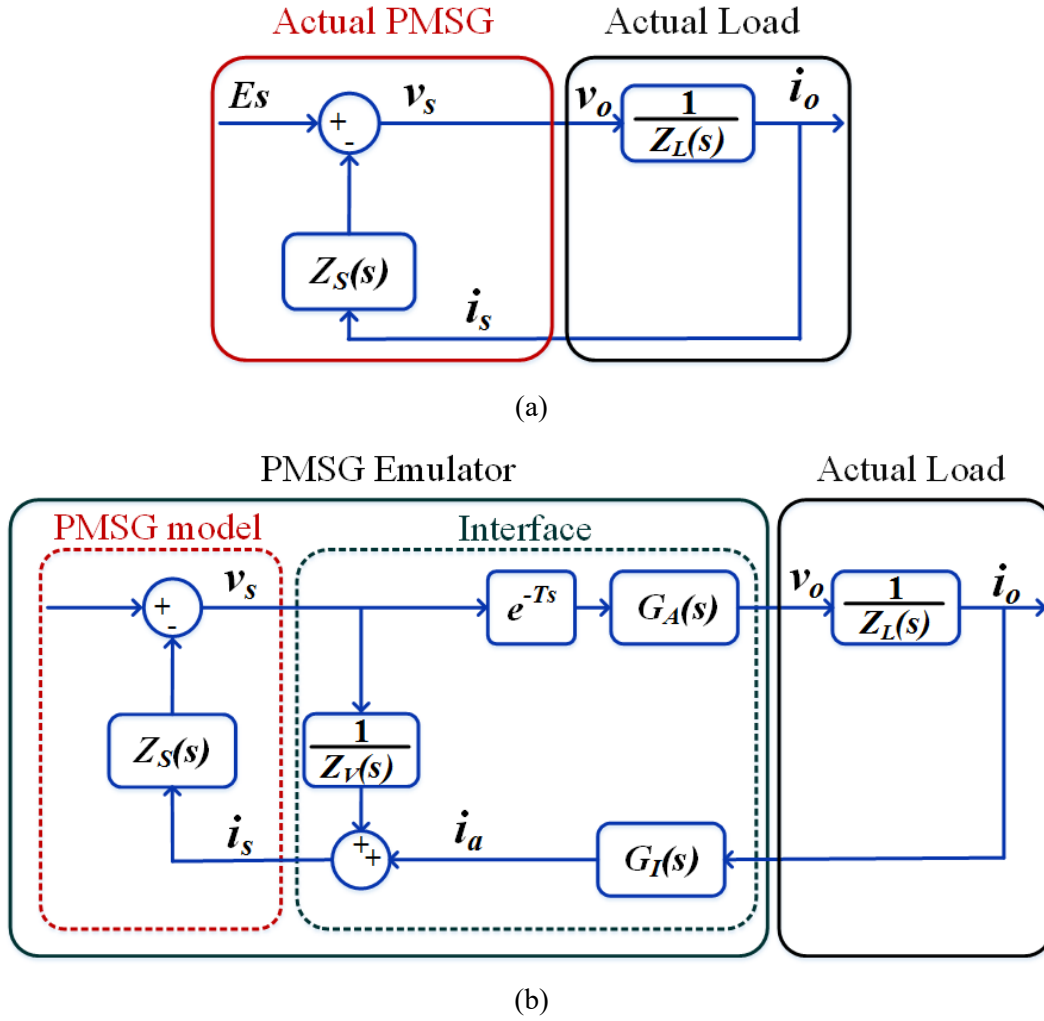


Figure 4.6 Block diagrams: (a) original system, (b) PMSG emulator with the modified voltage type ITM

$G_I(s)$  represents the transfer function of a LPF in the feedback load current signal and can be given as

$$G_I(s) = \frac{\alpha}{s + \alpha} \quad (4.16)$$

where  $\alpha$  is the corner frequency of the LPF.  $\alpha = 10k$  is selected for  $G_I(s)$  to attenuate high-frequency components emerging out of the numerical computations while it has a minimum impact on the low order current harmonics.

$e^{-Ts}$  is represented by the first-order Padé approximation [78] and can be given as

$$e^{-Ts} = \frac{-s + \beta}{s + \beta}, \quad \beta > 0 \text{ and } \beta = 2/T \quad (4.17)$$

The time delays of the voltage and current Hall sensors used for voltage and current measurements, and the delay of PWM module are small and are neglected.

The virtual impedance  $Z_V(s)$  can be calculated by considering the system accuracy. The accuracy of the PMSG emulator can be assessed by the transfer function perturbation (TFP)-based method suggested by [81], [96], [97].

The closed-loop transfer function of the original system can be obtained as

$$G_{CL, OS}(s) = \frac{1}{Z_S(s) + Z_L(s)} \quad (4.18)$$

and the closed-loop transfer function of the proposed PMSG emulator can be obtained as

$$G_{CL, ES}(s) = \frac{i_o(s)}{E_S(s)} = \frac{G_A(s)Z_V(s)e^{-Ts}}{Z_L(s)Z_V(s) + Z_S(s)G_A(s)G_I(s)Z_V(s)e^{-Ts} + Z_S(s)Z_L(s)} \quad (4.19)$$

Thus, the relative error between the closed-loop transfer function of the original system and the closed-loop transfer function of the proposed PMSG emulator can be defined as

$$Error(s) = \left| \frac{G_{CL, ES}(s) - G_{CL, OS}(s)}{G_{CL, OS}(s)} \right| \quad (4.20)$$

In order to eliminate the error defined by equation (4.20),  $G_{CL, ES}(s)$  should be equal to  $G_{CL, OS}(s)$ . In order to make equation (4.18) equal to equation (4.19), the impedance  $Z_V(s)$  can be calculated as

$$Z_V(s) = \frac{Z_L(s)Z_S(s)}{G_A(s)(Z_S(s) + Z_L(s))e^{-Ts} - G_A(s)G_I(s)Z_S(s)e^{-Ts} - Z_L(s)} \quad (4.21)$$

Although obtaining equation (4.21) is straightforward, it is defined as the ratio of different transfer functions. Therefore, the implementation of  $Z_V$  into the real time simulation platform presents serious challenges. Figure 4.7 shows the Bode diagram of equation (4.21) with changing loads. The loads are considered resistive or/and inductive types since they are the main loads in power system. One can see that the frequency response of  $Z_V(s)$  is nearly independent of  $Z_L(s)$ . Furthermore, one can observe that the performance of  $Z_V(s)$  is similar to that of a series RLC impedance. It is capacitive in the low frequency and is inductive in the high frequency range. At the resonance frequency, which is between 6 Hz and 60 Hz, it is resistive. Figure 4.8 shows the comparison of the frequency response of equation (4.21) with the proposed series RLC impedance. Its impedance in the s-domain can be defined as

$$Z_{RLC}(s) = \frac{L_V C_V s^2 + R_V C_V s + 1}{C_V s} \quad (4.22)$$

Where  $C_V$ ,  $L_V$ , and  $R_V$  are the capacitor, inductor and resistor of the RLC virtual impedance/filter. The parameters of the RLC virtual impedance are tuned in order to match the frequency response of equation (4.21) and it can be implemented in the software platform properly. This is a simple solution easy to implement. The parameter values of the transfer functions mentioned above are given in the Appendix A.

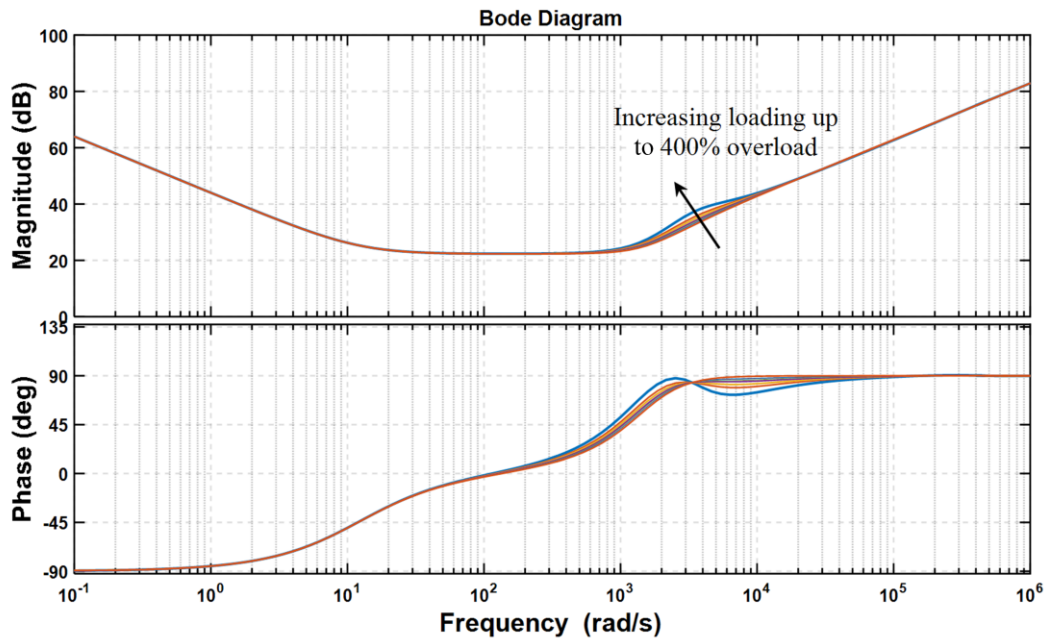


Figure 4.7 Bode diagram of (4.21) with changing loads up to 400% overload for the purely resistive and resistive-inductive load impedances.

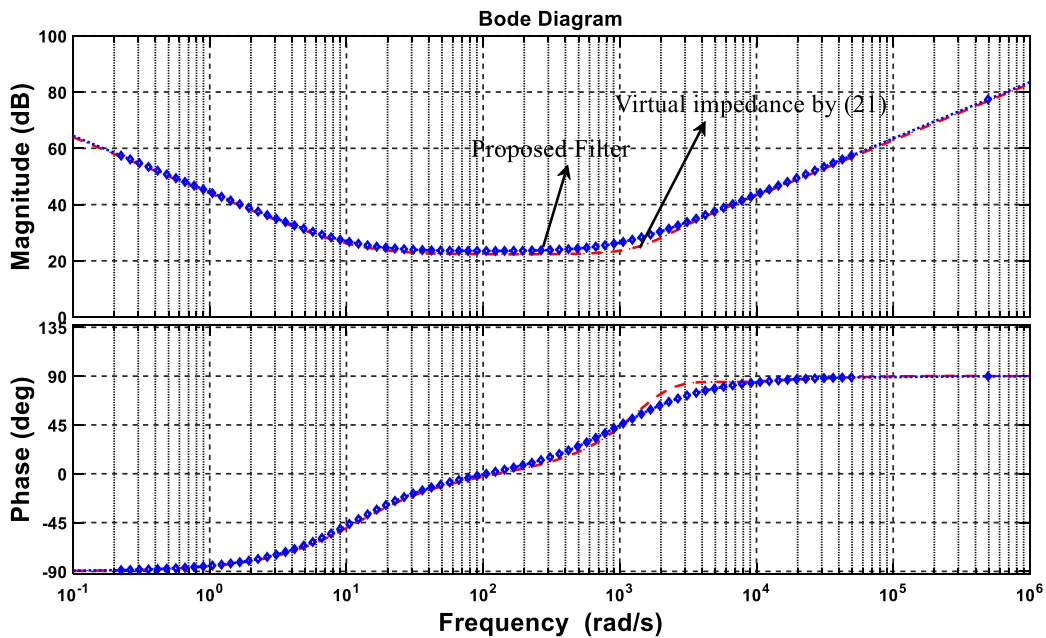


Figure 4.8 Comparison of the frequency responses of the virtual impedance calculated by (4.21) and proposed series RLC impedance/filter.

## 4.6 Experimental Observations and Discussions

To assess the performance of the proposed PMSG emulator, one was built and tested under various conditions. The selected PMSG for emulation is an actual 4-pole PMSG which is available in the laboratory. The parameter values of the PMSG are given in Appendix A. Figure 4.9 shows a picture with the complete system implemented in the laboratory for the power electronic converter-based PMSG emulator. The simulation part consists of the PMSG model, the virtual impedance and the control system of the VSC which are implemented in MATLAB/Simulink. Using dSPACE real-time interface (RTI), and Simulink Coder™, the Simulink models are compiled and downloaded into a dSPACE DS1103 controller board and then started on the real-time hardware automatically.

In this Chapter, the fourth-order Runge-Kutta method with constant time step is selected as the simulation solver. The minimum possible execution sampling time for implementing the PMSG model and control schemes of the emulator is obtained as 80  $\mu$ s. This defines the switching frequency of the converter, corner frequency of the low pass filter (LPF) and bandwidth of the cascaded control loops. Nonetheless, with this sampling time, one can replicate both fundamental and low-order harmonic components (5<sup>th</sup> and 7<sup>th</sup>) of the output voltage. However, for replicating high transient response of the system for other low-order harmonics e.g. 11<sup>th</sup> and 13<sup>th</sup> and achieving high accuracy, choosing a faster processor than was used and redesigning of controller and LC filter parameters of the power converter would be beneficial.

In addition, the PMSG emulator is designed to work for most normal operating conditions where the amplitude ratio of the source impedance including the virtual impedance to load impedance is less than one. In these cases, the stability of the voltage type ITM is guaranteed as discussed in [96]. Conversely, the PMSG emulator cannot work under a short circuit condition. The hardware part consists of the converter including 1200 V - 50 A IGBT half-bridge modules, LC filter and voltage and current hall-effect sensors. The developed PMSG emulator is designed based on a power converter rated at 11 kVA while the fundamental frequency and voltage range changes between 0 and 60 Hz, and between 0 and 220 V, respectively.

It is assumed that the generator is driven by a prime mover in which the input power/torque can be changed as a time-varying input in the simulation side. Different scenarios are considered to verify the emulator performance. First, the emulator is tested with both linear and nonlinear

loads. The linear load consists of a resistive three-phase set while the nonlinear one is realized with a three-phase diode bridge rectifier and a resistive element. Then, the effect of the virtual impedance on the emulator’s performance is investigated. The experimental results shown in the following Section were obtained with dSPACE Control Desk.

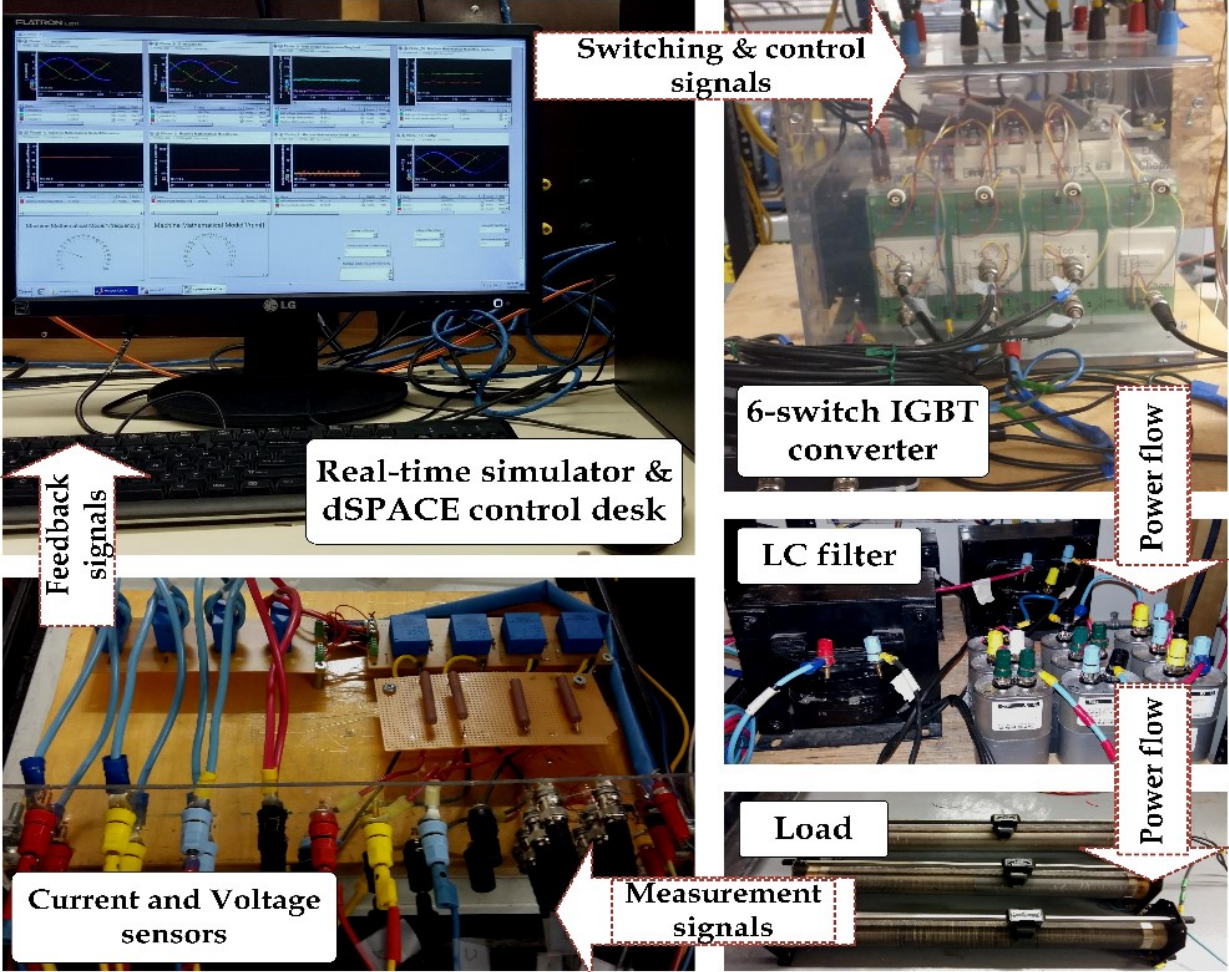


Figure 4.9 Experimental setup.

#### 4.6.1 Changing the Input Power with a Constant Load Impedance

In this sub-Section, the performance of the PMSG emulator with the suggested  $Z_V$  is tested during startup, steady state, and run down by changing the input power while keeping the actual

load impedance constant. The input power changes as shown in Figure 4.10. The emulator is tested with both linear and nonlinear loads. The former consists of a three-phase set of  $R_{ac} = 20 \Omega$ /phase and the latter concerns a three-phase diode rectifier with a resistive load of  $R_{dc} = 20 \Omega$ . The PMSG model results,  $v_s$  and  $i_s$ , are obtained from the simulation while the PMSG emulator results,  $v_o$  and  $i_o$ , are measured from the hardware as shown in Figure 4.2. Moreover, as mentioned before, selecting the value of the virtual impedance has an impact on the accuracy of the emulator. This accuracy can be demonstrated by the difference between waveforms of  $i_s$  and  $i_o$ , and waveforms of  $v_s$  and  $v_o$ .

Figure 4.11 (a), (b) and (c) show test results of the phase voltage, phase current and frequency of the PMSG emulator for the linear load. One can observe that the emulator is able to operate under different operating conditions, startup, generated output power and shutdown. The PMSG emulator is accelerated and decelerated according to the inertia of the machine and input power variations. The increase/decrease in the magnitude and frequency of the output voltage and current can be observed in both the PMSG model and PMSG emulator during start up/ run down. Figure 4.11 (d) and (e) show a zoomed-in view of the voltage and current waveforms of the PMSG model and PMSG emulator and the absolute error between them for a linear load. There, it can see that there is a good agreement between them. The maximum absolute error is 0.03 pu for the voltage and 0.04 pu for the current waveforms.

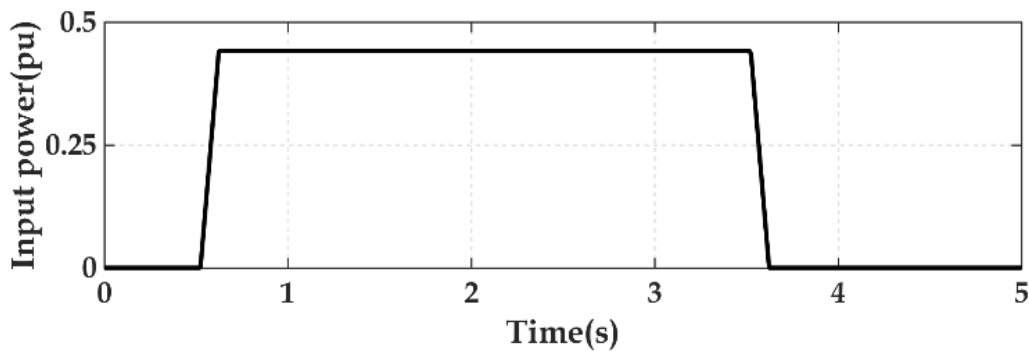


Figure 4.10 Variation of the PMSG emulator input power.

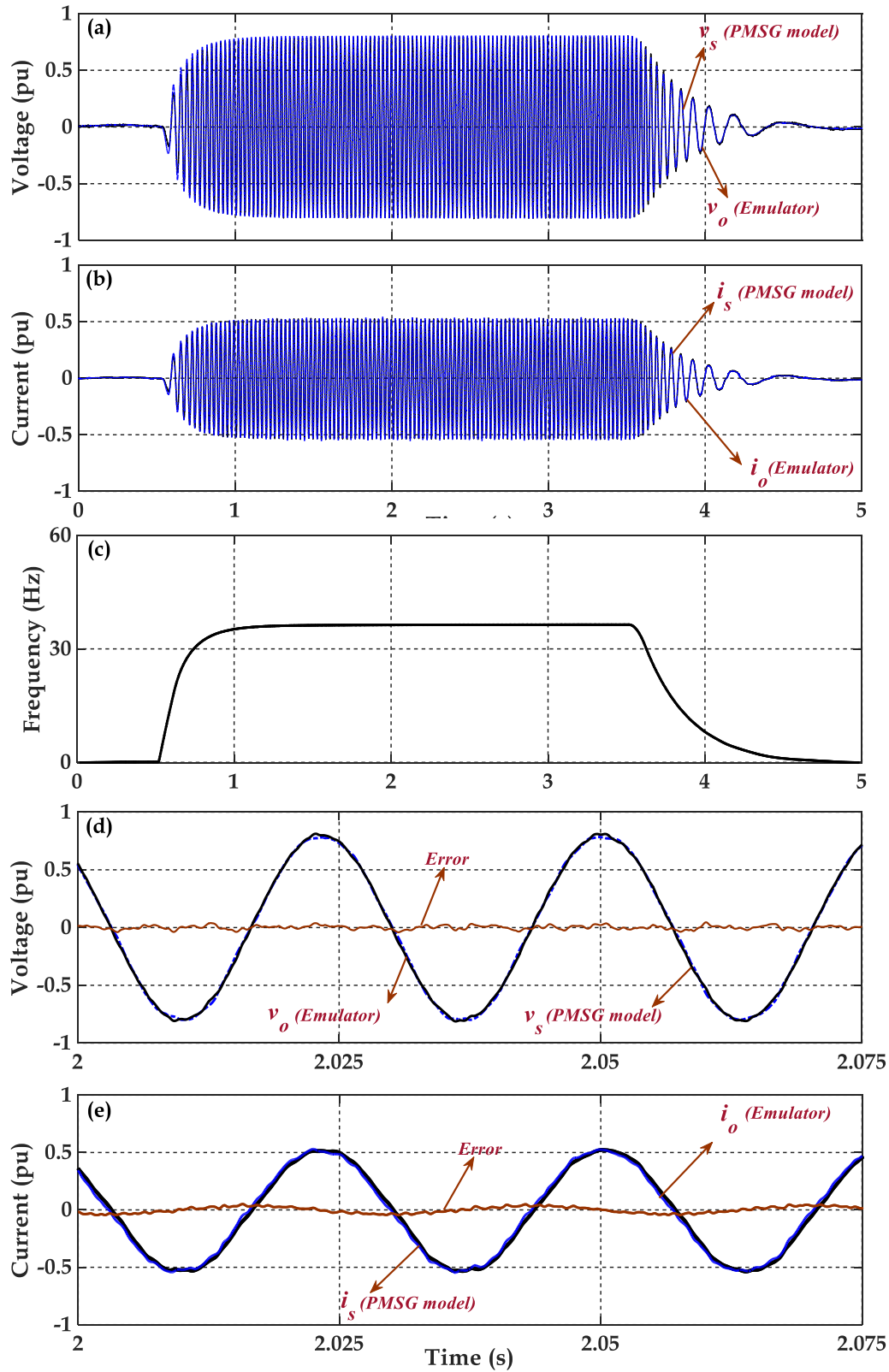


Figure 4.11 Test results of the PMSG emulator connected to a linear load; (a) phase voltage, (b) phase current, (c) frequency, (d) zoomed-in voltage around  $t = 2$  s, (e) zoomed-in current around  $t = 2$  s.

Figure 4.12 (a) and (b) show the harmonic spectra of the voltage and current waveforms of the PMSG model and emulator for the linear load. The fundamental component of both voltage and current waveforms, at 37 Hz, are matched. The absolute errors for the voltage waveforms at 185 Hz (5<sup>th</sup> harmonic) and at 259 Hz (7<sup>th</sup> harmonic) are 0.007 pu and 0.003 pu, respectively. The absolute error for the current waveforms at both the 5<sup>th</sup> harmonic and 7<sup>th</sup> harmonic are less than 0.0005 pu.

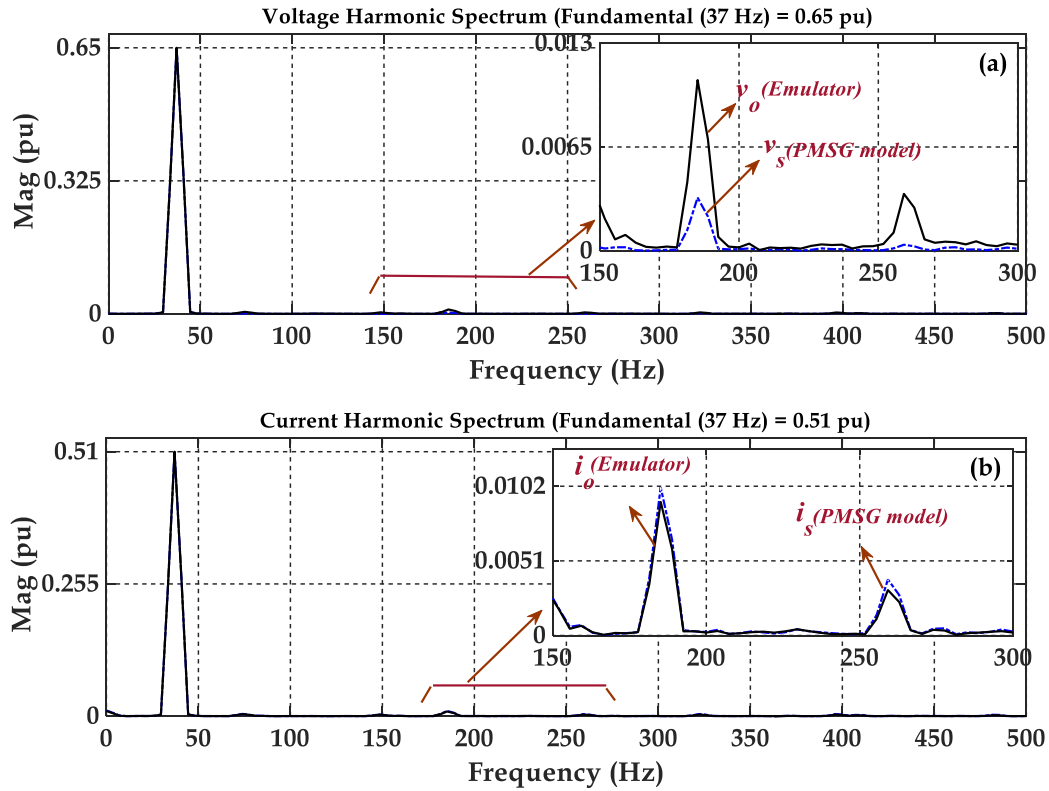


Figure 4.12 Harmonic spectra of the PMSG emulator connected to a linear load; (a) voltage, (b) current.

Figure 4.13 (a), (b) and (c) show the test results of the phase voltage, phase current and frequency of the PMSG emulator for the nonlinear load. Similar to the linear load, the emulator is able to operate under different operating conditions such as start-up, generated output power and shutdown. Figure 4.13 (d) and (e) show a zoomed-in view of the voltage and current waveforms of the PMSG model and PMSG emulator and the absolute error between them for the nonlinear load. It can see that the emulated waveforms with the suggested control strategy properly follow the PMSG model. The maximum error is 0.05 pu for the voltage waveforms and 0.06 pu for the current waveforms.

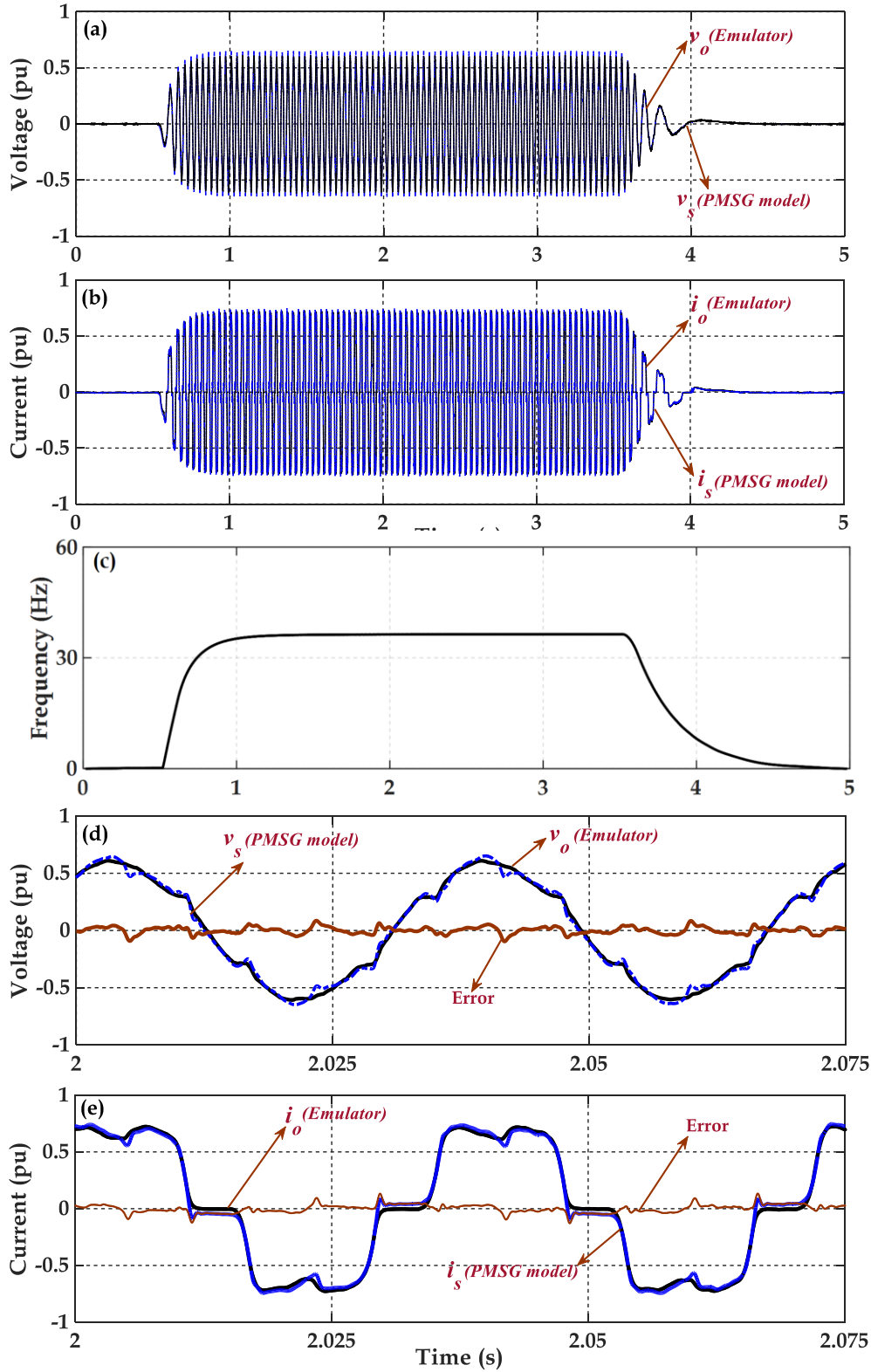


Figure 4.13 Results of the PMSG emulator connected to a non-linear load; (a) phase voltage, (b) phase current, (c) frequency, (d) zoomed-in voltage around  $t = 2$ s, (e) zoomed-in current around  $t = 2$ s.

Figure 4.14 (a) and (b) show the harmonic spectra of the voltage and current waveforms of the PMSG model and emulator supplying a nonlinear load. The fundamental components of both voltage and current waveforms, at 27 Hz, are matched. The current harmonic spectrum of the PMSG model are very similar by the emulator one. The absolute error between the current waveforms at 135 and 189 Hz, the 5<sup>th</sup> and 7<sup>th</sup> harmonics, are less than 0.0006 pu. The absolute error at the 5<sup>th</sup> and 7<sup>th</sup> harmonics of the voltage waveforms, are calculated as 0.011 pu and 0.005 pu, respectively. Figure 4.15 (a) and (b) show two cycles of the voltage and current waveforms of the PMSG model and emulator for the linear load in  $dq$ -frame. One can see that the 6<sup>th</sup> harmonic appears in d and q rotating frames, as discussed in Section 4.4. Moreover, the emulated waveforms in  $dq$ -frame with the suggested control strategy properly follow the PMSG model. This means that the proposed PI+res controller for the VSC is able to reduce the steady-state error and improve the transient response for fundamental and two low-order harmonic components: 5<sup>th</sup> and 7<sup>th</sup>.

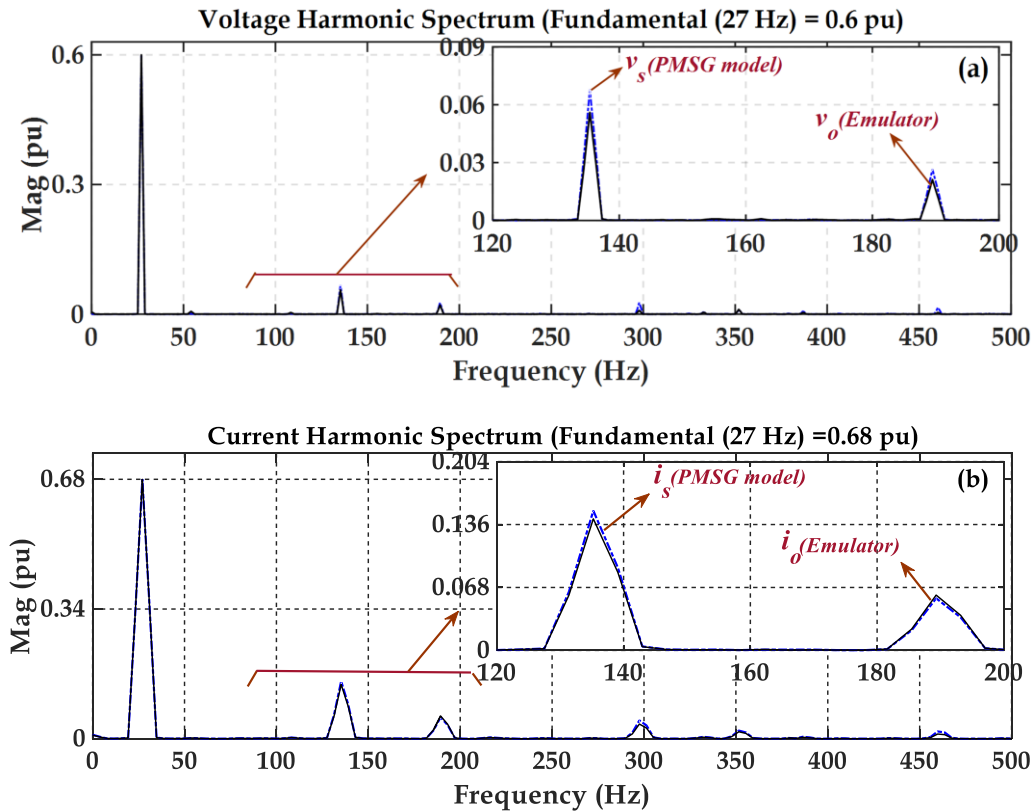


Figure 4.14 Harmonic spectra of the PMSG emulator connected to a nonlinear load; (a) voltage, (b) current.

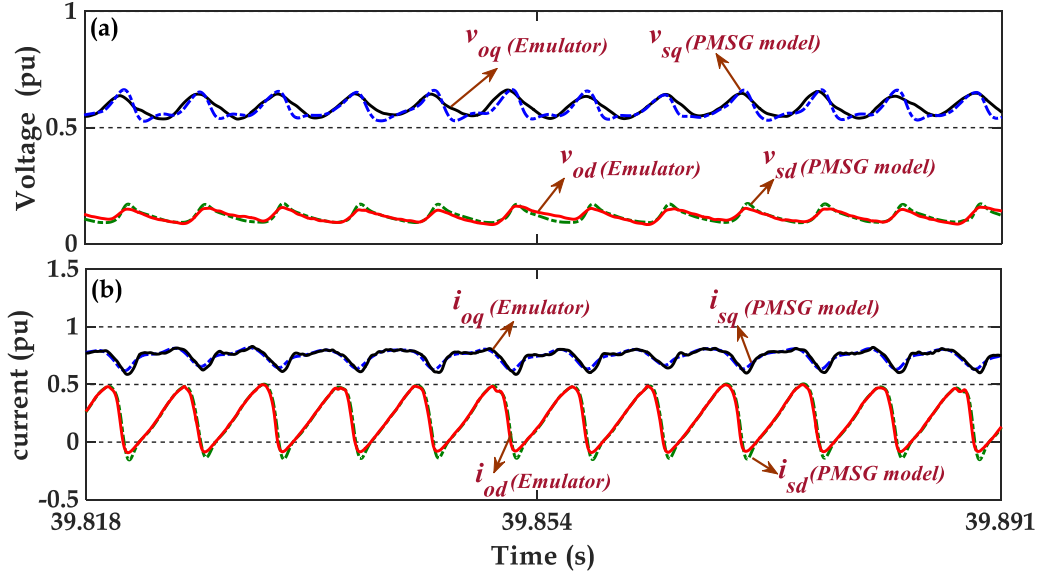


Figure 4.15 Results of the PMSG emulator connected to a non-linear load; (a) voltage in dq-frame, (b) phase current in dq-frame for 2 cycles waveform.

#### 4.6.2 Effect of the Virtual Impedance on the Emulator's Performance

In order to show the effect of the choice of the virtual impedance on the emulator's performance, a series resistive-capacitive (RC) filter is also considered as the virtual impedance. This is a case-study to verify its impact on the accuracy of the emulator when the load current has low-order harmonic components. Such virtual impedance behaves similarly to the one presented in [85]. The parameter values of the RC filter are selected so that the virtual impedance has lower impedance magnitude at frequencies above 60 Hz compared with the proposed virtual impedance as shown in Figure 4.8. Therefore, the high frequencies components ( $> 60$  Hz) of load current  $i_o$  are passed into the virtual impedance and reduced in the PMSG model current  $i_s$ . Then the accuracy of the system decreases at high frequencies since it depends on the difference between  $i_o$  and  $i_s$ . The RC filter is selected with  $R_V = 5 \Omega$ ,  $C_V = 5 \text{ mF}$ . It has 6.1 dB impedance magnitude for frequencies above 60 Hz and 60 dB impedance amplitude at zero frequency. The emulator is tested with a nonlinear load which is a three-phase diode rectifier with a resistive load of  $R_{dc} = 20 \Omega$ . The frequency of the output voltage of the emulator is measured as 28 Hz for a given input power. Figure 4.16 (a) and (b) show test results of the phase voltage and phase current of the PMSG emulator with the RC filter as virtual impedance. One can see that the PMSG model current  $i_s$  does not match the emulator load current  $i_o$ . The maximum absolute

error is 0.08 pu for the voltage and 0.42 pu for the current waveforms. Therefore, the RC filter introduces a large error when the load waveform presents fast varying components.

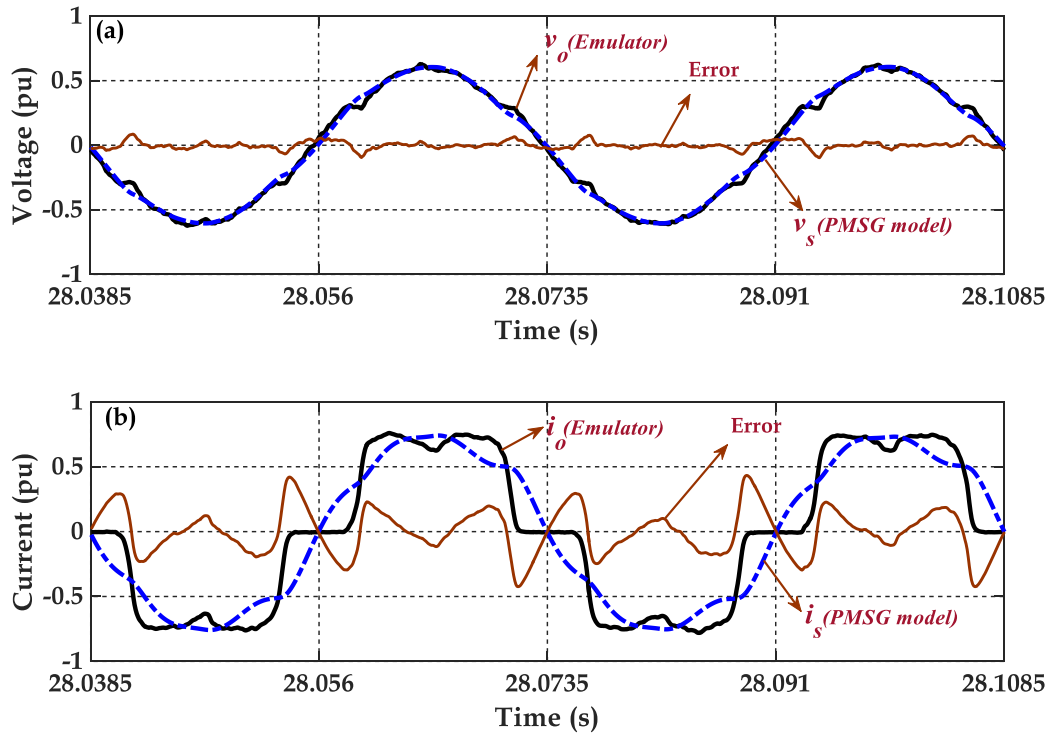


Figure 4.16 Test results of the PMSG emulator using two different virtual impedances. (a) Phase voltage, (b) phase current.

## 4.7 Summary

A converter-based PMSG emulator as a testbed for testing and developing generator's power electronic interfaces and its control system was reported in this Chapter. The model of the PMSG is formulated in a real-time simulator. A VC-VSC is used as a converter-based power amplifier. A virtual impedance, included in the software side, was proposed to improve the performance of the voltage type ITM interface for emulating an electrical generator. It is shown that it can be represented by a simple series RLC filter and its parameter can be selected irrespective of the load impedance value. A proportional-integral plus resonant controller is proposed for the voltage controller of the VSC in the  $dq$  frame. It is shown that the controller provides suitable voltage tracking not only for the fundamental component of variable frequency, but also for the 5<sup>th</sup> and 7<sup>th</sup> harmonic components that appear when the PMSG supplies non-linear loads. The

accuracy of the system has been analyzed. Experimental results were presented to validate the overall PMSG emulator performance during startup, steady state, and run down. The results have demonstrated that the proposed PMSG emulator performs well with high accuracy for both linear and nonlinear loading conditions. Thus, the proposed PMSG emulator can be used as a testbed for testing and developing wind/hydrokinetic energy conversion systems.

## Chapter 5. Power and Frequency Support Control for a Storage-less Diesel Hydrokinetic Microgrid

*This chapter presents an active power sharing control strategy for a storage-less diesel-hydrokinetic (D-HK) microgrid with high or medium penetration of hydrokinetic power to mitigate: 1) the effect of the grid frequency fluctuation due to instantaneous variation in the water speed/load, and 2) light loading operation of the diesel engine. The diesel generator set (genset) works based on a power vs. frequency droop control. To achieve the above objectives, a supplementary control loop that includes virtual inertia and frequency droop control is added to the conventional control system of a hydrokinetic energy conversion system (HKECS). The conventional control scheme is the maximum power point tracking (MPPT) control. By adding the supplementary control loop, the hydrokinetic turbine (HKT) operates in a deloaded mode to obtain sufficient reserve power on a continuous basis for the frequency support control. Also, the HKECS output power can change continuously between the maximum power point and the maximum deloading (DL) percentage of the turbine and delivers power to the grid according to the loading conditions of the genset. The HKECS includes a fixed-pitch HKT, a permanent magnet synchronous generator (PMSG) and a low-cost power electronics interface including three-phase diode rectifier, DC-DC boost converter and three-phase inverter. The proposed strategy is experimentally verified with electromechanical-based diesel engine and HKT emulators controlled via a dSPACE® rapid control prototyping system. The transient and steady-state performances of the system, including grid frequency and power balancing control, are demonstrated.*

### 5.1 Introduction

A large number of remote communities in northern Canada rely on diesel generator sets (gensets) [4]. The cost of electricity and environmental concerns suggest that hydrokinetic energy, as a renewable energy source, is a suitable alternative for power generation. A diesel-hydrokinetic (D-HK) microgrid has potential to reduce CO<sub>2</sub> emissions, fossil fuel consumption, and cost [98]. While a low level of hydrokinetic power penetration can be handled by the genset control system, a large or medium penetration level will have a negative effect on the transient and steady-state performance of the small-scale (1-100 kW) diesel hybrid microgrid. This is due

to the stochastic nature of water speed and variable load patterns [62]. It should be noted that the D-HK microgrids have not been extensively explored in the literature thus far. Therefore, some characteristics of D-HK systems are extended from diesel-wind (D-W) systems in this Chapter since most of their technical aspects are similar [28], [99]. However, the equivalent moment of inertia of an HKT is much greater than a wind turbine with the same power rating [31], [32], [100]. For example, the total moment of inertia for a 50 kW HKT is about 8407 kg.m<sup>2</sup> [32] while this value is around 1775 kg.m<sup>2</sup> for a 50 kW wind turbine [100].

A permanent magnet synchronous generator (PMSG)-based HKECS connects to the microgrid through a full-rated back-to-back power electronics converter [90], [101]. Considering variable water conditions, if the operation of maximum power point tracking (MPPT) is required, for a fixed-pitch HKT, the shaft speed of the turbine-generator has to be variable which is realized by the control scheme of the converter. However, with the medium and high penetration level of the hydrokinetic power, if the HKT operates with MPPT, the diesel genset might work with light loading, leading to deterioration in the engine performance and efficiency due to the issue of wet stacking. Diesel engine manufactures suggest a minimum load of about 0.4 p.u. to avoid this problem [23]. Therefore, an active power curtailment of the HKECS is desirable and necessary in order to mitigate the light loading condition on the diesel genset. Furthermore, the full-rated converter also decouples the generator frequency from the grid frequency. The disadvantage is that one tends to lose the inertia of the turbine-generator which can have a positive impact on the frequency regulation aspect of the microgrid during transient events [102]. A significant frequency reduction and a much-needed boost of diesel genset output power are expected during a large disturbance such as sudden increase in the load and/or decrease of water speed. The HKECS can release the kinetic energy stored in its rotating masses (e.g., blades, generator shaft, etc.) in order to support the grid frequency control. Moreover, these problems are magnified in storage-less D-HK microgrids where a conventional energy storage system is not available to mitigate power as well as frequency deviations by controlling active power [103].

Some studies have been done for the steady-state performance of a storage-less D-W/HK microgrid where the diesel engine runs at very low load due to a high level of wind/hydrokinetic power penetration [104], [105], [106], [60]. Using a dump load is an obvious solution to dissipate power generated by the HKECS and hence mitigate the low loading operation of the

diesel engine. However, given the cost and complexity of the hardware, and control system implementations, it is preferred to avoid its use if possible [104]. Reducing the HKECS output power is another solution [60]. It can be obtained by a blade pitch control and a generator speed control [67], [90]. The pitch regulated control is however not possible for most HKTs. This is the case for the cross-flow turbine considered in this thesis which has non-pitchable blades [27], [107]. On the other hand, generator speed control has been mostly used for the MPPT control [104], and there is little research on curtailing the WT/HKT output power with generator speed control in a storage-less D-HK to mitigate light loading condition of diesel genset.

Regarding transient conditions, recently, add-on controllers with the grid frequency feedback are introduced to the PMSG-based WECSs/HKECSs to support grid frequency control [108], [109], [110], [111], [112], [113]. The controllers include an inertial controller [108], [109], [110], a primary power vs. frequency droop controller (or primary frequency droop controller) [111], or a combination of both [111], [112], [113]. The turbine also operates at a deloading (DL) mode by moving the power tracking curve from the MPPT curve to the right sub-optimal curve to provide a sufficient power reserve margin for supporting the primary frequency droop control. In the majority of cases [108], [109], [110], [111], [112], the frequency support controllers are added to the power control loop of a cascaded outer power and inner current control loop. In [113], the frequency support controllers are added either into the inner current or the outer power loop. However, these controllers and their associated gains, e.g. inertial and frequency droop gains, are mainly intended to deal with transient conditions for a given wind/water speed. The selection of inertial and frequency droop gains has been not addressed considering the variable nature of the wind/water speed, resulting unreliable WECS/HKECS output power. In [108], [109], [110], [111], [112], the selected power electronics converter was a back-to-back 6-switch converter which is more complex and costly compared to a rectifier, a DC-DC boost converter, and a three-phase inverter, which is used in [113]. Moreover, the reference power of the MPPT/DL mode was estimated by sensing the generator rotor speed using a relatively expensive shaft encoder. The turbine frequency support control capability in a small-scale D-W microgrid was investigated by regulating the output voltage of the generator-side converter in [100]. However, this was implemented by a back-to-back 6-switch converter through a complicated multi-loop control scheme.

The purpose of this study is to develop a new supplementary frequency control loop for the HKECS to support grid frequency control during transient events as well as to provide an effective load power sharing between the HKECS and genset during the steady-state conditions. It includes inertial and frequency droop controllers which are added to the conventional control system of the HKECS. The output power of diesel genset operates based on a power vs. frequency droop curve to make a variable frequency system so that the HKECS can regulate its output power based on the grid frequency. The basic droop control can help with power sharing in the steady-state condition but its effect on the transient response, frequency nadir and rate of change of frequency (ROCOF)- $df/dt$ , is limited. By using the inertial controller, a better result is obtained. The proposed control strategy is realized with a single voltage loop control which the frequency support control scheme is added to the reference voltage. Selection and design of the frequency support control loop gains are discussed, and the effectiveness of the developed controller is verified experimentally with an electromechanical-based D-HK microgrid emulator.

## 5.2 Power and Frequency Control for a Storage-Less D-HK Microgrid

The schematic diagram of a generic storage-less D-HK microgrid used in this Chapter is shown in Figure 5.1. A diesel genset model includes two main parts, i.e., a prime mover (diesel engine) and an electrical generator (synchronous generator). In experimental work discussed in this Chapter, the synchronous generator is implemented with a 3.5 kW/220V/1800r/min/60Hz wound rotor synchronous generator (WRSG). The speed governor is a controller to regulate the speed of the diesel engine with a feedback of the actual shaft speed. The synchronous generator regulates the grid voltage with the automatic voltage regulator (AVR) while fulfilling the reactive power and voltage limitations (e.g.,  $1 \pm 5\%$  p.u) of the microgrid. More details of the diesel genset model used in this Chapter are discussed in [64]. The genset typically works as a master unit, balancing demand and supply. The HKECS provides a variable amount of active power and can be seen as a variable negative electrical load. In steady state conditions, the total generation  $P_{gen}$  including HKECS  $P_{HKECS}$  and genset  $P_{genset}$ , is equal to the total grid load,  $P_{load}$ , which includes the line losses. The dynamic relationship between power generation and demand can be represented by equation (5.1) from the swing equation [114].

$$P_{gen} - P_{load} \approx J_g f \frac{df}{dt} \approx \frac{dE_{kinetic}}{dt} \quad (5.1)$$

where  $E_{kinetic}$  is the kinetic energy stored in rotating machines that are directly connected to the grid,  $J_g$  is the total grid inertia,  $f$  is the grid frequency.

According to (5.1), a sudden mismatch in supply and demand will lead to a variation in the grid frequency. Usually, the master unit, the diesel genset, will react to active power mismatches so as to bring the frequency back to a stable and acceptable value. Since the adjustment in the mechanical input power of the diesel genset cannot be done instantaneously, the grid frequency will vary with a rate, called rate of change of frequency (*ROCOF* or  $\frac{df}{dt}$ ), and dictated mostly by the inertia connected to the shaft of the rotating machines connected to the grid. This is known as the inertial response of the system. Depending on the delays and gains in the speed/frequency loop of the diesel genset, the frequency will reach a minimum value called *frequency nadir*, and then bounce back towards the rated frequency, if the diesel genset operates in the isochronous mode. If the diesel genset works based on the droop frequency/speed control, the new steady-state frequency can be up to +/- 5% depending on the actual power demanded by the load.

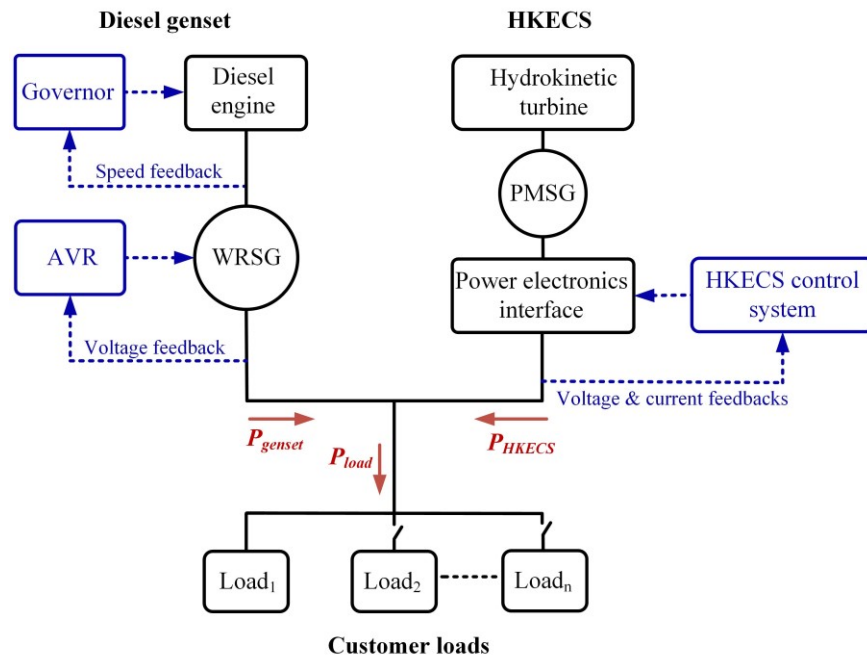


Figure 5.1 Schematic diagram of a generic storage-less D-HK microgrid.

Conventionally, HKTs operate in the MPPT mode to capture as much power as possible from the water flow. Hence, they do not participate in active power sharing with the genset and provide frequency support, where the converted hydrokinetic power should vary with grid frequency. However, with the appropriate controls, they have capabilities to provide the frequency support similar to diesel gensets, by actively regulating its output active power supplied to the grid [110], [115]. The HKECS can supply an additional power proportional to the grid frequency deviation ( $\Delta f$ ) and the derivative of grid frequency ( $\frac{df}{dt}$ ). During a disturbance e.g. load change, these components can decrease the imbalance between generation and demand by injecting/absorbing more power from the HKT to microgrid until the governor increase/decrease the mechanical power of the diesel genset. The additional power is provided by kinetic energy stored on the HKECS's rotating parts (e.g. blades, generator shaft, etc.), but it cannot guarantee beyond the transient period. Therefore, to provide an active power sharing in the steady-state (long-term), a power reserve is required. This reserve power can be obtained by operating the turbine in a deloaded (DL) mode. Controlling the turbine in the DL mode will be discussed in the next Section.

Moreover, the parallel operation control of the HKECS and genset in the microgrid can be obtained by centralized or decentralized control [116]. The former requires communication between generators, while the latter control is obtained without an explicit communications system by using power vs. frequency droop-based local controllers. This Chapter contributes towards the latter control. The power vs. frequency droop control allows a proportional load sharing among the generators. Let us assume that the HKECS output power changes linearly with the grid frequency, the relation between the grid frequency and output power of the genset and HKECS for a droop controlled mode are given as

$$P_{genset} = m_1 (f_1 - f) \quad (5.2)$$

$$P_{HKECS} = m_2 (f_2 - f) \quad (5.3)$$

where  $m_1$  and  $m_2$  are the slopes of the genset and HKECS droop curves (in kW/Hz), and  $f_1$  and  $f_2$  are the reference frequency (in Hz) of the genset and HKECS, respectively. These values can

be set so as to control how much power each source supplies at a given frequency.  $f_1$  usually sets to the no-load frequency of the genset while  $f_2$  can set to a different value based on the load sharing control strategy.

Considering a load variation for such system, the resulting frequency variation and genset output power variation can be given as [62].

$$\Delta f = \frac{\Delta P_{load}}{m_1 + m_2} \quad (5.4)$$

$$\Delta P_{genset} = \frac{m_1}{m_1 + m_2} \Delta P_{load} \quad (5.5)$$

According to equation (5.4) and (5.5), the HKECS (with a slope of  $m_2$ ) has a capability in reducing variation of the grid frequency as well as the genset output power for a given load change.

Therefore, the operation of HKECS in droop controlled provides an effective power sharing between generators in order to mitigate low-load running of the diesel generator in the steady state condition. Moreover, it also has a good effect on the transient response, e.g., frequency nadir and ROCOF as well.

### 5.3 HKECS Configuration and Operation

#### 5.3.1 HKECS Control Scheme

The schematic diagram for the HKECS used in this Chapter is shown in Figure 5.2. The output power and torque of a fixed-pitch cross-flow type HKT were introduced in the Section 2.1.1. The power electronics interface includes the generator-side converter (a three-phase diode bridge rectifier and a DC-DC boost converter) and grid-side converter (a three-phase inverter) with a common DC-link. Based on equation (2.34), the rotor speed of the PMSG/HKT ( $\omega_g / \omega_m$ ) can be regulated by adjusting the value of  $V_{dc}$ . This can be realized using the boost DC-DC converter. If  $V_{dc}$  can be controlled to track a given reference voltage, the power extracted by the

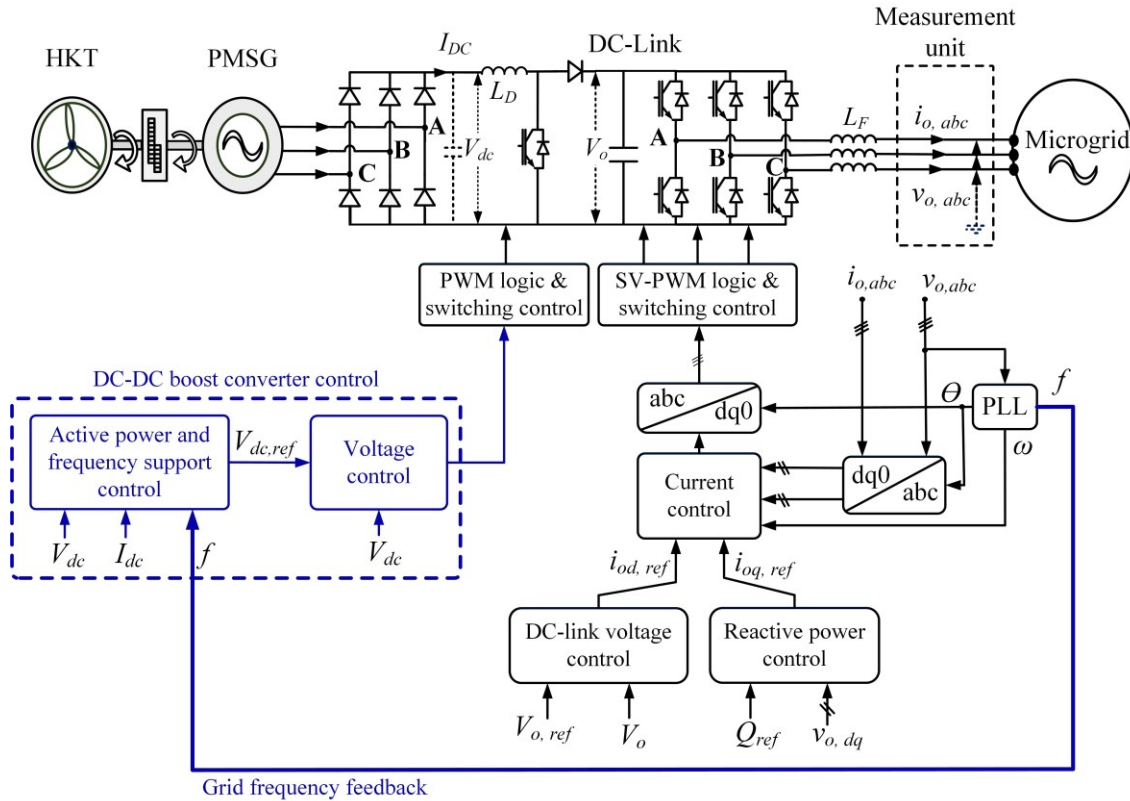


Figure 5.2 Block diagram of the HKECS.

HKT from the water flow can be controlled [55], [90]. The DC-DC boost converter control unit consists of an output diode rectifier voltage (rotor speed) control loop, and an active power and frequency support control loop. The design of the voltage control loop has been discussed in Chapters 2 and 3. This Chapter focuses on the design of the active power and the frequency support control loop, which will be discussed in Section 5.4.

The grid-side converter is a 6-switch inverter and is controlled so as to transfer the DC-link power into the grid, which is done by regulating the intermediate DC bus voltage. The grid-side inverter is designed to operate as a current-controlled voltage source inverter (CC-VSI). Its structure essentially involves two cascaded control loops. An inner current loop is responsible for regulating the inverter output current, and an outer DC-link voltage loop is used to balance the power flow into the intermediate DC bus. It should be able to regulate the DC-link voltage of the inverter regardless of the water speed variation. The reactive power control of the grid-side

converter can also be obtained by an outer reactive power loop. In the control loops, the output currents and grid voltages are converted from the  $abc$  frame to the  $dq$  frame using the Park transformation and a phase-locked loop (PLL) controller [51]. The PLL provides an accurate frequency and phase angle estimation of the grid voltage. The choice and parameter determination of the proportional-integral (PI)-type controllers and the PLL controller have been discussed in details in Section 2.1.5.1. In this Chapter, the grid-side converter is set to operate at unity power factor. The parameters of the HKECS are listed in Appendix A.

### 5.3.2 DL Operation Mode

To provide sufficient reserve power for supporting the frequency droop control, the HKT has to operate at a sub-optimal operating point, called DL operation mode [45]. For a fixed-pitch HKT and a given water speed, based on the turbine's power-rotor speed curve, the DL mode can be obtained by shifting the operating point towards the right side of the MPPT point (high-speed region), which leads to a power reduction on the HKT output power. Considering that the relationship between the generator/turbine rotor speed and the output voltage of diode rectifier is linear and given by equation (2.34), the available power at the DL mode operation can be calculated as

$$P_{HKT, DL} = \left(1 - \frac{\%DL}{100}\right)P_{HKT, MPPT} \quad (5.6)$$

where  $\%DL$  is DL percentage and

$$P_{HKT, MPPT} = K_{opt}V_{dc}^3 \quad (5.7)$$

$K_{opt}$  is the optimal coefficient and can be determined as

$$K_{opt} = \frac{0.5A\rho R^3 K_V'^3 C_{P,max}}{\lambda_{opt}^3} \quad (5.8)$$

where  $K_V'$  is the voltage constant.  $K_{opt}$  can also be obtained by an optimal power algorithm through off-line tests or simulations on the HKT, generator, and diode rectifier [107]. The

reserve power at a  $DL$  percentage can also be determined as

$$P_{reserve} = P_{HKT,max} - P_{DL} = \left(\frac{\%DL}{100}\right)P_{HKT,max} \quad (5.9)$$

In equation (5.6) and (5.9), %DL can vary between 0 and  $DL_{max}$ , where  $DL_{max}$  is the maximum acceptable DL percentage of the turbine and is a user-defined value. For example, when  $DL_{max}$  is set at 15%, %DL changes between zero and 15,  $P_{DL}$  varies between  $P_{HKT, MPPT}$  and  $0.85P_{HKT, MPPT}$ , and  $P_{reserve}$  changes between 0 and  $0.15 P_{HKT, MPPT}$ , respectively.

Figure 5.3 shows the power vs. output voltage of the diode rectifier for various water speeds for the HKT. It is assumed that the power losses are ignored,  $P_{dc}$  is equal to  $P_{HKT}$ . One can see that the maximum turbine power across different water speeds follows an MPPT curve, line “A-B”, which is corresponding to %DL= 0 in equation (5.6). When the turbine is deloaded to  $DL_{max}$ , the turbine power across various water speeds follows a  $DL_{max}$  curve, line “C-D”. These curves can be realized using look-up tables ( $P_{dc}$  vs.  $V_{dc}$ ). Also, for a given water speed e.g. 2.8 m/s, one can see that the turbine power varies between  $P_{HKT, MPPT}$  (point B) and  $P_{HKT, DLmax}$  (point D), where  $P_{HKT, DLmax}$  is the turbine power at  $DL_{max}$ . This can be obtained by changing  $V_{dc}$  between  $V_{dc, MPPT}$  and  $V_{dc, DLmax}$ , where  $V_{dc, DLmax}$  is the output voltage of the diode rectifier at  $DL_{max}$ , without using any mechanical sensors for water speed and rotor speed measurements. Moreover, it is assumed that there is a linear relationship between  $V_{dc}$  and  $P_{dc}$  in the DL mode (e.g., line “B-D”). It should be noted that as the turbine operates at a rotor speed higher than in the usual working condition (MPPT), the kinetic energy stored into the rotating shaft turbine will increase with the square of the rotor speed increase [113]. This kinetic energy can be released into the grid to support frequency control.

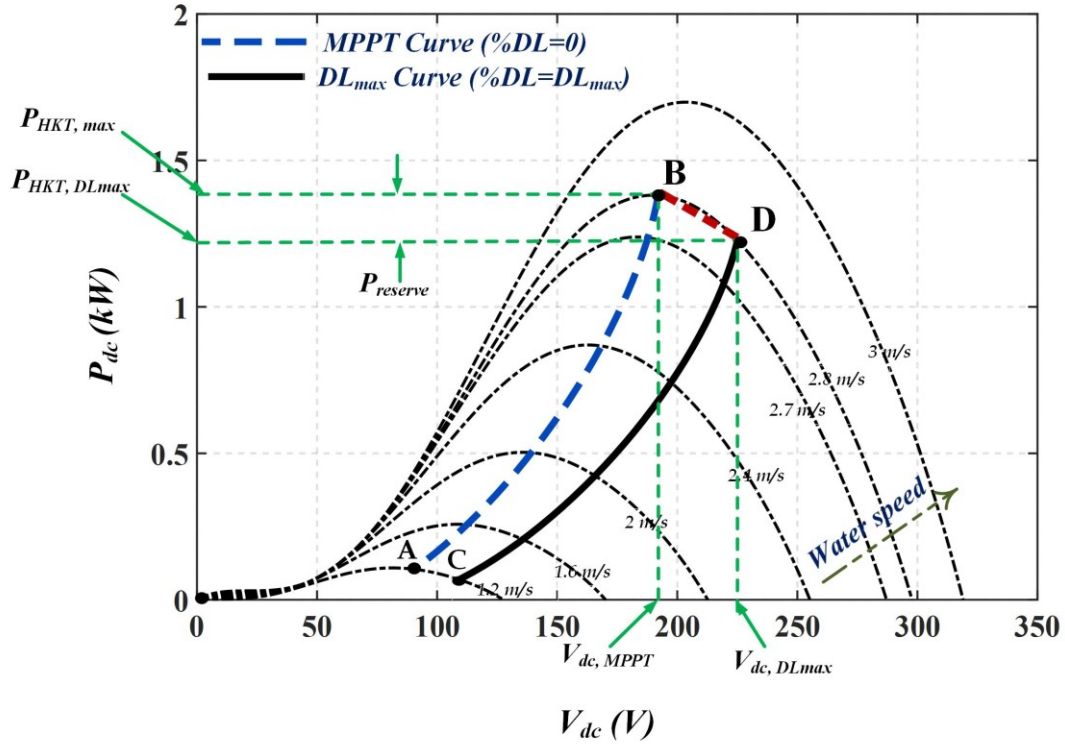


Figure 5.3 Power vs. output voltage of the diode rectifier for various water speeds and MPPT and DL Curves

#### 5.4 Proposed Frequency Support Control Scheme of the HKECS

As discussed in the previous Section, the grid-side converter is in charge of regulating the DC-link voltage while controlling the power factor of the HKECS. So, active power control of the HKECS can only be done through the DC-DC boost converter which is placed between the uncontrollable diode rectifier and the grid-side converter. Active power control of the HKECS in the MPPT mode has been obtained by a single control loop, diode rectifier output voltage control loop, which adjusts the duty cycle of the boost converter [55], [90]. In the following subsections, the inertial and droop control as add-on controllers will be introduced to this diode output voltage control loop in order to provide the frequency support control of a storage-less D-HK microgrid for both transient and steady-state conditions. Moreover, a brief discussion on the selection and design of the frequency loop gains will be explained.

### 5.4.1 Frequency Support Control Scheme of the HKECS Using the Boost DC-DC Converter

Figure 5.4 shows the block diagram of the proposed control scheme for the DC-DC boost converter. Without frequency support control (conventional control scheme),  $V_{dc, ref}$  can be generated by the MPPT tracking curve as shown in Figure 5.3.  $V_{dc}$  is controlled by a voltage regulator using a proportional-integral (PI) controller. Then, the voltage regulator generates the duty cycle ( $D$ ) of the DC-DC boost converter. With the frequency support control scheme, supplementary terms including the frequency droop control  $\Delta v_{dc,d}$  and the inertial control  $\Delta v_{dc,i}$  are added into the controller as given by equation (5.10) and (5.11).

$$\Delta V_{dc,d} = K_d(f - f_{ref}) \quad , \quad f \geq f_{ref} \quad (5.10)$$

$$\Delta v_{dc,i} = K_i \frac{df}{dt} \quad (5.11)$$

where  $K_d$  and  $K_i$  are the gains of the frequency droop control and the inertial control loops, respectively.  $f_{ref}$  is the reference frequency of frequency droop control.  $f_{ref}$  is set to the genset full-load frequency  $f_{fl}$ , which corresponds to 100% loading of the genset. Also, the derivative of a noisy high-frequency signal will intensify the effect of that noise which leads to a failure of the controller performance. To prevent this issue, the derivative term can be represented by a high-pass filter as shown in Figure 5.4. The time constant "T" should be selected small related to the main time constant of the system in order to detect  $\frac{df}{dt}$  of the grid frequency accurately. The time constant "T" is set to 0.08 s which is smaller than the main time constant of the system used this work ( $\approx 1$ s).

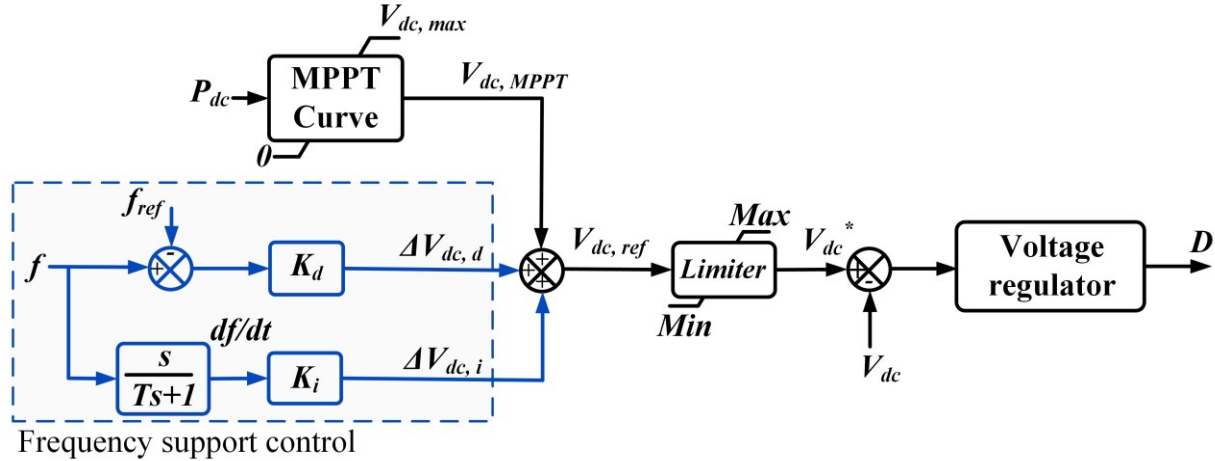


Figure 5.4 DC-DC boost converter with frequency support control.

From equation (5.10),  $V_{dc}$  changes according to the grid frequency deviation from a reference frequency value  $f_{ref}$ . This term allows the HKECS to change the turbine operating point between MPPT and  $DL_{max}$  according to grid frequency. During the steady-state period,  $\frac{df}{dt}$  is very small and can be ignored. Hence,  $V_{dc,ref}$  is  $K_d(f - f_{ref}) + V_{dc,MPPT}$ . Since the genset works with droop speed control, a load change will result in a frequency change. By having the HKECS operating with frequency droop, the HKT power will not be as high as if the HKT was operating in MPPT and operating point will change too. The operating point changes according to setting value of  $K_d$  which will be explained in the next sub-Section. Basically, this parameter is chosen so that the HKT operating point moves from the MPPT point towards the  $DL_{max}$  point when the grid frequency increases due to a decrease in the load power. Hence, the power supplied by the HKECS into the grid reduces and mitigates the light loading operation of the diesel genset. Moreover, the reserve power provided by the DL operation mode is increased leading to reserve more kinetic energy on the rotating masses which can be released into the grid for supporting frequency control during the transient period. Conversely, the turbine operating point moves towards the MPPT point when the grid frequency decreases due to an increase in the load power. This can help to maximize hydro resource utilization and reduce diesel engine's fuel consumption, although less energy for the inertial control can be obtained.

Following a disturbance, the inertial control aims to decrease the ROCOF compared to the case when only the frequency droop control is used. For example, within the initial stage of an under-frequency event, the value of ROCOF is largely negative, so  $\Delta v_{dc,i}$  is largely negative too. Therefore, the turbine rotor speed decreases faster, releasing more of the kinetic energy stored in the rotating masses into the grid within a shorter period. This results in a lower ROCOF compared to using only the frequency droop control.

#### 5.4.2 Selection of the Frequency Loop Gains

To provide a high contribution of the HKECS to support the grid frequency control, large values of  $K_i$  and  $K_d$  are desirable [117]. However, substantial gains can take the HKT to the stall region (unusable region) or exceed voltage/current rating of the PMSG and converters. This is because the operating point of the HKT changes with water speed variations, and hence the stored kinetic energy on the rotating parts and the reserve power provided by the DL operation of the turbine change. These problems can be solved by setting  $K_i$  and  $K_d$  according to the HKT operating point. Moreover, the minimum value of the reference signal of the voltage control loop is set to  $V_{dc, MPPT}$  to avoid the HKT operation in the stall region.

The frequency droop control gain  $K_d$  is selected by the following equation.

$$K_d = K_{d0} \frac{V_{dc, MPPT}}{V_{dc, MPPT, max}} \quad (5.12)$$

where  $K_{d0}$  is the droop gain-tuning factor and is a constant value.  $K_{d0}$  is set according to  $DL_{max}$  for  $v_{T, max}$ , where  $v_{T, max}$  is the maximum allowable water speed. It is set so that the HKT operates at  $DL_{max}$  as grid frequency reaches  $f_{ml}$ .  $f_{ml}$  corresponds to the minimum diesel engine loading (40% of rated value) according to the droop speed control on the diesel genset. At  $v_{T, max}$ ,  $V_{dc, MPPT}$  is equal to  $V_{dc, MPPT, max}$  and hence  $K_d = K_{d0}$ . However, the HKT operation point may go beyond their corresponding  $DL_{max}$  point if a fixed value of  $K_d$  is selected for water speeds lower than  $v_{T, max}$ . Hence,  $K_d$  is automatically decreased by factor  $\frac{V_{dc, MPPT}}{V_{dc, MPPT, max}}$  in equation (5.12), which  $V_{dc, MPPT, max}$  is more than  $V_{dc, MPPT}$  for water speeds lower than  $v_{T, max}$ .

Table 5.1 shows variations of the HKECS output power and the output voltage of the diode rectifier with grid frequency for three different water speeds,  $v_T = [1.8 \text{ m/s}, 2.4 \text{ m/s}, 2.8 \text{ m/s}]$ , while  $K_i = 0$  and  $DL_{max} = 25\%$ . The results were obtained based on the simulation for the steady-state conditions. The rated power of the diesel genset is 3.5 kW, and it operates with droop speed control with a slope ( $m_1$ ) of 1.076 Hz/kW.  $f_{ml}$  and the corresponding minimum loading of the diesel genset  $P_{genset, min}$  are calculated as 60.7 Hz and 1.4 kW, respectively. According to the procedure mentioned above,  $K_{d0}$  and  $f_{fl}$  are selected as 24 V/Hz and 58.44 Hz, respectively. One can see that when the grid frequency moves towards its lowest value ( $f_{fl}$ ), the HKT moves towards the MPPT point as well as  $\Delta V_{dc,d}$  to zero, what is automatically done by decreasing factor  $(f - f_{fl})$  in equation (5.10). As a result, the genset's output power decreases. On the other hand, when the grid frequency moves towards  $f_{ml}$ , HKT moves towards the  $DL_{max}$  point, resulting in reducing the output power of HKECS and increasing the genset's output power. The power vs. frequency results of the HKECS from Table 5.1, and power vs. frequency plot of the genset are shown together in Figure 5.5. One can observe that HKECS presents different power-frequency droop characteristics while the water speed changes. At higher water speeds (e.g., 2.8 m/s), the variation of HKECS output power with grid frequency change is more than low water speeds (e.g., 1.6 m/s). Therefore, the HKECS contributes more to share the load with the genset at higher water speeds than lower water speeds.

Table 5.1 Variation of the HKECS output power and output voltage of the diode rectifier with grid frequency for three different water speeds,  $v_T = [1.6 \text{ m/s}, 2.4 \text{ m/s}, 2.8 \text{ m/s}]$ , while  $K_i = 0$  ( $\Delta v_{dc,i} = 0$ ),  $K_d = 24$ , and  $DL_{max} = 25\%$ .

$f$	$v_T = 2.8 \text{ m/s}$			$v_T = 2.4 \text{ m/s}$			$v_T = 1.6 \text{ m/s}$		
	$\Delta V_{dc,d} = K_d(f - f_{ref})$ (V)	$V_{dc,ref}$ (V)	$P_{HKECS}$ (kW)	$\Delta V_{dc,d} = K_d(f - f_{ref})$ (V)	$V_{dc,ref}$ (V)	$P_{HKECS}$ (kW)	$\Delta V_{dc,d} = K_d(f - f_{ref})$ (V)	$V_{dc,ref}$ (V)	$P_{HKECS}$ (kW)
60.7 ( $f_{ml}$ )	54.24	244.24	1.038	46.64	208.64	0.630	31.45	142.45	0.178
60.2	42.24	232.24	1.141	36.32	198.32	0.712	24.49	135.49	0.208
59.7	30.24	220.24	1.257	26	188	0.778	17.53	128.53	0.229
59.2	18.24	208.24	1.330	15.68	177.68	0.835	10.57	121.57	0.240
58.8	8.64	198.64	1.369	7.43	169.43	0.859	5.01	116.01	0.255
58.44 ( $f_{fl}$ )	0	190	1.385	0	162	0.870	0	111	0.257

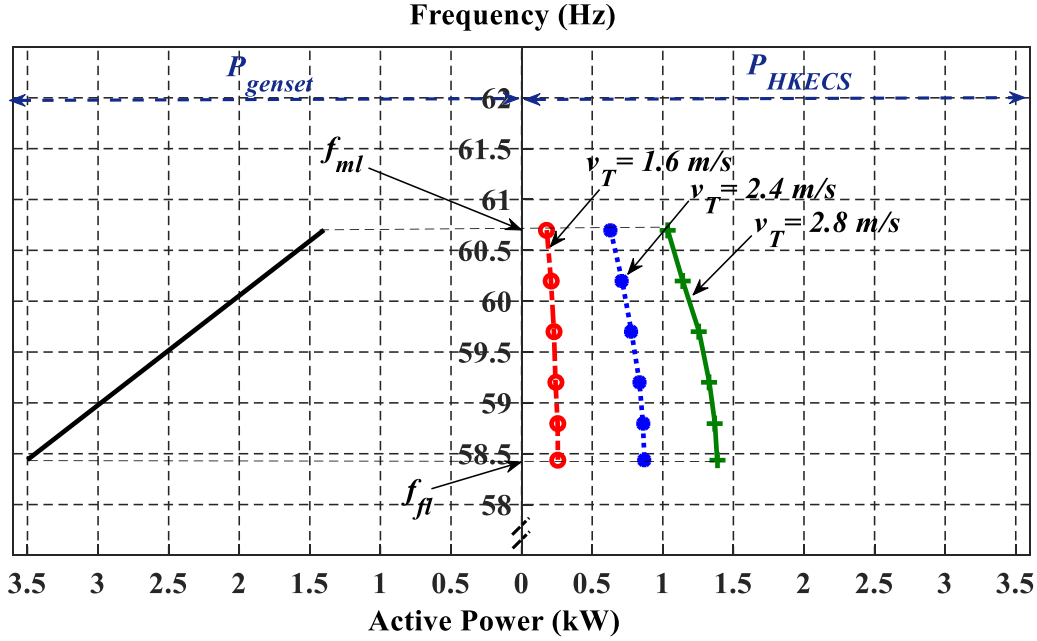


Figure 5.5 Variations of the HKECS and genset output power with grid frequency for three different water speeds ,  $v_T = [1.6 \text{ m/s}, 2.4 \text{ m/s}, 2.8 \text{ m/s}]$ , while  $K_i=0$  ( $\Delta v_{dc,i} = 0$ ),  $K_d=24$  and  $DL_{max}=25\%$ .

The inertial control gain  $K_i$  is selected based on the largest credible load change and releasable kinetic energy (KE) stored in the rotating masses of the HKECS into the microgrid. The releasable KE for an HKECS from rotating masses can be given as

$$\Delta E_{HKT} = J(\omega_m^2 - \omega_{m,MPPT}^2) \quad (5.13)$$

Substituting equation (2.34) into equation (5.13), equation (5.14) can be obtained.

$$\Delta E_{HKT} = \frac{J}{K_V^2} (V_{dc}^2 - V_{dc, MPPT}^2) \quad (5.14)$$

From equation (5.1), (5.11), and (5.14),  $K_i$  can be considered proportional to the releasable KE with a reasonable assumption. Also, the maximum releasable KE is obtained when  $V_{dc}$  changes from  $V_{dc, DLmax}$  to  $V_{dc, MPPT}$  [118]. Moreover, a larger  $K_i$  implies more releasable KE and more contribution to the reduction of the ROCOF than that of a smaller  $K_i$ . However, since frequency droop provides a variable DL operation for the HKT and considering water speed

variations, choosing a constant  $K_i$  cannot be considered as an effective method. So,  $K_i$  is selected by the following equation.

$$K_i = K_{i0} \frac{V_{dc}^2 - V_{dc, MPPT}^2}{V_{dc, MPPT, max}^2} \quad (5.15)$$

where  $K_{i0}$  is the inertial gain-tuning factor and is a constant value. In order to set  $K_{i0}$ , the value of  $K_i$  should be estimated so that  $K_i$  becomes the largest possible value for the HKT to release the maximum KE into the grid at  $v_{T, max}$ . This can be obtained by running simulation tests on the D-HK microgrid for to a step-up load change while both generators operate with the droop frequency control. Then,  $K_{i0}$  is calculated by replacing  $K_i$  in equation (5.15) for given  $V_{dc}$  values corresponding to  $DL_{max}$  and MPPT points. According to the above procedure,  $K_i$  is obtained as 40 V.s/Hz, and  $K_{i0}$  is calculated as 60 V.s/Hz for a 30% step-up load change.

From equation (5.15) for a constant water speed,  $K_i$  automatically decreases to zero as the operating point moves from the  $DL_{max}$  point to the MPPT point, by reducing factor of  $(V_{dc}^2 - V_{dc, MPPT}^2)$  in equation (5.15). Also, for water speeds lower than  $v_{T, max}$ ,  $K_i$  is automatically decreased by factor  $V_{dc, MPPT, max}^2$  in equation (5.15), which is more than  $V_{dc, MPPT}^2$  for each water speed. This avoids the problem of very large gains taking the HKT to the stall region (unusable region) at low water speeds. Figure 5.6 (a) and (b) show the simulation results of the grid frequency, output voltage of diode rectifier and HKECS output power response to a 30% step-up load change for two water speeds,  $v_T = [2.4\text{m/s}, 2.8\text{m/s}]$ , while  $K_{d0}$  and  $DL_{max}$  are set 24 and 25%. For both water speeds, the results are shown for  $K_{i0} = 0$  (without  $K_{i0}$ ),  $K_i = 40$  V.s/Hz (fixed value), and  $K_i$  selected based on equation (5.15). Setting  $K_i$  based on equation (5.15), it can be observed that the transient frequency response of the grid regarding ROCOF and *frequency nadir* is improved in both water speeds. However, the improvement of these terms at  $v_T = 2.8$  m/s is more evident than  $v_T = 2.4$  m/s. This is because the value of  $K_i$  is decreased based on equation (5.15) due to moving of turbine operating point towards the MPPT point and reducing the water speed. Also,  $V_{dc}$  is decreased to  $V_{dc, MPPT}$ , as expected based on the above discussion. For  $K_i = 40$  V.s/Hz (fixed value), the transient frequency response of the grid regarding ROCOF and *frequency nadir* at  $v_T = 2.8$  m/s is the same as that  $K_i$  selected based on

equation (5.15). However, as shown in Figure 5.6 (b). (ii) and (iii), one can observe that the HKT is taken to the stall region after the load change at  $v_T = 2.4$  m/s due to a large value of  $K_i$ . The HKECS output power and the output voltage of diode rectifier are fallen to around zero. Also, the grid frequency dips to around 57 Hz, as shown in Figure 5.6 (b). (i).

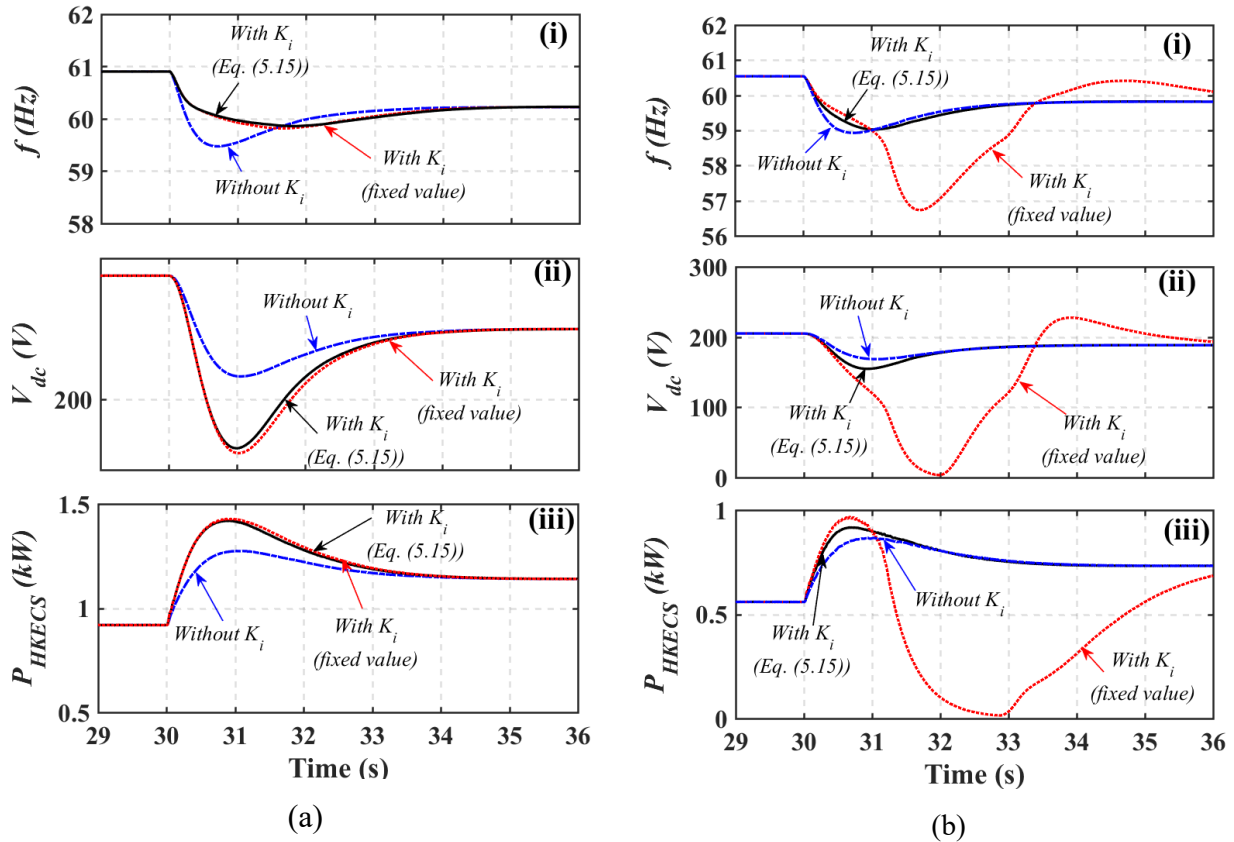


Figure 5.6 System response to a 30% step load change while  $K_{d0} = 25$  and  $DL_{max} = 25\%$ ; (a) grid frequency (i), output voltage of diode rectifier (ii), output power of HKECS(iii) for  $v_T = 2.8$ m/s, (b) grid frequency (i), output voltage of diode rectifier (ii), output power of HKECS (iii) for  $v_T = 2.4$ m/s.

## 5.5 Experimental Results and Discussions

### 5.5.1 D-HK Microgrid Emulator as Experimental Test-bed

An experimental set-up was assembled in the laboratory to assess the performance of the proposed frequency support control scheme for the storage-less D-HK microgrid. Figure 5.7 shows the block diagram of the storage-less D-HK microgrid emulator including the HKT and

diesel engine emulators. The development and application of the diesel genset and HKT/wind turbine emulator have been discussed in [25], [60], [64], [90]. The HKT emulator was based on a DC motor, whose torque is controlled through its armature current. This is achieved with a DC-DC buck converter operating with hysteresis current control (HCC) and fed from the AC grid through a three-phase diode rectifier. The reference signal for the HCC comes from the model (torque vs. shaft speed) of the cross-flow HKT. More details on HKT emulator are given in [90]. The diesel engine of the genset is emulated by a separately excited DC motor. Its rotor speed is controlled by an ABB DCS800 motor drive. The model of the HKT and diesel engine are implemented in a dSPACE DS1103 rapid control prototyping system. This system is also used as an interface between the ABB drive hardware, ABB control desk, and Matlab/Simulink to provide feedback signals. Figure 5.8 shows a picture of the complete system implemented in the laboratory. A power electronics interface including diode rectifier, DC-DC boost converter and three-phase inverter connected to a step-up transformer is used to connect the PMSG to the AC microgrid. The parameters of the experimental setup are listed in Appendix A. The results shown in the following sub-Sections are obtained with the Yokogawa SL1000 data acquisition system with a sampling period of  $20 \mu s$ . For demonstrating the performance of the proposed frequency support controller, the HKECS output power, genset output power, PMSG rotor speed, and grid frequency are illustrated through different scenarios in the following Sections. In all scenarios, the diesel genset is supposed to be operating in parallel with the HKECS. The CC-VSI of the HKECS works with unity power factor ( $Q_{ref} = 0$ ) while the local AC load presents power factor of 0.98 lagging. The HKECS is assumed to be operating up to 25% DL mode from the MPPT point during tests while working based on the proposed frequency support control loops.

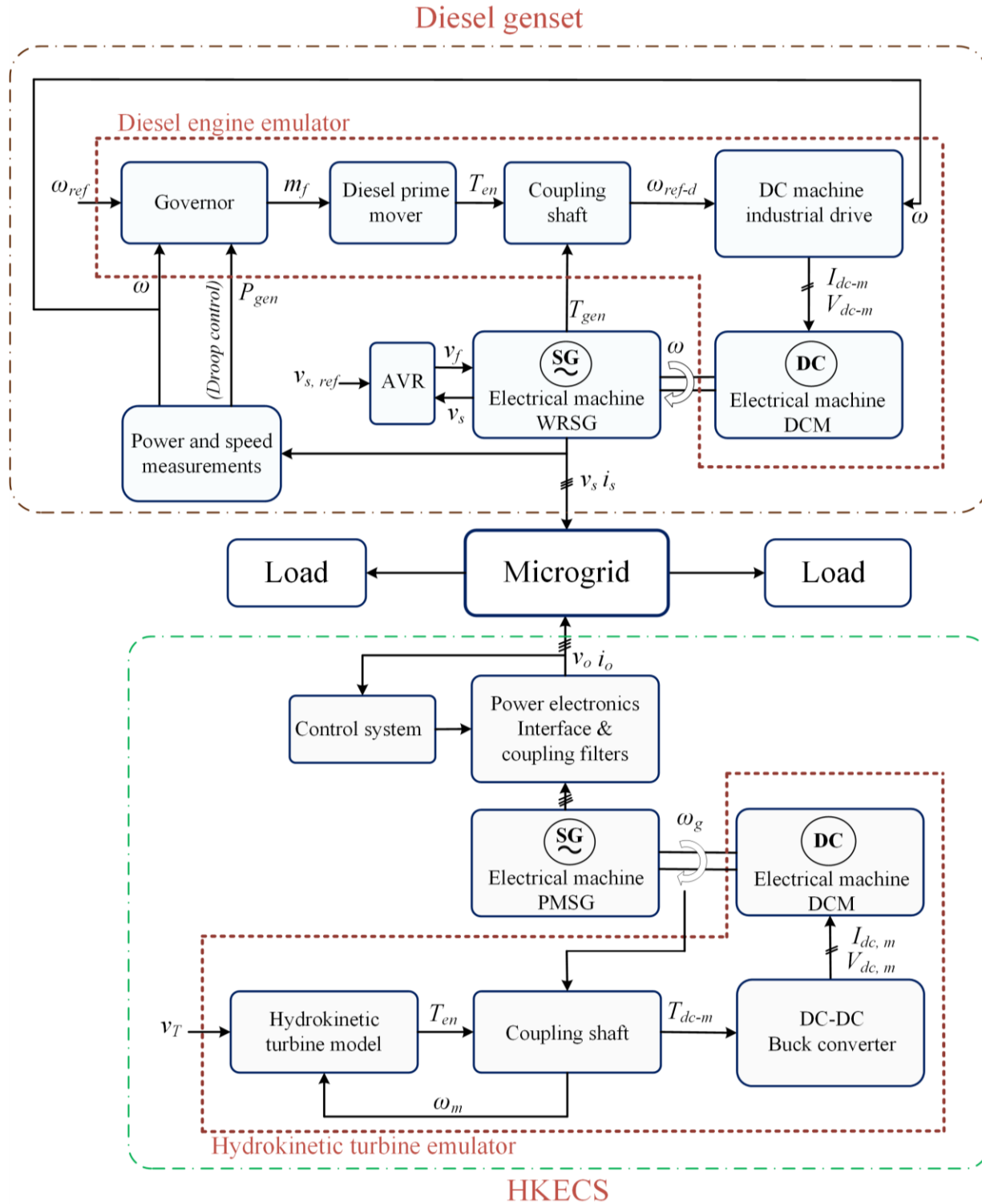


Figure 5.7 The block diagram of the storage-less D-HK microgrid emulator.

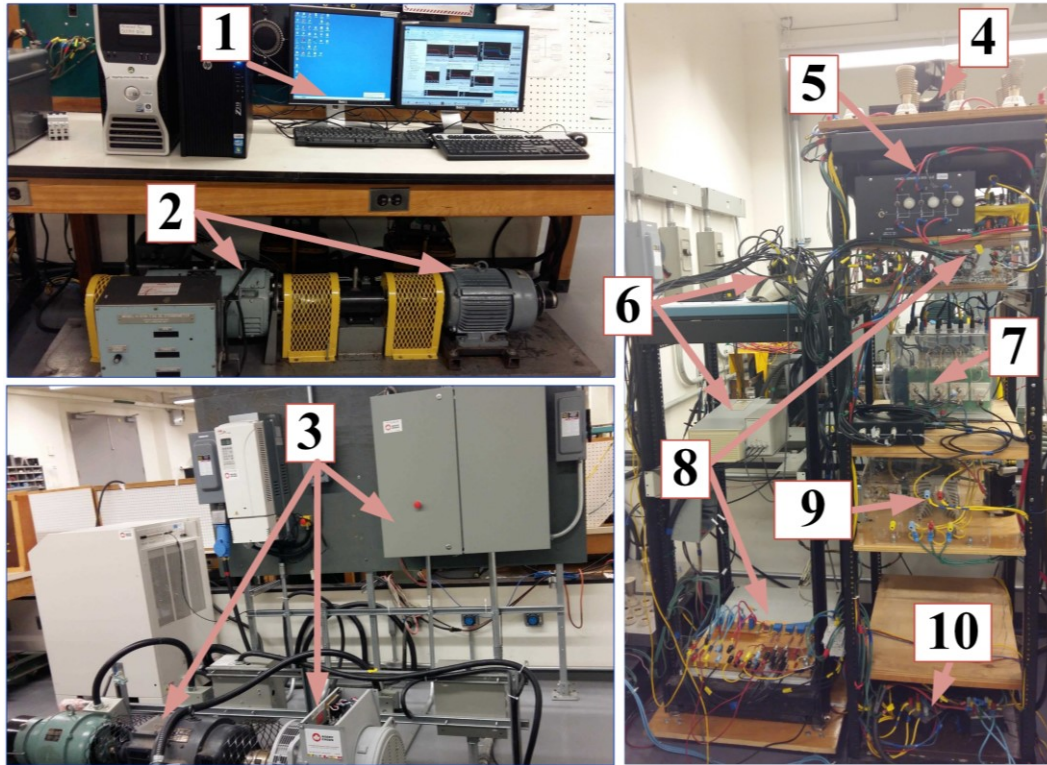


Figure 5.8 Hardware of experimental setup for a D-HK microgrid emulator; 1. dSPACE and ABB drive control desk, 2. DC motor and PMSG, 3. industrial ABB drive, wound rotor synchronous generator and DC motor, 4. AC and DC loads, 5. Synchronization device, 6. dSPACE interface hardware, 7. diode rectifier, DC-DC boost converter, and inverter, 8. current and voltage sensors, 9. DC-DC buck converter, 10. coupling filters and transformers.

### 5.5.2 Response to a Step Load Variation

This test concerns the system response before and after a step increment in the load. The initial load is 2.22 kW and then changes to 2.9 kW (30% step-up load change). Three cases are considered in this part. In all cases, the water speed is kept constant at 2.4 m/s during the test time. In case I, the HKECS operates in the MPPT mode. In case II, the HKECS operates with the proposed controller but with the inertial control loop disabled ( $K_i = 0$ ). In case III, the HKECS operates with both proposed frequency droop and inertial control loops.

Figure 5.9 shows waveforms of interest for case I. In all periods of the test, one can see that the HKECS operates in MPPT mode and does not participate in the frequency control and active power load sharing.  $P_{HKECS}$ ,  $V_{dc}$ ,  $\omega_g$ ,  $C_p$ , and  $V_o$  are kept constant at 0.95 kW, 160 V, 100 rad/s, 3.1, and 280 V, respectively. Before the load increment, the frequency is 60.9 Hz, and the genset

generates 1.27 kW. One can see that the diesel genset operates under the light loading condition as the grid frequency is higher than the minimum frequency  $f_{ml}$  (60.7 Hz) and the diesel genset output power is less than the minimum loading of the diesel genset  $P_{genset, min}$  (1.4 kW, 40% of rated value) After the load increment, the grid frequency drops to a minimum of 58.7 Hz after 0.9 s, then it increases to a steady-state value of 60 Hz and the genset delivers 1.95 kW power to the grid. The *frequency nadir* and ROCOF are measured as 2.2 Hz and 2.44 Hz/s following the load step increase.

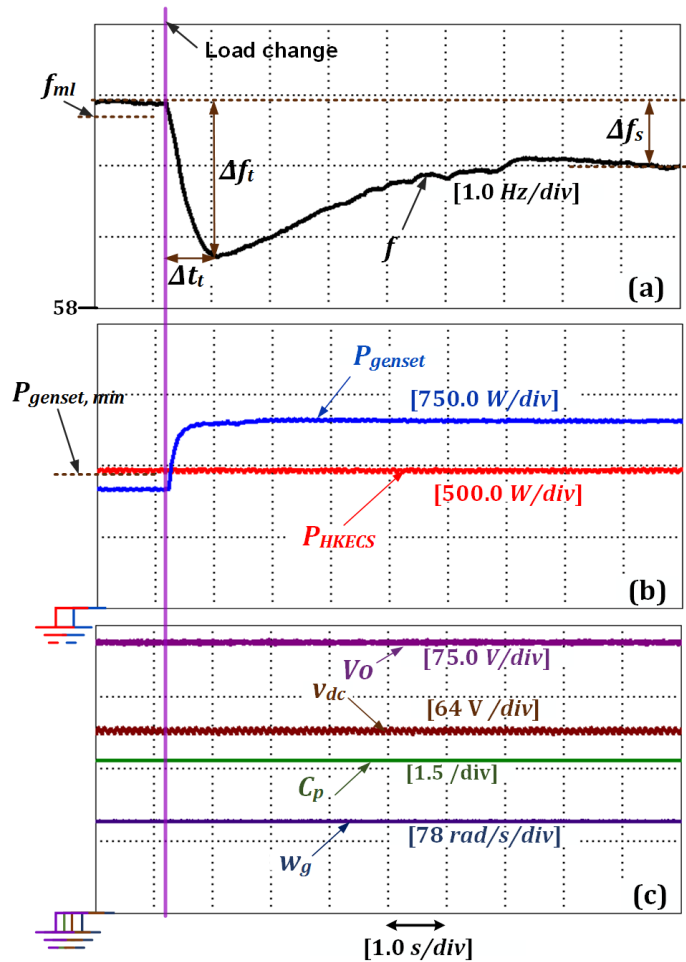


Figure 5.9 The system response for case I. The HKECS operates in MPPT mode. (a) grid frequency  $f$ , (b) HKECS output active power  $P_{HKECS}$  and genset output active power  $P_{genset}$ , and (c) inverter DC-link voltage  $V_O$ , diode rectifier output voltage  $V_{dc}$ , turbine power coefficient  $C_p$ , and generator rotor speed  $\omega_g$ .

Figure 5.10 shows waveforms of interest for case II. Before the load increment, the frequency is 60.55 Hz, and the genset generates 1.57 kW. One can observe that the HKECS output power is curtailed according to the DL operation mode compared to Case I and it generates 0.65 kW.  $V_{dc}$ ,  $\omega_g$ ,  $C_p$ , and  $V_o$  are 195 V, 124 rad/s, 2.6, and 280 V, respectively. One can see that the genset operates above the light loading condition as the grid frequency is lower than  $f_{ml}$  (60.7 Hz) and/or  $P_{genset}$  is higher than  $P_{genset, min}$  (1.4 kW). After the load increment, the frequency drops to a minimum of 58.8 Hz after 0.8 s, then it increases to a steady-state value of 59.8 Hz, and the genset generates 2.13 kW. One can see that as the frequency decreases, the HKECS increases its output power to support frequency control and active sharing during both the transient and steady-state conditions. Its output power increases to 0.9 kW and then decreased to 0.77 kW in the steady-state condition. The *frequency nadir* and ROCOF are measured as 1.75 Hz and 2.1 Hz/s during the transient condition.  $V_{dc}$  and  $\omega_g$  changes according to the frequency droop control. They decrease during the transient temporarily to 172 V, 105 rad/s, then they become stable at 185 V and 113 rad/s. After the load change,  $C_p$  increases to 0.3, then decreases to 0.285, which is more than before the load increment. This means that the contribution of the HKECS in power sharing between generators in the microgrid is increased with an increase in the load power. The HKECS produces more power due to higher power demand.

Figure 5.11 shows the system performance for case III. One can see that the steady-state performance is similar to case II, yielding expected results. However, the transient performance of the system, regarding *frequency nadir* and ROCOF is significantly improved when using both inertial and frequency droop control loops. The frequency nadir and ROCOF are measured as 1.6 Hz and 1.4 Hz/s during the transient condition. One can see that the HKECS contributes to the frequency support control more than in case II.  $V_{dc}$ ,  $\omega_g$ , and  $C_p$  are decreased to 166 V, 100 rad/s, and 3.1 respectively, which correspond to the MPPT operation point.

In both case I and case II, The HKECS can keep the inverter DC-link voltage constant at 280 V while providing the grid frequency control support as shown in Figure 5.10 (d) and Figure 5.11 (d).

Table 5.2 shows a summary of the system response for Case I, Case II, and Case III results.

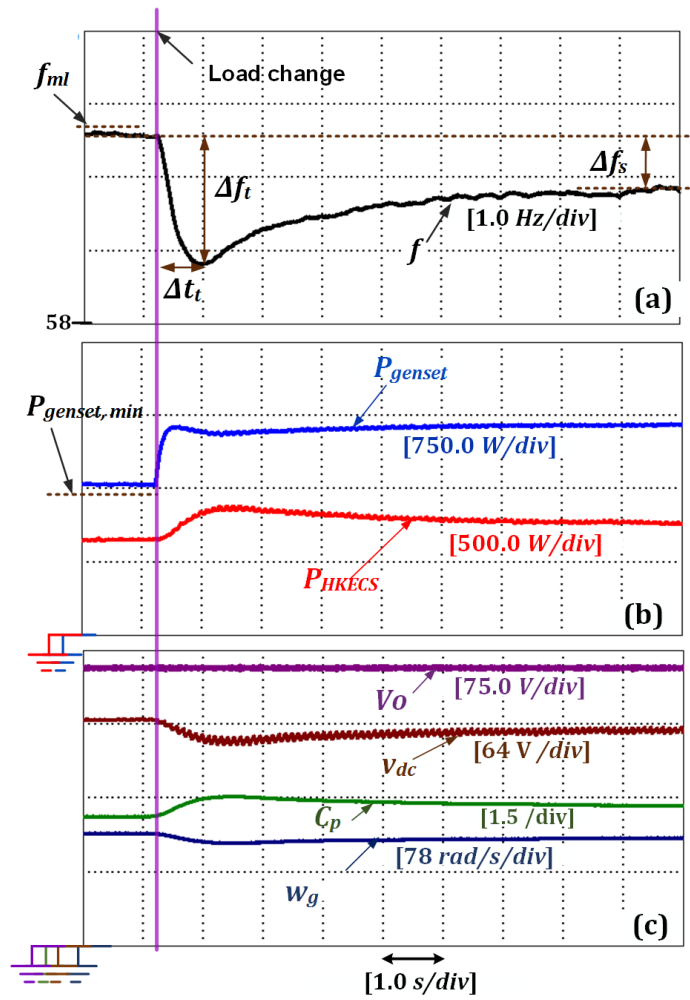


Figure 5.10 The system response for case II. The HKECS operates with proposed frequency support control while  $K_i = 0$  during the test. (a) grid frequency  $f$ , (b) HKECS output active power  $P_{HKECS}$  and diesel genset output active power  $P_{genset}$ , and (c) inverter DC-link voltage  $V_0$ , diode rectifier output voltage  $V_{dc}$ , turbine power coefficient  $C_p$ , and generator rotor speed  $\omega_g$ .

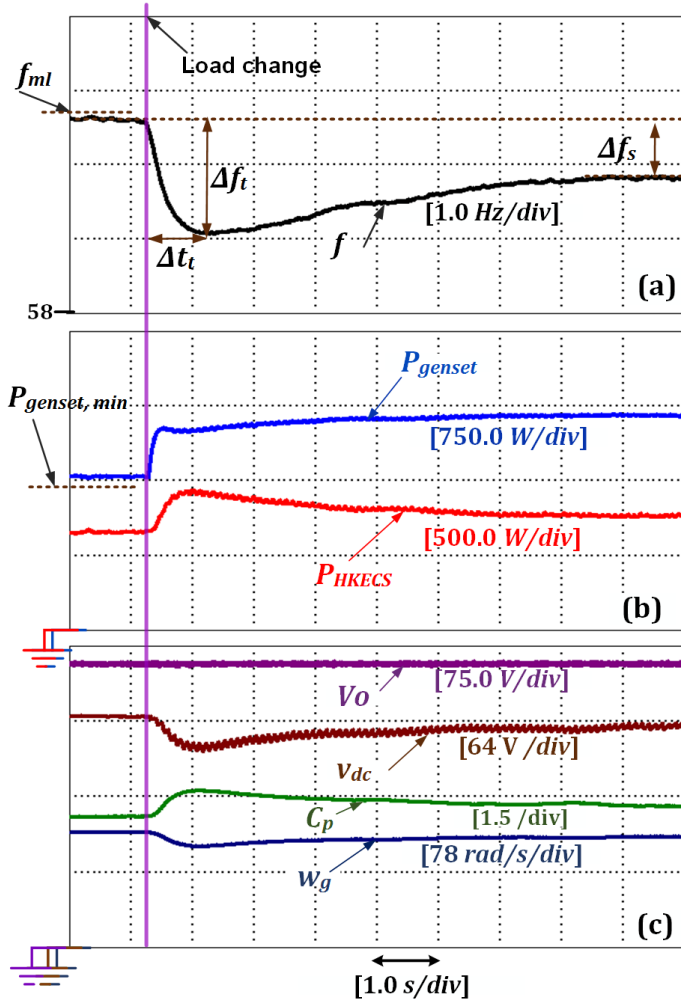


Figure 5.11 The system response for case III. The HKECS operates with proposed frequency support control loops. (a) grid frequency  $f$ , (b) HKECS output active power  $P_{HKECS}$  and diesel genset output active power  $P_{genset}$ , and (c) inverter DC-link voltage  $V_o$ , diode rectifier output voltage  $V_{dc}$ , turbine power coefficient  $C_p$ , and generator rotor speed  $\omega_g$ .

Table 5.2 Summary of the system response for Case I, Case II, and Case III results for a 30% step-up load change.  $f_s$  is the steady-state value of the grid frequency.

Case No.	Frequency nadir ( $\Delta f_t$ ) (Hz)	ROCOF ( $\Delta f_t / \Delta t_t$ ) (Hz/s)	Steady-state values before the load change			Steady-state values after the load change		
			$f_s$ (Hz)	$P_{genset}$ (kW)	$P_{HKECS}$ (kW)	$f_s$ (Hz)	$P_{genset}$ (kW)	$P_{HKECS}$ (kW)
Case I	2.2	2.44	60.9	1.27	0.95	60	1.95	0.95
Case II	1.75	2.1	60.7	1.57	0.65	59.8	2.13	0.77
Case III	1.6	1.4	60.7	1.57	0.65	59.8	2.13	0.77

### **5.5.3 Response to a Water Speed Variation**

This part is performed to evaluate the system response during water speed variations while the HKECS is equipped with the proposed frequency support control. The water speed changes in the shape of a trapezium as shown in Figure 5.12 while the load is considered to be constant at 2.9 kW during the test. Figure 5.13 and Figure 5.14 show key waveforms of the system response while the HKECS operates in the MPPT mode and with the proposed frequency support control loops, respectively. One can see that the variations (peak-to-peak) of the grid frequency, the output power of the diesel genset and the HKECS considerably decrease with the proposed controller as summarized in Table 5.3. This is obtained at the cost of a decline in the average power supplied by the HKECS, and consequently, with an increment in the amount of power delivered by the diesel genset. However, this amount of the power curtailment from the HKECS was considered as a reasonable power reserve and is a sensible compromise for the enhancement of the active power balancing and frequency response.

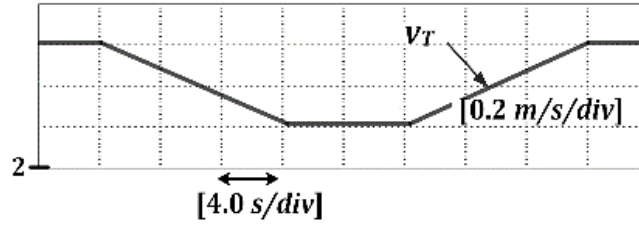


Figure 5.12 Water speed variations

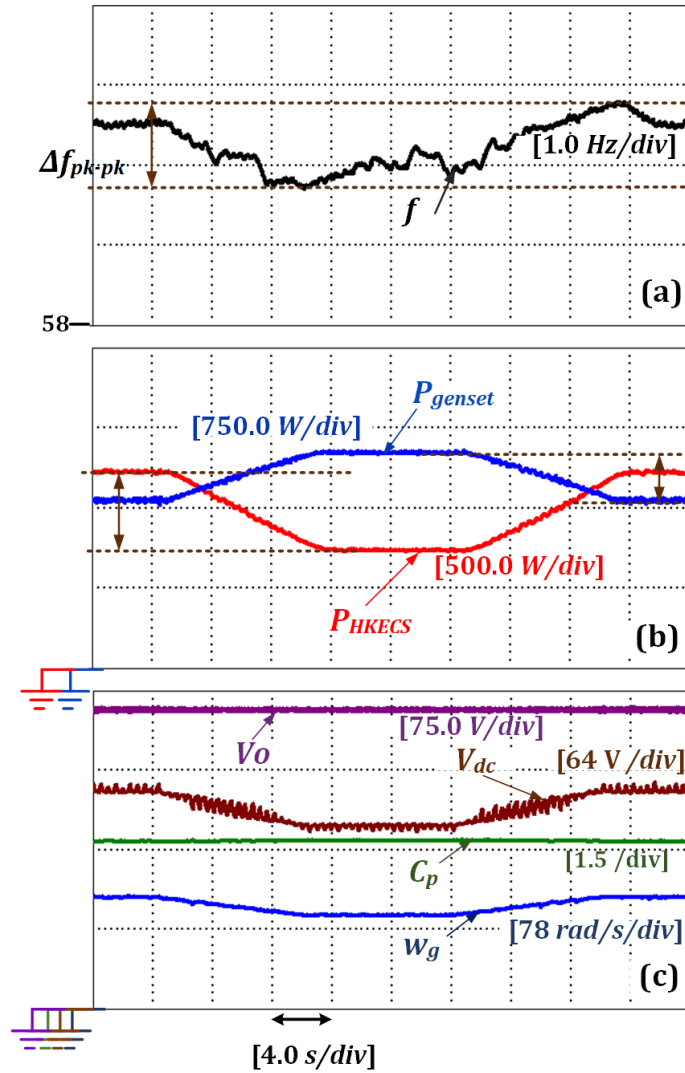


Figure 5.13 The system response to water speed variations while the HKECS operates with the MPPT mode. (a) grid frequency  $f$ , (b) HKECS output active power  $P_{HKECS}$  and diesel genset output active power  $P_{genset}$ , and (c) inverter DC-link voltage  $V_o$ , diode rectifier output voltage  $V_{dc}$ , turbine power coefficient  $C_p$ , and generator rotor speed  $\omega_g$ .

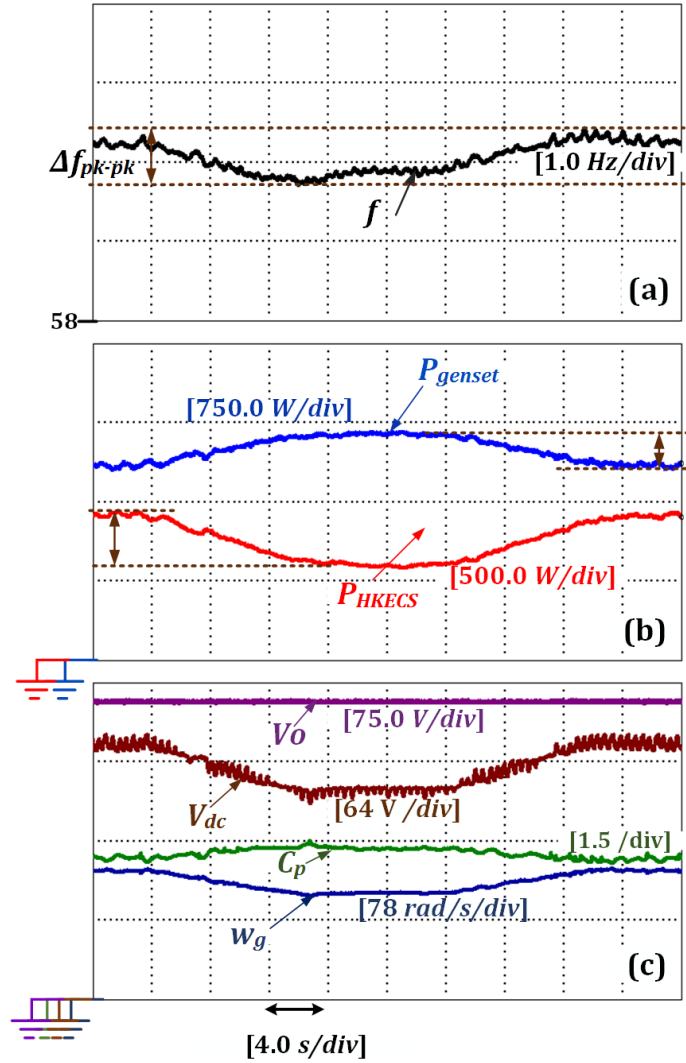


Figure 5.14 The system response to water speed variations while the HKECS operates with the proposed frequency support control loops. (a) grid frequency  $f$ , (b) HKECS output active power  $P_{HKECS}$  and diesel genset output active power  $P_{genset}$ , and (c) inverter DC-link voltage  $V_o$ , diode rectifier output voltage  $V_{dc}$ , turbine power coefficient  $C_p$ , and generator rotor speed  $\omega_g$ .

Table 5.3 Summary of the system response to water speed variations while the HKECS operates with the MPPT mode, and with the proposed frequency support control loops.

Test	$\Delta f_{PK-PK}$ (Hz) (peak-to-peak)	$\Delta P_{HKECS}$ (W) (peak-to-peak)	$\Delta P_{genset}$ (W) (peak-to-peak)
With the MPPT mode ( $K_i = 0$ and $K_d = 0$ )	1	475	487
With the proposed frequency support control loops	0.7	350	338

## 5.6 Summary

This Chapter presents a new frequency support control for a storage-less D-HK microgrid. The control scheme has been proposed for a fixed-pitch PMSG-based HKECS by synthesizing inertial and frequency droop control loops to improve the grid frequency response and to mitigate light loading operation of the diesel engine. It has been achieved by the inexpensive and simple configuration, including a diode rectifier, a DC-DC boost converter, and an inverter, and a single voltage control loop combined with the add-on frequency control scheme. With the help of the voltage control, the turbine's rotor speed, as well as its output power, is directly regulated by controlling the output voltage of the diode rectifier. There is no need for sensing the water speed and the generator speed. The procedure to select the frequency control loop gains has been proposed through the different water speeds while considering the minimum loading of the diesel engine and the HKT rotor speed limit range. Electromechanical-based emulator of the diesel genset and the HKT have been built for investigating the system performance with proposed frequency support control experimentally. The results have been demonstrated through step load change and water speed variations tests. Results showed that the use of the HKECS with the inertial and frequency control droops could significantly improve the steady-state and transient performance of the grid frequency and reduce the genset and HKECS power variations. Moreover, the light loading operation of the diesel engine was mitigated by using the proposed frequency droop control for the HKECS. To sum up, the proposed frequency support control is recommended for storage-less small-scale diesel-hydrokinetic/wind microgrids, which are not equipped with energy storage devices such as ultracapacitor, flywheel, or batteries.

## Chapter 6. Conclusions and Future Works

*This chapter concludes the research work presented in this Ph.D. Based on the explanations made through the separate chapters of the research, the overall conclusion of the research work is presented, leading to the suggestion of future work.*

### 6.1 Conclusions

The conclusions of this thesis are listed as below:

#### **In Chapter 1:**

- A discussion of the research area and some related works are provided.
- A review of the characteristics of a storage-less D-HK microgrid is presented and some advantages and disadvantages of such microgrid are highlighted.
- The research targets and objectives are defined.

#### **In Chapter 2:**

- The theoretical background and modelling of the storage-less D-HK microgrid are discussed. The steady-state and dynamic models of the HKECS and diesel genset are formulated and simulated in order to investigate some features of the storage-less D-HK.
- Some benefits and drawbacks of three common power converter topologies for the HKECS are discussed. A 6-switch converter plus 2L-VSI (back-to-back converter), and diode rectifier plus DC-DC converter plus 2L-VSL allow continuous power regulation from zero to the highest turbine speed. The diode rectifier plus DC-DC converter is simpler and less expensive than the six-switch converter. However, the problems of harmonic distortion and power losses in the generator arise.
- Power tracking control challenges in the HKECS are explained. The operation and control scheme of the HKT in both low and high-speed regions are compared. The HKECS can dispatch its output power in the low-speed region from the maximum available power to zero. However, an instability problem appears due to the inherent characteristics of the HKT. The HKT can be deloaded in the high-speed region where the power reserve is obtained from the stored kinetic energy. However, the de-loading

percentage and the control strategy to control the rotor speed so that optimal stored power can be injected into the grid, are some of the challenges.

### **In Chapter 3:**

- A dispatchable power control scheme for a fixed-pitch HKT with a PMSG followed by a diode rectifier and a boost DC-DC converter is presented. It allows an operator to set a reference power which is delivered, provided that the water speed is high enough. If not, it delivers as much as possible, operating with MPPT or in a speed limiting mode with an automatic shutdown in case of excessive water speeds.
- The controller is achieved with a novel supervisory controller with simple If – Then – Else and Min functions along with a cascaded outer power and inner diode rectifier voltage loop control system with linear controllers. Using this controller, the HKT can transit between modes of operation smoothly as the water speed and reference power from the operator change.
- The performance of the proposed supervisory controller was demonstrated experimentally with various tests conducted with an electromechanical HKT emulator with the PMSG, diode rectifier and boost DC-DC converter controlled by a DS-1103 dSPACE® system.

### **In Chapter 4:**

- A converter-based PMSG emulator as a testbed for testing and developing generator's power electronic interfaces and its control system is introduced.
- A VC-VSC is used as a converter-based power amplifier. The model of the PMSG is formulated in a real-time simulator. A virtual impedance, included in the software side, has been proposed to improve the performance of the voltage type ITM interface for emulating an electrical generator. The accuracy of the system is analysed. It is shown that it can be represented by a simple series RLC filter and its parameters can be selected irrespective of the load impedance value.
- A proportional-integral plus resonant controller is also introduced for the voltage controller of the VSC in the  $dq$  frame. It is shown that the controller provides proper voltage tracking not only for the fundamental component of variable frequency but also

for the 5<sup>th</sup> and 7<sup>th</sup> harmonic components that appear when the PMSG supplies non-linear loads.

- Experimental results were shown to validate the overall PMSG emulator performance during startup, steady state, and run down. The results have demonstrated that the proposed PMSG emulator performs well with high accuracy for both linear and nonlinear loading conditions.

### **In Chapter 5:**

- A frequency support control for storage-less D-HK microgrid is introduced. The frequency support control scheme is implemented by add-on inertial and frequency droop controllers to the conventional control scheme of the HKECS.
- The procedure to select the frequency control loop gains is explained through the different water speeds while considering the minimum loading of the diesel engine and the HKT rotor speed limit range. With the proposed control scheme, there is no need for sensing the water speed and the turbine speed.
- The system performance with the proposed frequency support control was experimentally investigated by the diesel engine and the HKT emulator. The system performance has been verified through different tests.
- Results showed that the use of the HKECS with the inertial and frequency control droops could significantly improve the steady-state and transient performance of the grid frequency, reduce diesel genset and HKECS power variations, and mitigate the light loading operation of the diesel engine.

## **6.2 Proposed Future Work**

The following topics are suggested as future work based on the acquired experiences through the separate contributions of this research work.

### **Power and Frequency Support Control for a Storage-less Diesel Hydrokinetic Microgrid**

- Diode rectifier plus DC-DC converter plus 2L-VSL has been used as a generator-side converter in this work. This topology is simple and inexpensive, but the problems of harmonic distortion and power losses in the generator arise. It would be interesting to investigate other three-phase semi-controlled rectifiers for the generator-side converter

such as Minnesota rectifier, Vienna rectifier, etc., which can help to mitigate the total harmonic distortion (THD) at ac mains [119].

- The hydrokinetic performance curve is subjected to a set of complex fluid-dynamic interactions, and the HKT may work within a set of curves instead of following only one curve [120]. In this study, only one curve was considered, and the electromechanical-based HKT emulator was developed based on one curve. It would be interesting to develop the HKT emulator with a more sophisticated model.

### **Power Electronic Converter-Based PMSG Emulator: A Testbed for Renewable Energy Experiments**

- In the choice of the machine equations, it is assumed that saturation, eddy currents and hysteresis losses are ignored although it can be considered by parameter changes. These assumptions are accurate enough to describe the performance of the PMSG during normal operating conditions. However, a more accurate machine model can be used based on a finite-element analysis (FEA) to accurately describe the machine performance during faults, saturation, etc.
- It is assumed that the current and voltage controllers of the VSC are designed based on a balanced system. Therefore, the negative and zero-sequence components in the Park transformation are ignored. Developing the controllers for an unbalanced system would be interesting.

### **Power and Frequency Support Control for a Storage-less Diesel Hydrokinetic Microgrid**

- As an extension of this study, it is necessary to identify the most important factors that limit the performance of the proposed control scheme in practice. This can be considered as future work.
- It would be interesting to provide a cost analysis of the proposed D-HK microgrid in comparison with the cost of typical diesel plants used in remote communities.

## References

- [1] C. V. Nayar, W. B. Lawrance and S. J. Phillips, "Solar/wind/diesel hybrid energy systems for remote areas," in *Proceedings of the 24th Intersociety Energy Conversion Engineering Conference*, Washington, 1989.
- [2] F. Katiraei, M. R. Iravani and P. W. Lehn, "Micro-grid Autonomous Operation during and Subsequent to Islanding Process," *IEEE Transactions on Power Delivery*, vol. 20, no. 1, pp. 248-257, 2005.
- [3] "Réseaux autonomes, portrait d'ensemble et perspectives d'avenir," Hydro-Québec Distribution, 2011.
- [4] J. Maisonneuve, P. Pillay and Claude B. Laflamme, "Osmotic power potential in remote regions of Quebec," *Renewable Energy*, vol. 81, pp. 62-70, 2015.
- [5] "Plan d'approvisionnement 2011-2020 des réseaux autonomes," Hydro-Québec Distribution, 2010.
- [6] H. J. Vermaak, K. Kusakana and S. P. Koko, "Status of Micro-Hydrokinetic River Technology in Rural Applications: A Review of Literature," *Renewable and Sustainable Energy Reviews*, vol. 29, pp. 625-633, 2014.
- [7] P. Fraenkel, "Marine current turbines: an emerging technology," in *Scottish Hydraulics Study Group Seminar*, Glasgow, 2014.
- [8] "Assessment of Canada's Hydrokinetic Power Potential, Phase I Report," Canadian Hydraulics Center, National Research Council of Canada, 2010.

- [9] "A Renewable Energy Option: Hydrokinetic Power," Hydro Quebec, Montreal, 2015.
- [10] M. Khan, G. Bhuyan, M. Iqbal and J. Quaicoe, "Hydrokinetic Energy Conversion Systems and Assessment of Horizontal and Vertical Axis Turbines for River and Tidal Applications: A Technology Status Review," *Applied Energy*, vol. 86, no. 10, pp. 1823-1835, 2009.
- [11] S. Antheaume, T. Maître and J.-L. Achard, "Hydraulic Darrieus Turbines Efficiency for Free Fluid Flow Conditions Versus Power Farms Conditions," *Renewable Energy*, vol. 33, p. 2186–2198, 2008.
- [12] R. Hunter and G. Elliot, *Wind-Diesel System: A Guide to the technology and its implementation*, New York: Cambridge University Press, 1994.
- [13] N. Mendis, K. M. Muttaqi, S. Perera and M. N. Uddin, "Remote Area Power Supply System: An Integrated Control Approach Based on Active Power Balance," *IEEE Industry Applications Magazine*, vol. 21, no. 2, pp. 63-76, 2015.
- [14] N. Mendis, K. M. Muttaqi and S. Perera, "An Effective Power Management Strategy for a Wind–Diesel–Hydrogen-Based Remote Area Power Supply System to Meet Fluctuating Demands Under Generation Uncertainty," *IEEE Transactions on Industry Applications*, vol. 51, no. 2, pp. 1128-1238, 2014.
- [15] V. J. Ginter and J. K. Pieper, "Robust Gain Scheduled Control of a Hydrokinetic Turbine," *IEEE Transactions on Control Systems Technology*, vol. 19, no. 4, pp. 805-817, 2010.
- [16] N. Luo, Y. Vidal and L. Acho, *Wind Turbine Control and Monitoring*, Springer, 2014.
- [17] L. Gordon and S. Nylund, "EZQ Stage and Velocity Sensor: Test results from The White River1," June 1999. [Online]. Available: [www.nortek-as.com/lib/technical-notes](http://www.nortek-as.com/lib/technical-notes).

- [18] S. B and Y. Kamenir, "Energetics of Turbulent Jet Flow: An Example of Jordan River Mouth," in *Fourth International Conference on Hydro-Science and Engineering (ICHE2000)*, Seoul, Korea, 2000.
- [19] S. d'Auteuil, C. Ridd and A. Birjandi, "Riverine Hydrokinetic Resource Assessment and Site Selection Using Low Cost Satellite and Aerial Winter Imagery," in *Proceedings of the 3rd Marine Energy Technology Symposium*, Washington, 2015.
- [20] M. T. Hoq, N. U. A and M. N. Islam, "Micro Hydro Power: Promising Solution for Off-grid," *International Journal of Scientific & Engineering Research*, vol. 2, no. 12, pp. 1-6, 2011.
- [21] R. Sebastian, "Simulation of the transition from Wind only mode to Wind Diesel mode in a no-storage Wind Diesel System," *IEEE Latin America Transactions*, vol. 7, no. 5, pp. 539-544, 2009.
- [22] A. G. Tomilson, "Frequency and Voltage Control of a High-Penetration, No-Storage Wind-Diesel System," Master Thesis, Memorial University of Newfoundland, Newfoundland, 1998.
- [23] L. Guzzella and A. Amstutz, "Control of Diesel Engines," *IEEE Control Systems*, vol. 18, no. 5, pp. 53-71, 1998.
- [24] C. Abbey, W. Li and G. Joos, "An Online Control Algorithm for Application of a Hybrid ESS to a Wind–Diesel System," *IEEE Transactions on Industrial Electronics*, vol. 57, no. 12, pp. 3896-3904, 2010.
- [25] F. D. Bianchi, H. d. Battista and R. J. Mantz, *Wind Turbine Control Systems: Principles, Modelling and Gain Scheduling Design*, London: Springer, 2007.
- [26] A. Sumper, O. Gomis-Bellmunt, A. Sudria-Andreu, R. Villafafila-Robles and J. Rull-

- Duran, "Response of Fixed Speed Wind Turbines to System Frequency Disturbances," *IEEE Transactions on Power Systems*, vol. 24, no. 1, pp. 181-192, 2009.
- [27] M. Hauck, I. Munteanu, A. I. Bratcu, S. Bacha and D. Roye, "Operation of Grid-Connected Cross-Flow Water Turbines in the Stall Region by Direct Power Control," *IEEE Transactions on Industrial Electronics*, vol. 58, no. 4, pp. 1132-1140, 2011.
- [28] T. Ackermann, *Wind Power in Power System*, John Wiley & Sons, 2005.
- [29] J. H. Lee, S. H. Lee and S. K. Sul, "Variable-Speed Engine Generator With Supercapacitor: Isolated Power Generation System and Fuel Efficiency," *IEEE Transactions on Industry Applications*, vol. 45, no. 6, pp. 2130-2135, 2009.
- [30] R. Peña, R. Cárdenas, J. Proboste, J. Clare and G. Asher, "Wind–Diesel Generation Using Doubly Fed Induction Machines," *IEEE Transactions on Energy Conversion*, vol. 23, no. 1, pp. 202-214, 2008.
- [31] A. L. A. Mesquita, A. L. A. Mesquita, F. C. Palheta, J. R. P. Vaz, M. V. G. d. Morais and C. Gonçalves, "A Methodology for the Transient Behavior of Horizontal Axis Hydrokinetic," *Energy Conversion and Management*, vol. 87, p. 1261–1268, 2014.
- [32] R. J. Cavagnaro, "Impact of Turbulence on the Control of a Hydrokinetic Turbine," in *International Conference on Ocean Energy*, Halifax, 2014.
- [33] J. C. Neely, K. M. Ruehl, R. A. Jepsen and J. D. Roberts, "Electromechanical emulation of hydrokinetic generators for renewable energy research," in *IEEE Conference on Oceans*, San Diego, 2013.
- [34] M. Torres and L. A. C. Lopes, "Inverter-based Virtual Diesel Generator for Laboratory-scale Applications," in *36th Annual Conference on IEEE Industrial Electronics Society*, Glendale, 2010.

- [35] M. J. Khan, M. T. Iqbal and J. E. Quaicoe, "Effects of Efficiency Nonlinearity on the Overall Power Extraction: A Case Study of Hydrokinetic-Energy-Conversion Systems," *IEEE Transactions on Energy Conversion*, vol. 26, no. 3, pp. 911-922, 2011.
- [36] M. C. Sousounis, J. K. H. Shek, R. C. Crozier and M. A. Mueller, "Comparison of Permanent Magnet Synchronous and Induction Generator for a Tidal Current Conversion System with Onshore Converters," in *2015*, Seville, IEEE International Conference on Industrial Technology (ICIT).
- [37] N. Mohan, *Advanced Electrical Drives, Analysis, Control and Modelig*, Wiley, 2014.
- [38] T. Ekelund, "Speed Control of Wind Turbines in the Stall Region," in *Proceedings of IEEE International Conference on Control and Applications*, Glasgow, 1994.
- [39] F. A. M. Vásquez, T. F. d. Oliveira and A. C. P. B. Junior, "On the Electromechanical Behavior of Hydrokinetic Turbines," *Energy Conversion and Management*, vol. 115, pp. 60-70, 2016.
- [40] J. C. Y. Hui, A. Bakhshai and P. K. Jain, "A Sensorless Adaptive Maximum Power Point Extraction Method With Voltage Feedback Control for Small Wind Turbines in Off-Grid Applications," *IEEE Journal of Emerging and Selected Topics in Power Electronics*, vol. 3, no. 3, pp. 817-828, 2015.
- [41] S. M. R. Kazmi, H. Goto, H. J. Guo and O. Ichinokura, "A Novel Algorithm for Fast and Efficient Speed-Sensorless Maximum Power Point Tracking in Wind Energy Conversion Systems," *IEEE Transactions on Industrial Electronics*, vol. 58, no. 1, pp. 29-36, 2011.
- [42] Z. Zhou, F. Sculler, J. F. Charpentier, M. E. H. Benbouzid and T. Tang, "Power Smoothing Control in a Grid-Connected Marine Current Turbine System for Compensating Swell Effect," *IEEE Transactions on Sustainable Energy*, vol. 4, no. 3,

pp. 816-826, 2013.

- [43] Z. Wu, W. Gao, J. Wang and S. Gu, "A Coordinated Primary Frequency Regulation from Permanent Magnet Synchronous Wind Turbine Generation," in *IEEE Conference on Power Electronics and Machines in Wind Applications*, Denver, 2012.
- [44] H. Wang, J. Yang, Y. Ma, Z. Xing and C. Zhe, "Model Predictive Control of PMSG-based Wind Turbines for Frequency Regulation in an Isolated Grid," in *IEEE 3rd International Future Energy Electronics Conference and ECCE Asia*, Kaohsiung, 2017.
- [45] K. V. Vidyanandan and N. Senroy, "Primary Frequency Regulation by Deloaded wind Turbines using Variable Droop," *IEEE Transactions on Power Systems*, vol. 28, no. 2, pp. 837-846, 2013.
- [46] V. Yaramasu, P. C. S. B. Wu, S. Kouro and M. Narimani, "High-power Wind Energy Conversion Systems: State-of-the-art and Emerging Technologies," *Proceedings of the IEEE*, vol. 103, no. 5, pp. 740-788, 2015.
- [47] Z. Zhang, Y. Zhao, W. Qiao and L. Qu, "A Space-Vector-Modulated Sensorless Direct-Torque Control for Direct-Drive PMSG Wind Turbines," *IEEE Transactions on Industry Applications*, vol. 50, no. 4, pp. 2331-2341, 2014.
- [48] W. Qiao, L. Qu and R. G. Harley, "Control of IPM Synchronous Generator for Maximum Wind Power Generation Considering Magnetic Saturation," *IEEE Transactions on Industry Applications*, vol. 45, no. 3, pp. 1095-1105, 2009.
- [49] A. Bidram, F. L. Lewis and A. Davoudi, "Distributed Control Systems for Small-Scale Power Networks: Using Multiagent Cooperative Control Theory," *IEEE Control Systems*, vol. 34, no. 6, pp. 56-77, 2014.

- [50] A. Yazdani and R. Iravani, *Voltage-Sourced Converters in Power Systems: Modeling, Control, and Applications*, John Wiley & Sons, 2010.
- [51] D. Dong, B. Wen, D. Boroyevich, P. Mattavelli and Y. Xue, "Analysis of Phase-Locked Loop Low-Frequency Stability in Three-Phase Grid-Connected Power Converters Considering Impedance Interactions," *IEEE Transactions on Industrial Electronics*, vol. 62, no. 1, pp. 310-321, 2015.
- [52] A. D. Hansen and G. Michalke, "Multi-pole Permanent Magnet Synchronous Generator Wind Turbines' Grid Support Capability in Uninterrupted Operation during Grid Faults," *IET Renewable Power Generation*, vol. 3, no. 3, pp. 333-348, 2009.
- [53] M. Bhardwaj, "Software Phase Locked Loop Design Using C2000™ Microcontrollers for Single Phase Grid Connected Inverter," Application Report, Texas Instruments, 2013.
- [54] N. Mohan, T. M. Undeland and W. P. Robbins, *Power Electronics: Converters, Applications, and Design*, Wiley, 2002.
- [55] A. M. Knight and G. E. Peters, "Simple Wind Energy Controller for an Expanded Operating Range," *IEEE Transactions on Energy Conversion*, vol. 20, no. 2, pp. 459-466, 2005.
- [56] D. Maksimovic, A. M. Stankovic, V. J. Thottuvelil and G. C. Verghese, "Modeling and Simulation of Power Electronic Converters," in *Proceedings of the IEEE*, 2001.
- [57] M. F. Iacchetti, G. M. Foglia, A. D. Gerlando and A. J. Forsyth, "Analytical Evaluation of Surface-Mounted PMSG Performances Connected to a Diode Rectifier," *IEEE Transactions on Energy Conversion*, vol. 30, no. 4, pp. 1367-1375, 2015.
- [58] T. Lukasiewicz, R. V. d. Oliveira and G. G. Dranka, "Control of an Islanded Wind-

- Diesel Microgrid with High Penetration Level of Wind Generation," in *IEEE Power & Energy Society General Meeting*, Denver, 2015.
- [59] J. F. Conroy and R. Watson, "Low-voltage Ride-through of a Full Converter Wind Turbine with Permanent Magnet Generator," *IET Renewable Power Generation*, vol. 1, no. 3, pp. 182-189, 2007.
- [60] M. H. Ashourianjozdani, L. A. C. Lopes and P. Pillay, "Power Sharing Control Strategy for a No-storage Hydrokinetic-Diesel System in an Isolated AC Mini-grid," in *IEEE Power and Energy Society General Meeting (PESGM)*, Boston, 2016.
- [61] X. Tan, J. Dai and B. Wu, "A Novel Converter Configuration for Wind Applications Using PWM CSI with Diode Rectifier and Buck Converter," in *IEEE International Electric Machines & Drives Conference (IEMDC)*, Niagara Falls, 2011.
- [62] O. D. Mipoung, L. A. C. Lopes and P. Pillay, "Potential of Type-1 Wind Turbines for Assisting With Frequency Support in Storage-Less Diesel Hybrid Mini-Grids," *IEEE Transactions on Industrial Electronics*, vol. 61, no. 5, pp. 2297-2306, 2014.
- [63] "IEEE Guide for Synchronous Generator Modeling Practices and Applications in Power System Stability Analyses," IEEE Std 1110-2002, IEEE Standards Association, New York, 2002.
- [64] O. D. Mipoung, L. A. C. Lopes and P. Pillay, "Frequency Support From a Fixed-Pitch Type-2 Wind Turbine in a Diesel Hybrid Mini-Grid," *IEEE Transactions on Sustainable Energy*, vol. 5, no. 1, pp. 110-118, 2014.
- [65] S. M. R. Kazmi, H. Goto, H. J. Guo and O. Ichinokura, "A Novel Algorithm for Fast and Efficient Speed-Sensorless Maximum Power Point Tracking in Wind Energy Conversion Systems," *IEEE Transactions on Industrial Electronics*, vol. 58, no. 1, pp. 29-36, 2011.

- [66] K. Yuen, K. Thomas, M. Grabbe, P. Deglaire, M. Bouquerel, D. Osterberg and M. Leijon, "Matching a Permanent Magnet Synchronous Generator to a Fixed Pitch Vertical Axis Turbine for Marine Current Energy Conversion," *IEEE Journal of Oceanic Engineering*, vol. 34, no. 1, pp. 24-31, 2009.
- [67] M. Hauck, A. Rumeau, I. Munteanu, A. I. Bratcu, S. Bacha, D. Roze and A. Hably, "A 1:1 Prototype of Power Generation System Based Upon Cross-flow Water Turbines," in *IEEE International Symposium on Industrial Electronics*, Hangzhou, 2012.
- [68] "Smart Hydro Power GmbH (Ltd.)," 2010. [Online]. Available: <http://www.smart-hydro.de/>.
- [69] M. A. Vallet, S. Bacha, I. Munteanu, A. I. Bratcu and D. Roze, "Management and Control of Operating Regimes of Cross-Flow Water Turbines," *IEEE Transactions on Industrial Electronics*, vol. 58, no. 5, pp. 1866-1876, 2011.
- [70] Z. M. Dalala, Z. U. Zahid and J. S. Lai, "New Overall Control Strategy for Small-Scale WECS in MPPT and Stall Regions With Mode Transfer Control," *IEEE Transactions on Energy Conversion*, vol. 28, no. 4, pp. 1082-1092, 2013.
- [71] C. Lumbreras, J. M. Guerrero, P. García, F. Briz and D. Díaz, "Control of a Small Wind Turbine in the High Wind Speed Region," *IEEE Transactions on Power Electronics*, vol. 31, no. 10, pp. 6980-6991, 2016.
- [72] J. Chen, T. Lin, C. Wen and Y. Song, "Design of a Unified Power Controller for Variable-Speed Fixed-Pitch Wind Energy Conversion System," *IEEE Transactions on Industrial Electronics*, vol. 63, no. 8, pp. 4899-4908, 2016.
- [73] J. Chen, J. Chen and C. Gong, "New Overall Power Control Strategy for Variable-Speed Fixed-Pitch Wind Turbines Within the Whole Wind Velocity Range," *IEEE*

*Transactions on Industrial Electronics*, vol. 60, no. 7, pp. 2652-2660, 2013.

- [74] A. Burlibasa, I. Munteanu and A. I. Bratcu, "Unitary power control strategy for low-power wind energy conversion system using active speed stall control for full-load regime," *IET Renewable Power Generation*, vol. 8, no. 6, pp. 696-706, 2014.
- [75] S. M. R. Kazmi, H. Goto, H. J. Guo and O. Ichinokura, "Review and critical analysis of the research papers published till date on maximum power point tracking in wind energy conversion system," in *IEEE Energy Conversion Congress and Exposition*, Atlanta, 2010.
- [76] J. Hussain and M. K. Mishra, "Adaptive Maximum Power Point Tracking Control Algorithm for Wind Energy Conversion Systems," *IEEE Transactions on Energy Conversion*, vol. 31, no. 2, pp. 697-705, 2016.
- [77] P. Novak, T. Ekelund, I. Jovik and B. Schmidtbauer, "Modeling and Control of Variable-speed Wind-turbine Drive-system Dynamics," *IEEE Control Systems*, vol. 15, no. 4, pp. 23-38, 1995.
- [78] R. H. B. Richard C. Dorf, *Modern Control Systems*, Prentice Hall, 2008.
- [79] S. Kouadria, S. Belfedhal, E. M. Berkouk and Y. Meslem, "Development of Real Time Wind Turbine Emulator Based on DC Motor Controlled by PI Regulator," in *Eighth International Conference and Exhibition on Ecological Vehicles and Renewable Energies (EVER)*, Monte Carlo, 2013.
- [80] T. F. Chan and L. L. Lai, "Permanent-Magnet Machines for Distributed Power Generation: A Review," in *IEEE Power Engineering Society General Meeting*, Tampa, 2007.
- [81] L. Yang, J. Wang, Y. Ma, J. Wang, X. Zhang, L. M. Tolbert, F. F. Wang and K.

- Tomsovic, "Three-Phase Power Converter-Based Real-Time Synchronous Generator Emulation," *IEEE Transactions on Power Electronics*, vol. 32, no. 2, pp. 1651-1665, 2017.
- [82] C. S. Edrington, M. Steurer, J. Langston, T. El-Mezyani and K. Schoder, " Role of Power Hardware in the Loop in Modeling and Simulation for Experimentation in Power and Energy Systems," *Proceedings of the IEEE*, vol. 103, no. 12, pp. 2401 - 2409, 2015.
- [83] W. Ren, M. Steurer and T. L. Baldwin, "Improve the Stability and the Accuracy of Power Hardware-in-the-Loop Simulation by Selecting Appropriate Interface Algorithms," *IEEE Transactions on Industry Applications*, vol. 44, no. 4, pp. 1286-1294, 2008.
- [84] P. C. Krause, O. Wasynczuk and S. D. Sudhoff, *Analysis of Electric Machinery and Drive Systems*, IEEE Press, 2002.
- [85] R. S. Kaarthik and P. Pillay, "Emulation of a Permanent Magnet Synchronous Generator in Real-time using Power Hardware-in-the-loop," in *IEEE International Conference on Power Electronics, Drives and Energy Systems (PEDES)*, Trivandrum, 2016.
- [86] S. R. Macminn and R. J. Thomas, "Microprocessor simulation of synchronous Machine Dynamics in Real-Time," *IEEE Transactions on Power Systems*, vol. 1, no. 3, pp. 220-225, 1986.
- [87] M. Steurer, C. S. Edrington, M. Sloderbeck, W. Ren and J. Langston, "A Megawatt-Scale Power Hardware-in-the-Loop Simulation Setup for Motor Drives," *IEEE Transactions on Industrial Electronics*, vol. 57, no. 4, pp. 1254-1260, 2010.
- [88] F. Lehfuss, G. Lauss, P. Kotsampopoulos, N. Hatziaargyriou, P. Crolla and A. Roscoe, "Comparison of Multiple Power Amplification Types for Power Hardware-in-the-Loop

- Applications," in *Complexity in Engineering (COMPENG). Proceedings*, Aachen, 2012.
- [89] G. Si and R. M. K. J. Cordier, "Extending the Power Capability With Dynamic Performance of a Power-Hardware-in-the-Loop Application—Power Grid Emulator Using “Inverter Cumulation,” *IEEE Transactions on Industry Applications*, vol. 52, no. 4, pp. 3193-3202, 2016.
- [90] M. H. Ashourianjozdani, L. A. C. Lopes and P. Pillay, "Power Control Strategy for Fixed-pitch PMSG-based Hydrokinetic Turbine," in *IEEE International Conference on Power Electronics, Drives and Energy Systems (PEDES)*, Trivandrum, 2016.
- [91] J. Wang, Y. Ma, L. Yang, L. M. Tolbert and F. Wang, "Power converter-based three-phase induction motor load emulator," in *Twenty-Eighth Annual IEEE Applied Power Electronics Conference and Exposition (APEC)*, Long Beach, 2013.
- [92] A. D. Paquette, M. J. Reno, R. G. Harley and D. M. Divan, "Sharing Transient Loads: Causes of Unequal Transient Load Sharing in Islanded Microgrid Operation," *IEEE Industry Applications Magazine*, vol. 20, no. 2, pp. 23-34, 2014.
- [93] N. Pogaku, M. Prodanovic and T. C. Green, "Modeling, Analysis and Testing of Autonomous Operation of an Inverter-Based Microgrid," *IEEE Transactions on Power Electronics*, vol. 22, no. 2, pp. 613-625, 2007.
- [94] P. C. Loh, M. J. Newman, D. N. Zmood and D. G. Holmes, "A Comparative Analysis of Multiloop Voltage Regulation Strategies for Single and Three-phase UPS Systems," *IEEE Transactions on Power Electronics*, vol. 18, no. 5, pp. 1176-1185, 2003.
- [95] R. T. a. F. B. M. Liserre, "Multiple Harmonics Control for Three-phase Grid Converter Systems with the Use of PI-RES Current Controller in a Rotating Frame," *IEEE Transactions on Power Electronics*, vol. 21, no. 3, pp. 836-84, 2006.

- [96] M. Ashourianjozdani, L. A. C. Lopes and P. Pillay, "Converter-based PMSG Emulator: A Testbed for Renewable Energy Experiments," in *IEEE International Electric Machines and Drives Conference (IEMDC)*, Miami, 2017.
- [97] W. Ren, M. Steurer and T. L. Baldwin, "An Effective Method for Evaluating the Accuracy of Power Hardware-in-the-Loop Simulations," *IEEE Transactions on Industry Applications*, vol. 45, no. 4, pp. 1484-1490, 2009.
- [98] M. Arriaga, C. A. Cañizares and M. Kazerani, "Renewable Energy Alternatives for Remote Communities in Northern Ontario, Canada," *IEEE Transactions on Sustainable Energy*, vol. 4, no. 3, pp. 661-670, 2013.
- [99] M. A. Vallet, S. Bacha, I. Munteanu, A. I. Bratcu and D. Roye, "Management and Control of Operating Regimes of Cross-Flow Water Turbines," *IEEE Transactions on Industrial Electronics*, vol. 58, no. 5, pp. 1866-1876, 2011.
- [100] R. Engleitner, A. Nied, M. S. M. Cavalca and J. P. d. Costa, "Dynamic Analysis of Small Wind Turbines Frequency Support Capability in a Low-Power Wind-Diesel Microgrid," *IEEE Transactions on Industry Applications*, vol. 54, no. 1, pp. 102-111, 2018.
- [101] J. Carrasco, L. Franquelo, J. Bialasiewicz, E. Galvan, R. PortilloGuisado, M. Prats, J. Leon and N. Moreno-Alfonso, "Power-Electronic Systems for the Grid Integration of Renewable Energy Sources: A Survey," *IEEE Transactions on Industrial Electronics*, vol. 53, no. 4, pp. 1002-1016, 2006.
- [102] L. Ruttledge, N. W. Miller, J. O'Sullivan and D. Flynn, "Frequency Response of Power Systems With Variable Speed Wind Turbines," *IEEE Transactions on Sustainable Energy*, vol. 3, no. 4, pp. 683-691, 2012.

- [103] J. Hossain and A. Mahmud, *Large Scale Renewable Power Generation*, 2014, Springer.
- [104] D. G. Infield, G. W. Slack, N. H. Lipman and P. J. Musgrove, "Review of Wind/Diesel Strategies," *IEE Proceedings A - Physical Science, Measurement and Instrumentation, Management and Education - Reviews*, vol. 130, no. 9, pp. 613-619, 1983.
- [105] P. Rosas, W. Lemos, A. Pereira, R. Barros and E. Feitosa, "Problems of Planning Hybrid Wind-Diesel Power Systems," in *IEEE/PES Transmission and Distribution Conference and Exposition: Latin America*, 2004.
- [106] H. Rezvani and A. Hekmati, "Wind Diesel Hybrid System without Battery Energy Storage Using Imperialist Competitive Algorithm," *International Journal of Electrical and Computer Engineering*, vol. 9, no. 6, pp. 560-564, 2015.
- [107] A. Merabet, K. T. Ahmed, H. Ibrahim, R. Beguenane and A. M. Y. M. Ghias, "Energy Management and Control System for Laboratory Scale Microgrid Based Wind-PV-Battery," *IEEE Transactions on Sustainable Energy*, vol. 8, no. 1, pp. 145-154, 2017.
- [108] Y. Wang, X. Z. J. Meng and L. Xu, "Control of PMSG-Based Wind Turbines for System Inertial Response and Power Oscillation Damping," *IEEE Transactions on Sustainable Energy*, vol. 6, no. 2, pp. 565-574, 2015.
- [109] Z. Wu, D. W. Gao, H. Zhang, S. Yan and X. Wang, "Coordinated Control Strategy of Battery Energy Storage System and PMSG-WTG to Enhance System Frequency Regulation Capability," *IEEE Transactions on Sustainable Energy*, vol. 8, no. 3, pp. 1330-1343, 2017.
- [110] V. Kleftakis, A. Rigas, C. Papadimitriou, N. Katsoulakos, P. Moutis and N. Hatziargyriou, "Contribution to Frequency Control by a PMSG Wind Turbine in a Diesel-Wind Turbine Microgrid for Rural Electrification," in *IEEE MedPower*

*Conference, Athens, 2014.*

- [111] I. D. Margaritis, S. A. Papathanassiou, N. D. Hatziargyriou, A. D. Hansen and P. Sorensen, "Frequency Control in Autonomous Power Systems With High Wind Power Penetration," *IEEE Transactions on Sustainable Energy*, vol. 3, no. 2, pp. 189-199, 2012.
- [112] Z. Wu, W. Gao, J. Wang and S. Gu, "A Coordinated Primary Frequency Regulation from Permanent Magnet Synchronous Wind Turbine Generation," in *IEEE Power Electronics and Machines in Wind Applications*, Denver, 2012.
- [113] Y. Tan, K. M. Muttaqi, P. Ciufo and L. Meegahapola, "Enhanced Frequency Response Strategy for a PMSG-Based Wind Energy Conversion System Using Ultracapacitor in Remote Area Power Supply Systems," *IEEE Transactions on Industry Applications*, vol. 53, no. 1, pp. 549-558, 2017.
- [114] P. Kundur, *Power System Stability and Control*, McGraw-Hill, 1994.
- [115] X. Yingcheng and T. Nengling, "Review of Contribution to Frequency Control Through Variable Speed Wind Turbine," *Renewable energy*, vol. 36, pp. 1671-1677, 2011.
- [116] S. Krishnamurthy, T. M. Jahns and R. H. Lasseter, "The Operation of Diesel Gensets in a CERTS Microgrid," in *IEEE Power and Energy Society General Meeting - Conversion and Delivery of Electrical Energy in the 21st Century*, Pittsburgh, 2008.
- [117] A. S. Ahmadyar and G. Verbič, "Control Strategy for Optimal Participation of Wind Farms in Primary Frequency Control," in *IEEE Eindhoven PowerTech*, Eindhoven, 2015.
- [118] A. Zertek, G. Verbic and M. Pantos, "A Novel Strategy for Variable-Speed Wind Turbines' Participation in Primary Frequency Control," *IEEE Transactions on*

*Sustainable Energy*, vol. 3, no. 4, pp. 791-799, 2012.

- [119] B. Singh, B. N. Singh, A. Chandra, K. Al-Haddad, A. Pandey and D. P. Kothari, "A Review of Three-Phase Improved Power Quality," *IEEE Transactions on Industrial Electronics*, vol. 51, no. 3, pp. 641-660, 2004.
  
- [120] L. Lazauskas and B. Kirke, "Modeling passive variable pitch cross flow hydrokinetic turbines to maximize," *Renewable Energy*, vol. 45, pp. 41-50, 2012.
  
- [121] L. A. Lopes, J. Lhuilier, M. F. Khokar and A. Mukherjee, "A Wind Turbine Emulator that Represents the Dynamics of the Wind Turbine Rotor and Drive Train," in *IEEE 36th Power Electronics Specialists Conference*, Recife, 2005.
  
- [122] F. Blaabjerg and Z. Chen, *Power Electronics for Modern Wind Turbines*, Morgan & Claypool Publishers, 2006.
  
- [123] H. Garnier, M. Mensler and A. Richard, "Continuous-time Model Identification From Sampled Data: Implementation Issues and Performance Evaluation," *International Journal of Control*, vol. 76, no. 13, p. 1337–1357, 2003.

## Appendix A

### The parameters of the study

The main parameters of Chapter 2, Chapter 3, and Chapter 5 are given below.

TABLE A.1  
HKT PARAMETERS

Parameter	Value	Parameter	Value
$P_{HKT,N}$	1.45 (kW)	Turbine inertia	2.5 (kg.m <sup>2</sup> )
$R$	0.33 (m)	$v_{T,cut\_in}$	1.2 (m/s)
$H$	0.5 (m)	$v_{T, gN}$	2.7 (m/s)
$\rho$	1000(kg.m <sup>-3</sup> )	$v_{T, cN}$	2.8 (m/s)
$g_r$	6	$v_{T, cut\_off}$	3.0 (m/s)
$C_p = 0.0119\lambda^6 + 0.127\lambda^5 + 0.496\lambda^4 + 0.795\lambda^3 + 0.39\lambda^2 + 0.0762\lambda + 0.000237.$			

TABLE A. 2  
PMSG AND POWER ELECTRONICS INTERFACE PARAMETERS

Parameter	Value	Parameter	Value
$P_{PMSG,N}$	5 (kW)	J	0.01 (kg.m <sup>2</sup> )
$\lambda_m$	0.6 (V.s)	$V_o$	250 (V)
$R_g$	0.37 ( $\Omega$ )	$K_V$	1.8
$L_g$	0.0014 (H)	$K_T$	2.08
$n_p$	2	$\mu$	0.86

TABLE A. 3  
CONTROL SYSTEM PARAMETERS

Parameter	Value	Parameter	Value
Sampling time	80 ( $\mu$ s)	$\tau$	0.8 (s)
$K_p$	0.024	$T_z$	0.27 (s)
$K_i$	0.29	$T_p$	0.4 (s)
$K_d$	0.0005	M	5.2
$K_{ip}$	0.1		

TABLE A. 4  
PARAMETERS OF DC MOTOR (HKT EMULATOR)

Parameter	Value	Parameter	Value
$P$	11 ( $kW$ )	$n$	1750 ( $RPM$ )
$V$	240 ( $V$ )	$J$	0.06 ( $kg \cdot m^2$ )
$I$	53.5 ( $A$ )	$K_{T\_DC}$	1.18 ( $N \cdot m/A$ )

TABLE A.5  
PARAMETERS OF DIESEL ENGINE

Parameter	Value	Parameter	Value
$\tau_s$	0.022( $s$ )	$m$	$5.5e-5(rad/sW)$
$m_f$	1.5( $lb/s$ )	$\omega_{nen}$	188.5( $rad/s$ )
$J$	0.163 ( $kg \cdot m^2$ )		

TABLE A. 6  
PARAMETERS OF DC MOTOR AND DC DRIVE (GENSET EMULATOR)

Parameter	Value	Parameter	Value
$P_{DC\ motor}$	5 ( $HP$ )	$n$	1800 ( $RPM$ )
$I$	22.7 ( $A$ )	$I$ (ABB DCS800 )	25 ( $A$ )
$V$	220 ( $V$ )		

TABLE A.7  
PARAMETERS OF WOUND ROTOR SYNCHRONOUS GENERATOR

Parameter	Value	Parameter	Value
$P_{ge}$	11 (kW)	$V$	220 (V)
$S_{ge}$	14 (kVA)	$n$	1800 (RPM)
$I$	36 (A)	$p$	2

The main parameters of Chapter 4 are given below.

TABLE A.8  
PMSG AND POWER ELECTRONICS INTERFACE PARAMETERS

Parameter	Value	Parameter	Value
$\lambda_{af}$	0.63(V.s)	$V_{dc}$	350(V)
$R_s$	0.1718( $\Omega$ )	$f_{sw}$	12(kHz)
$L_d, L_q$	5.14, 14.19(mH)	$C_F$	7( $\mu$ F)
Poles	4	$R_C$	0.5( $\Omega$ )
Inertia	0.033(kg.m <sup>2</sup> )	$L_F$	1(mH)
		$R_F$	0.5( $\Omega$ )

TABLE A.9  
CONTROL AND MEASUREMENT SYSTEM PARAMETERS

Parameter	Value	Parameter	Value
$K_{PC}$	7	$\alpha$	10000
$K_{IC}$	20852	Sample Time	80( $\mu$ s)
$K_{PV}$	0.0036	Time delay ( $\mu$ s)	15
$K_{IV}$	1.5	$\omega_{cu}$	1
$K'_{IV}$	45		

TABLE A.10  
SYSTEM PER UNIT BASE VALUES

Parameter	Value	Parameter	Value
$V_{base}$	180 (V) (Phase)	$f_{h-base}$	60(Hz)
$I_{base}$	12.6 (A) (Phase)	$S_{base}$	3402(VA)

## Appendix B

### • Two-Mass Drivetrain System (Chapter 2)

Figure B.1 shows the physical model considered for the representation of the two-mass drivetrain system. In this model,  $J_{HKT}$  and  $B_{HKT}$  are the mass moment of inertia and friction damping coefficient of the turbine, respectively.  $K$  is torsional spring constant, indicating the stiffness of the mechanical shaft at the low-speed side (turbine side).  $J_{PMSG}$  is the mass moment of inertia and  $B_{PMSG}$  is friction damping of the generator at the high-speed side (PMSG side). The mathematical equations of the two-mass model are given by [121], [28].

$$\frac{d\omega_m}{dt} = \frac{T_{HKT}}{J_{HKT}} - \frac{B_{HKT}}{J_{HKT}} \omega_m - \frac{K}{J_{HKT}} (\theta_m - \theta_{LS}) \quad (B.1)$$

$$\frac{d\omega_g}{dt} = \frac{T_{HS}}{J_{PMSG}} - \frac{T_{ePMSG}}{J_{PMSG}} - \frac{B_{PMSG}}{J_{PMSG}} \omega_g \quad (B.2)$$

$$g_r = \frac{T_{HS}}{T_{LS}} = \frac{\omega_{HS}}{\omega_{LS}} = \frac{n_{LS}}{n_{HS}} \quad (g_r > 1) \quad (B.3)$$

Where  $\omega_{LS}$  and  $\omega_{HS}$  are the angular speed at the low-side and high-side of an ideal gearbox with gear ratio  $g_r: 1$ , where  $g_r = n_{LS}/n_{HS}$ .  $\theta_m$  and  $\theta_{LS}$  are the angle of the turbine shaft and the angle of low-side of the gearbox, respectively.

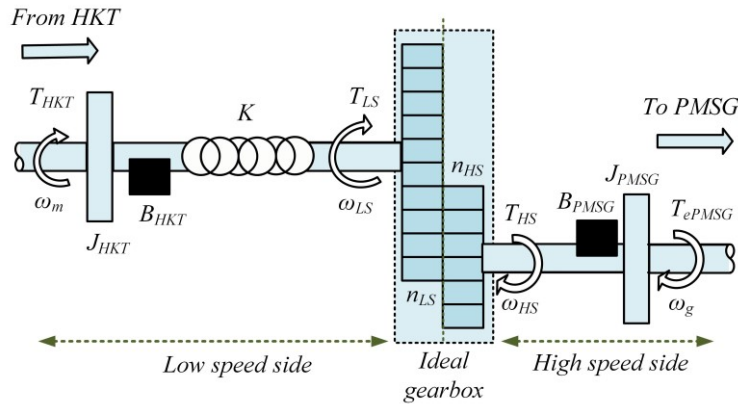


Figure B.1 Two-mass drive train system

- **Torque (or Current) Control of a DC motor Controlled with HCC by a DC-DC Buck Converter-HKT emulator (Chapter 3)**

The torque developed by a separately excited DC motor can be given as

$$T_e = K_T I_a \tag{B.4}$$

where  $I_a$  is the armature current and  $K_T$  is the torque constant factor.

The current of DC motor is controller based on HCC control with DC-DC buck converter as shown in Figure B.2. The HCC is implemented by using a J-K flip-flop as shown in Figure B.3. When the actual current of the DC motor ( $I_a$ ) keeps in the tolerance band, the state of the switch remains the same. The tolerance band is selected around the reference current ( $I_{a, ref}$ ) of the machine. The switch will be turned off, if  $I_a$  will be higher than the upper limit of the tolerance band. If  $I_a$  is less than the lower limit of the tolerance band, the switch will be turned on. From equation (B.4), the reference current can be related to reference torque, which is defined by produced torque by the HKT. Figure B.4 shows the performance of the HCC implemented by a J-K flip-flop.  $I_{a, ref}$  is 10A, Frequency of clock signal is 3.33 (kHz) and tolerance band ( $\epsilon$ ) is 0.2 A.

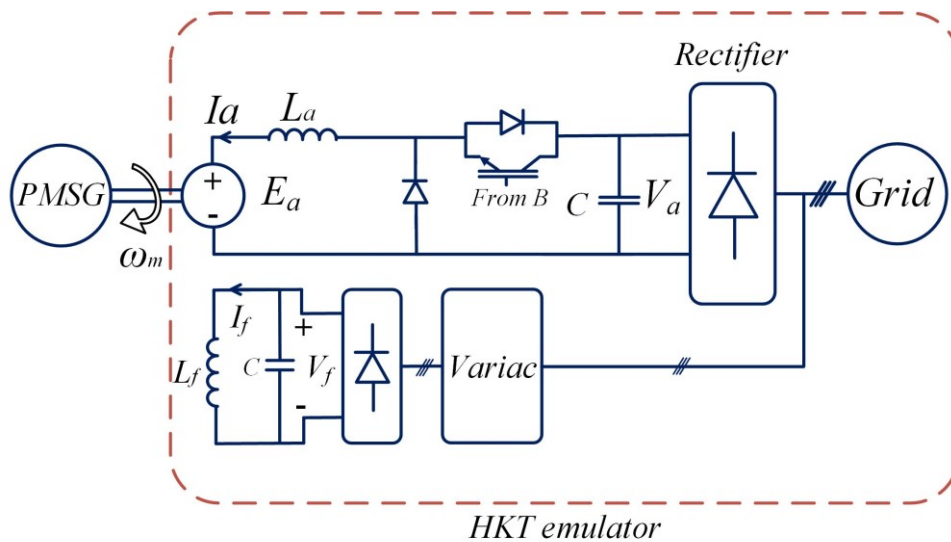


Figure B.2 Block diagram of HKT emulator

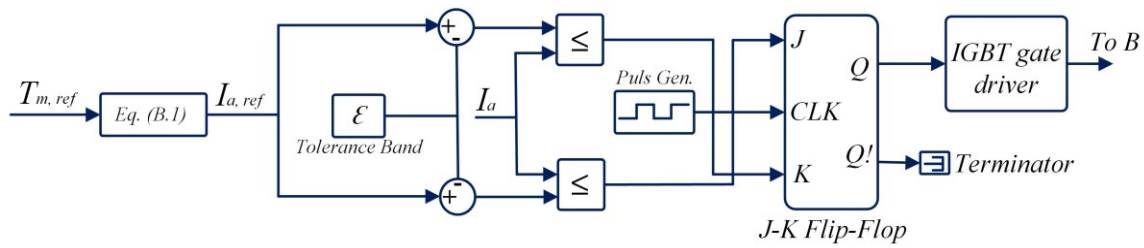


Figure B.3 Torque Control of a DC motor Controlled with HCC from a DC-DC Buck converter

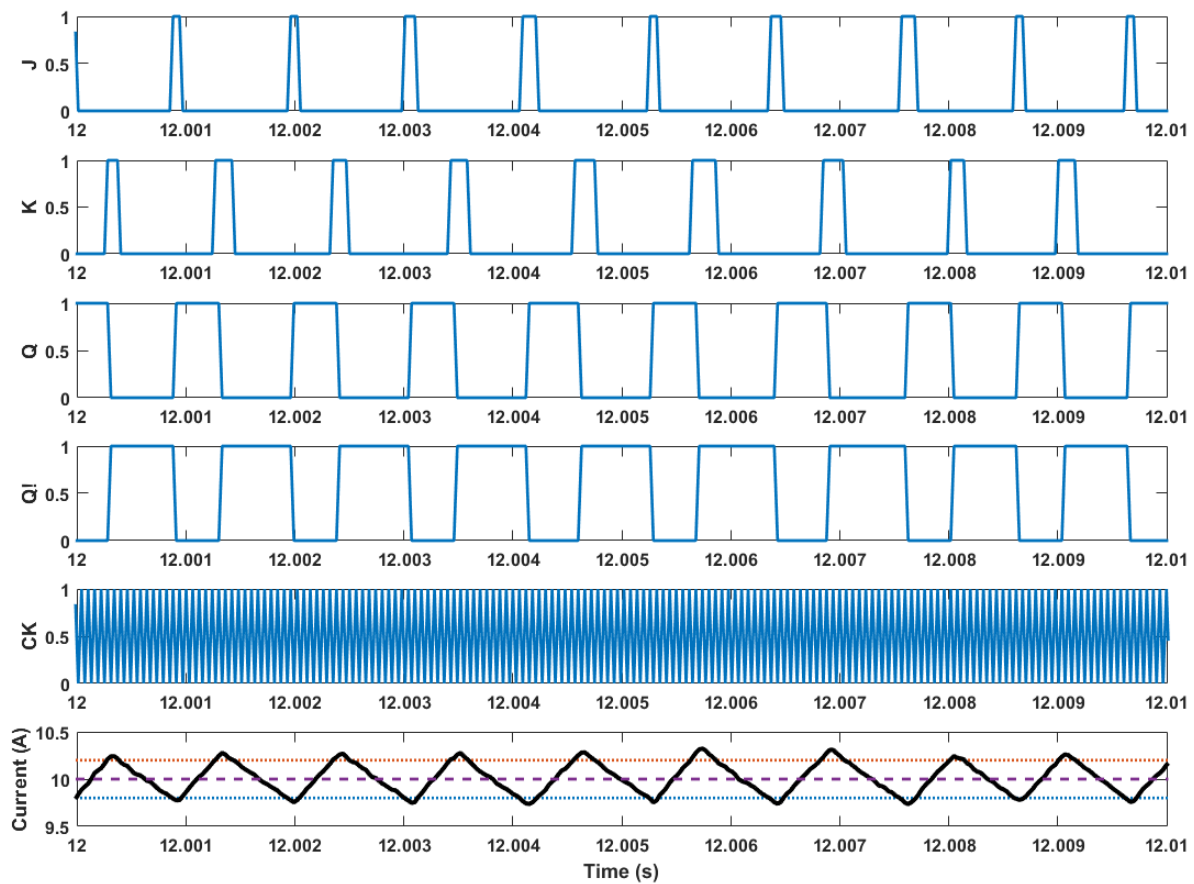


Figure B.4 the performance of the HCC implemented by a J-K flip-flop.  $I_{a, ref} = 10\text{A}$ , frequency of clock signal = 3.33 (kHz) and tolerance Band ( $\epsilon$ ) = 0.2 A

- **Impact of Water Speed Variations on the System's Behavior (Chapter 3)**

In this Section, simulation tests are performed to demonstrate the impact of water speed variations on of the proposed control system's behaviour. Figure B. 5. (a) shows the water speed profile. Figure B. 5. (b), (c), (d), and (e) show the resulting output power, output voltage of the rectifier, the generator rotor speed, and the power coefficient of the HKT, respectively, for various operating conditions.

From  $t = 110$  s to 130 s,  $P_{dc, sp}$  is set to 0.6 kW-while the water speed is changed as shown in Figure B. 5. (a). Since  $P_{dc, sp}$  is less than the maximum available  $P_{dc}$ , the integrator is enabled and the *Min* function outputs  $V_{dc, 1}$ . In Figure B. 5. (c), one can see that  $V_{dc}$  follows  $V_{dc, 1}$ . The system operates in the PRM and  $P_{dc}$  is regulated at 0.6 kW as shown in Figure B. 5. (b). In this segment, the power coefficient is less than 0.3, indicating that the HKT operates in the stall region.

From  $t = 130$  s to 150 s,  $P_{dc, sp}$  is changed to 1.26 kW. In this segment,  $P_{dc, sp}$  is more than maximum available power according to actual water speeds. Therefore, the integrator is grounded and the *Min* function outputs  $V_{dc, 12}$ . In this segment, the system operates in MPPT/SLM. The power coefficient is found to be around 0.3, the value of maximum power coefficient  $C_{p, max}$ .

At  $t = 150$  s,  $P_{dc, sp}$  is changed to 0.6 kW, remaining in this condition until  $t = 170$  s. Since  $P_{dc, sp} < P_{dc, MPPT}$ , the integrator is enabled and the *Min* function outputs  $V_{dc, 1}$ . The power control algorithm regulates  $P_{dc}$  to  $P_{dc, sp}$ . As shown in Figure B. 5. (b), after a brief transient,  $P_{dc}$  is regulated at 0.6 kW. Finally, it is shown that the proposed supervisory power control system works properly with water speed profile containing ripple.

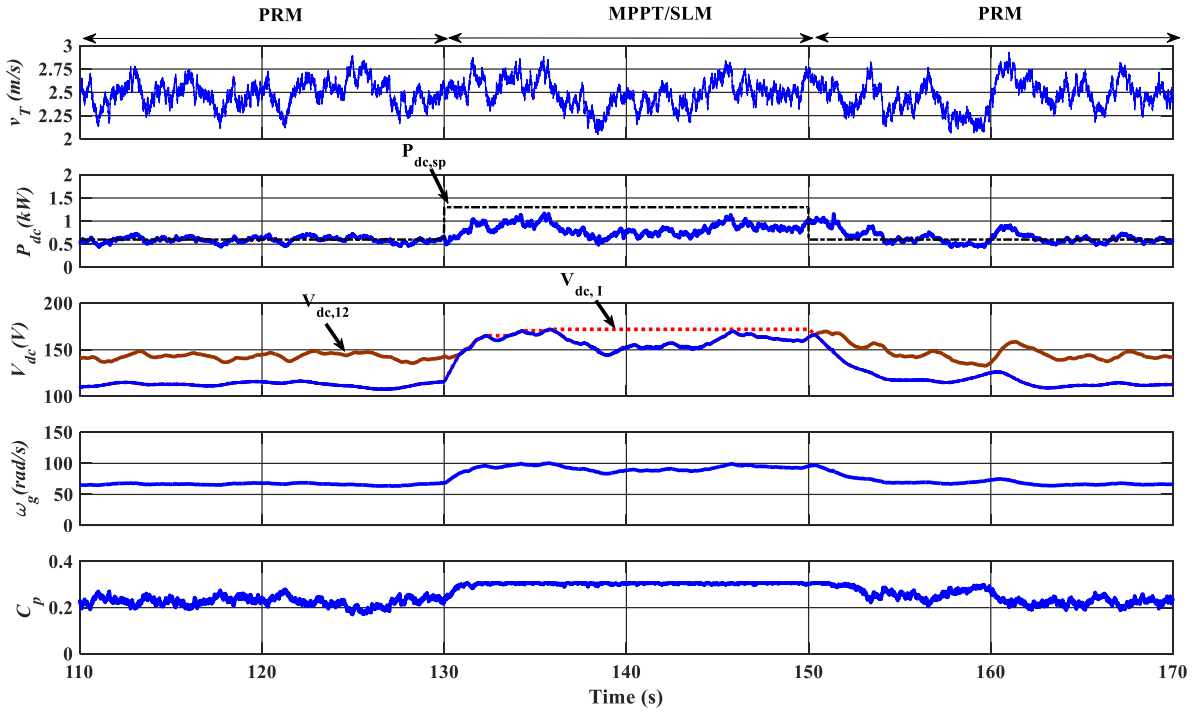


Figure B.5 HKECS system parameters: (a) water speed variations, (b) output DC power, (c) output DC voltage, (d) PMSG rotor speed, and (e) turbine power coefficient.

## Appendix C

### Park Transformation

The  $dq$  variables are obtained from  $abc$  variables through the Park transformation as:

$$v_{dq0}(t) = \begin{bmatrix} v_q(t) \\ v_d(t) \\ v_0(t) \end{bmatrix} = T \begin{bmatrix} v_a(t) \\ v_b(t) \\ v_c(t) \end{bmatrix} = T v_{abc}(t) \quad \text{C.1}$$

where,

$$T = \frac{2}{3} \begin{bmatrix} \cos(\theta) & \cos(\theta - \frac{2\pi}{3}) & \cos(\theta + \frac{2\pi}{3}) \\ \sin(\theta) & \sin(\theta - \frac{2\pi}{3}) & \sin(\theta + \frac{2\pi}{3}) \\ 1 & 1 & 1 \end{bmatrix} \quad \text{C.2}$$

where  $\theta$  is the electrical rotor angular position.